# Operational Two-Stage Stratified Topographic Correction of Spaceborne Multispectral Imagery Employing an Automatic Spectral-Rule-Based Decision-Tree Preliminary Classifier

Andrea Baraldi, Matteo Gironda, and Dario Simonetti

***Abstract*—The increasing amount of remote sensing (RS) imagery acquired from multiple platforms and the recent announcements that scientists and decision makers around the world will soon have unrestricted access at no charge to large-scale spaceborne multispectral (MS) image databases make urgent the need to develop easy-to-use, effective, efficient, robust, and scalable satellite-based measurement systems. In these scientific and industrial contexts, it is well known that, to date, the operational performance of existing stratified non-Lambertian (anisotropic) topographic correction (SNLTOC) algorithms has been limited by the need for *a priori* knowledge of structural landscape characteristics, such as surface roughness which is land cover class specific. In practice, to overcome the circular nature of the SNLTOC problem, a mutually exclusive and totally exhaustive land cover classification map of a spaceborne MS image is required *before* SNLTOC takes place. This system requirement is fulfilled by the original operational automatic two-stage SNLTOC approach presented in this paper which comprises, in cascade, 1) an automatic stratification first stage and 2) a second-stage ordinary SNLTOC method selected from the literature. The former combines 1) four subsymbolic digital-elevation-model-derived strata, namely, horizontal areas, self-shadows, and sunlit slopes either facing the sun or facing away from the sun, and 2) symbolic (semantic) strata generated from the input MS image by an operational fully automated spectral-rule-based decision-tree preliminary classifier recently presented in RS literature. In this paper, first, previous works related to the TOC subject are surveyed, and next, the novel operational two-stage SNLTOC system is presented. Finally, the original two-stage SNLTOC system is validated in up to 19 experiments where the system's capability of reducing within-stratum spectral variance while preserving pixel-based spectral patterns (shapes) is assessed quantitatively.**

***Index Terms*—Decision-tree classification, digital elevation model (DEM), fuzzy rule, image-understanding system, inductive data learning, prior knowledge, topographic correction.**

Manuscript received May 27, 2008; revised July 24, 2008, November 14, 2008, March 16, 2009, and June 3, 2009. First published October 6, 2009; current version published December 23, 2009.

A. Baraldi was with the European Commission Joint Research Centre, 21020 Ispra, Italy. He is now with Baraldi Consultancy in Remote Sensing, 40129 Bologna, Italy (e-mail: andrea6311@gmail.com).

M. Gironda was with the University Institute of Architecture of Venice, 30135 Venezia, Italy (e-mail: teogironda@libero.it).

D. Simonetti is with the European Commission Joint Research Centre, 21020 Ispra, Italy (e-mail: dario.simonetti@ext.jrc.ec.europa.eu).

Color versions of one or more of the figures in this paper are available online at http://ieeexplore.ieee.org.

Digital Object Identifier 10.1109/TGRS.2009.2028017

## I. Introduction

THE POTENTIAL of remote sensing (RS) for the monitoring of the Earth's environment and the detection of its temporal variations at geographic extents ranging from local (areas up to 100 000 $km^2$) to regional (roughly between 100 000 and 1 000 000 $km^2$ [1]), continental, and global scales is well known by user communities involved with urban growth assessment and planning, intelligence/surveillance applications for national security and defense purposes, ecosystem management, watershed protection, water balance calculations, risk management, and global change [1]–[3].

The increasing number of Earth observation (EO) spaceborne platforms featuring enhanced combinations of radiometric, spatial, spectral, and temporal resolution and the recent announcements that scientists and decision makers around the world will soon have unrestricted access at no charge to large-scale RS image databases [4] make urgent the need to develop operational satellite-based measurement systems suitable for automating the quantitative analysis of RS imagery, which is one of the traditional goals of the RS community involved with global land cover and land cover change assessment [1].

Unfortunately, to date, the transformation of huge amounts of multisource spaceborne imagery into information still remains far below reasonable expectations and mostly confined to scientific applications [5]. In common practice, an insufficient RS image mapping capability may be due to two main factors.

1) Existing scientific and commercial RS image-understanding systems (RS-IUSs), such as [6] and [7] which have recently gained a noteworthy popularity, score low in operational performance which encompasses [8], [9] the following:
   a) ease of use (degree of automation);
   b) effectiveness (e.g., classification accuracy);
   c) efficiency (e.g., computation time and memory occupation);
   d) economy (costs increase monotonically with manpower, e.g., the manpower required to collect scene-specific training samples);
   e) robustness to changes in input parameters;
   f) robustness to changes in the input data set;
   g) maintainability/scalability/reusability to keep up with users' changing needs;

h) timeliness (defined as the time span between data acquisition and product delivery to the end user; it increases monotonically with manpower).

For example, a low operational performance measurement may explain why the impact upon commercial RS image-processing software toolboxes of the literally hundreds of so-called novel low (subsymbolic)- and high (symbolic)-level image-processing algorithms presented each year in scientific literature remains negligible [5].

2) The increasing rate of collection of RS data of enhanced quality outpaces the capabilities of both manual inspection and inductive machine learning from supervised (labeled) EO data [2]. The cost, timeliness, quality, and availability of adequate reference (training/testing) data sets derived from field sites, existing maps, and tabular data as a source of prior knowledge are considered the most limiting factors on RS data product generation and validation [1].

From a technical viewpoint, a data processing system is termed *fully automated* when it requires neither user-defined parameters nor reference data samples to run; therefore, its ease of use is unsurpassed [10]. *To automate a data processing system, necessary, although not sufficient, conditions are for input data to be* [11] 1) *well behaved* (well conditioned), i.e., not violating any assumptions needed to successfully apply whatever analysis the system performs, e.g., every input data source is expressed in a physical unit of measure and belongs to a known domain of variation, and 2) *well understood* by the system developer, namely, every input data source is provided with a clear physical meaning and with a community-agreed data format.

In particular, EO sensor-derived data are well behaved when they are as follows.

1) Radiometrically calibrated, i.e., dimensionless digital numbers (DNs) are transformed into a community-agreed radiometric unit of measure. For example, in the context of the Global Monitoring for the Environment and Security (GMES) program, led by the European Union (EU) in partnership with the European Space Agency (ESA), and of the Global Earth Observation System of Systems (GEOSS), conceived by the Group on Earth Observations (GEO) [12]–[14], calibration and validation (Cal/Val)-related activities are considered crucial in accomplishing harmonization and interoperability of EO data and derived products generated from multiple sources. In particular, the Quality Assurance Framework for Earth Observation data (QA4EO) [15] initiative led by the Committee of Earth Observations (CEOS) [16] Working Group on Calibration and Validation [17] aims at establishing an appropriate coordinated program of Cal/Val initiatives throughout all stages of a spaceborne mission, from sensor build to end of life.
2) Geometrically corrected, i.e., projected onto a community-agreed terrestrial reference system.
3) Validated, i.e., provided with quantitative, unequivocal, and traceable measures of geometric and radiometric EO data quality. For example, in the words of the QA4EO initiative, in an EO data product generation and delivery chain, every operation or data flow must be provided with a quality indicator (QI) based on an unequivocal quantifiable metrological/statistically based measure [15, p. 7], i.e., a QI is based on a documented quantitative assessment of its traceability to a community-agreed reference standard ideally tied to a physical unit of measure belonging to an international system of units. Accurate operation performance/data quality tracking (traceability) provides knowledge on what is not performing up to a reference standard, so that alternative quality assurance strategies can be enforced at that stage.

In multisensor data fusion, image mosaicking for visualization and classification purposes, multitemporal image analysis, and quantitative biophysical [e.g., leaf area index (LAI)] and biochemical [e.g., fraction of absorbed photosynthetically active radiation (FAPAR)] parameter extraction [11], [18]–[26], well-known undesired RS inter- and intra-image radiometric changes are due to the following:

1) changes in instrumental conditions;
2) changes in solar illumination due to changes in the sun's position and in the Earth–sun distance;
3) atmospheric effects;
4) changes in solar illumination due to topographic influences.

To normalize the aforementioned sources 1)–4) of radiometric change, a standard Cal/Val-related protocol for RS image preprocessing should comprise steps 1) and 2), which are described next.

1) Radiometric calibration and atmospheric correction. It comprises a sequence of three steps.
   a) *Absolute radiometric calibration* [27], namely, the linear transformation of DNs into nonnegative top-of-atmosphere (TOA) radiance ($TOARD_T$) values $\geq 0$, where the subscript $T$ means terrain, i.e., $TOARD_T$ values are affected by topographic effects. This first calibration step depends on offset and gain calibration parameters retrieved from calibration metadata files accounting for instrumental conditions.
   b) Nonlinear transformation of $TOARD_T$ values into TOA reflectance ($TOARF_T$) values belonging to range [0, 1], where influences of the sun zenith angle (as a function of the time of RS data acquisition and position of the RS image footprint) and of the Earth–sun distance (as a function of the time of RS data acquisition) are normalized [24]. In the rest of this paper, this step is considered mandatory and preliminary to topographic normalization.
   c) When atmospheric effects are taken into account, the transformation of either $TOARD_T$ or $TOARF_T$ values into terrain radiance $L_T$ values $\geq 0$ or terrain reflectance $\rho_T$ values belonging to range [0, 1] [28]. In existing literature, some authors recommend the concurrent application of topographic and atmospheric correction [29] while other authors and commercial RS image-processing software toolboxes,

such as [6], recommend applying RS image atmospheric correction prior to topographic normalization. Atmospheric correction is a typical ill- or poorly posed problem requiring ancillary data (summary statistics) to be collected at several locations within the RS image footprint at the time of RS image acquisition, which are rarely available in practice. Consequently, atmospheric correction is very difficult to solve and requires the user's supervision to make it better posed [6]. In this paper, ill-posed atmospheric correction is considered optional (therefore, it is ignored in practice) by an RS image spectral-rule-based decision-tree preliminary classifier (SRC) requiring as input a multispectral (MS) image radiometrically calibrated into $TOARF_T$ values, which are considered a parent class of surface reflectance $\rho_T$ values, i.e., $TOARF_T \supseteq \rho_T$ (see Sections III-A and IV-A2).

2) RS image topographic correction (TOC), also called topographic normalization, whose aim is to compensate for changes in terrain exposure to direct sunlight, i.e., to transform $TOARF_T/L_T/\rho_T$ values into $TOARF_H/L_H/\rho_H$ values where the index $H$ identifies a horizontal-like surface. Although it has been investigated for at least 20 years, the TOC problem has not yet been solved satisfactorily due to its circular nature [6], [18], [29]–[44]. While an automatic classification of an RS MS image must rely upon well-behaved input data, realistic TOC approaches must account for non-Lambertian (anisotropic) surface reflectance as a function of structural landscape characteristics such as surface roughness, which is land cover class specific. In other words, realistic non-Lambertian TOC (NLTOC) systems must incorporate the "stratified" or "layered" approach. In RS common practice, the exploitation of stratified NLTOC (SNLTOC) approaches is limited by the need for *a priori* knowledge of land-cover-class-specific surface roughness. To overcome this limitation, "more research regarding the use of better stratification methods" is strongly encouraged [37, p. 2130], [38, p. 294].

To summarize, an original operational automatic solution to the aforementioned circular SNLTOC problem 2) stems from the *a priori* availability of a classification map automatically generated from an RS image well behaved in agreement with the aforementioned resolution 1). On the contrary, several land-cover-class- or unsupervised data-cluster-specific SNLTOC applications found in existing literature ignore or neglect the necessary, although not sufficient, radiometric calibration requirement for automating data processing. As a consequence, these SNLTOC applications adopt a manual or semiautomatic scene-by-scene data understanding approach. For example, in [43], an extended pixel-based $k$-means clustering algorithm, capable of detecting automatically the number $k$ of unlabeled data clusters, is employed for preliminary stratification (slicing). One-class (vegetation) [31], [42], two-class (vegetation/nonvegetation and forest/nonforest) [34]–[36], or three-class (snow/vegetation/nonvegetation) [37], [38] image strata are generated by preliminary image photointerpretation [36], image feature [e.g., normalized difference vegetation index (NDVI)] thresholding [34], [35], or semiautomated two-stage hybrid data-learning image-classification approaches [37], [38]. In addition, in [34] and [35], a dichotomous digital elevation model (DEM)-driven terrain slope thresholding is adopted where slopes below 10°, which include horizontal surfaces, are excluded from SNLTOC. In [44], ten strata based on DEM-driven slope ranges are generated irrespective of land cover types. Next, ten stratum-specific Minnaert coefficients (refer to Section III-B2b) are estimated image-wide and interpolated. Finally, pixel-based Minnaert coefficients are estimated from the interpolation curve to be employed in a pixel-based SNLTOC approach. Unfortunately, the correlation of surface roughness, relevant to the TOC problem, with empirical DEM-derived stratification (slicing) criteria independent of land cover types is expected to be moderate or low.

The original contribution of this paper to existing knowledge on the TOC subject is fourfold. First, Lambertian TOC (LTOC), NLTOC, and SNLTOC approaches found in existing literature are critically revised, which provides this paper with a significant survey value. Second, an original combination of automatic subsymbolic and symbolic (semantic) stratification methods suitable for developing an operational SNLTOC system are proposed in line with recommendations found in [37] and [38]. The novel stratification strategy combines: 1) four subsymbolic (asemantic) solar illumination layers, namely, self-shadows, horizontal surfaces, slopes facing the sun, and slopes facing away from the sun, generated from a DEM and the sun zenith and azimuth angles at the time of RS data acquisition and 2) symbolic (semantic) strata generated from a spaceborne MS image radiometrically calibrated into $TOARF_T \supseteq \rho_T$ values by a fully automated SRC system of systems presented and discussed in related papers [21]–[23], [45]. Third, this paper presents a novel operational automatic two-stage SNLTOC approach capable of satisfying the system requirements a)–h) listed previously to be considered eligible for use in an operational satellite-based measurement system. To the best of our knowledge, no alternative operational solution to the circular MS image TOC problem can be found in existing literature. Fourth, a novel set of SNLTOC quality indexes is proposed.

Due to its degree of novelty in agreement with the new QA4EO guidelines, this paper is of potential interest to the segment of the RS community involved with automating the quantitative analysis of RS data, e.g., in the framework of the ongoing GEOSS and GMES international programs.

This paper is structured as follows. Section II introduces the terms and symbols adopted in the rest of this paper. In Section III, previous works related to the TOC problem are surveyed. The novel operational two-stage SNLTOC system is presented in Section IV. Study areas, testing images, and ancillary data employed in the experimental session are described in Section V. Methods for the quantitative assessment of alternative SNLTOC algorithms are discussed in Section VI. Quantitative and qualitative SNLTOC results are collected and discussed in Section VII. Final conclusions are proposed in Section VIII.

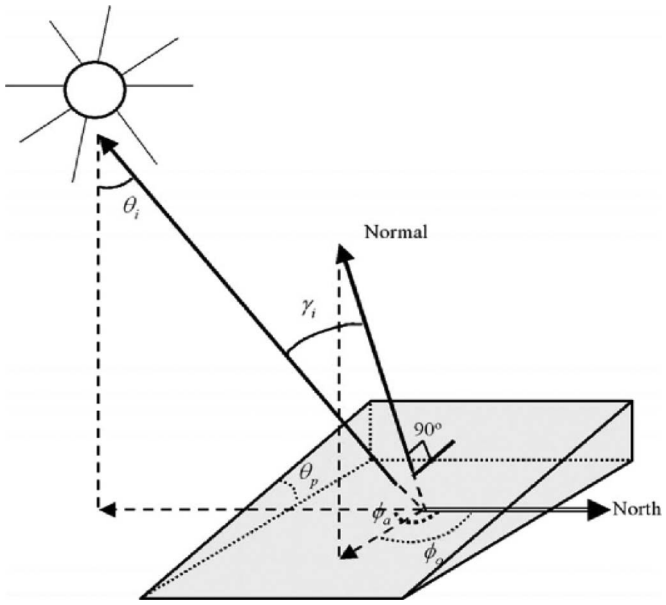


Fig. 1. Taken from [29]. The angles involved in the computation of the pixel-based illumination $IL(n) = \cos\gamma_i(n) = (1),\ n = 1, \ldots, N$, where $N$ is the total number of pixels. The adopted symbols mean the following: 1) $\theta_i$ (in this figure) $= \theta_z$ (in the rest of this paper) $\in [0°, 90°]$ is the solar zenith angle, equal to (90°—sun's elevation angle); 2) $\phi_a \in [0°, 360°]$ is the solar azimuth angle; 3) $\theta_p(n) \in [0°, 90°]$ is the pixel-based slope angle computed from the DEM exclusively, i.e., irrespective of the sun's zenith and azimuth angles; and 4) $\phi_0(n) \in [0°, 360°]$ is the pixel-based aspect angle computed from the DEM exclusively, i.e., irrespective of the sun's zenith and azimuth angles.

## II. Definitions and Symbols

The per-pixel *solar incident angle*, $\gamma_i(n) \in [0°, 180°]$, $n = 1, \ldots, N$, where $N$ is the total number of pixels in an MS image, is defined as the angle between the normal to the ground and the sun's rays (refer to Fig. 1, which is selected from RS literature). The cosine of the solar incident angle is called *illumination*, i.e., $IL(n) = \cos\gamma_i(n) \in [-1, 1]$, $n = 1, \ldots, N$. Given the sun zenith angle $\theta_z \in [0°, 90°]$, the sun azimuth angle $\phi_a \in [0°, 360°]$, and a DEM of the same size and spatial resolution as the RS image to be topographically normalized, the pixel-based illumination value $IL(n),\ n = 1, \ldots, N$, is computed as follows [29], [31], [34], [35], [37], [38], [44]:

$$\begin{aligned} IL(n) = \cos\gamma_i(n) &= \cos\theta_p(n)\cos\theta_z \\ &+ \sin\theta_p(n)\sin\theta_z\cos\left(\phi_a - \phi_0(n)\right), \\ IL(n) &\in [-1, \quad 1];\ n = 1, \ldots, N \end{aligned} \tag{1}$$

where the following are true (see Fig. 1).

1) $\theta_i$ (in Fig. 1) $= \theta_z$ (in the rest of this paper) $\in [0°, 90°]$ is the *solar zenith angle* equal to (90°—sun's elevation angle). It is either provided by the RS image metadata file or can be computed from the 1) image acquisition date and time and 2) (average) image-specific or pixel-based latitude/longitude spatial coordinates.
2) $\phi_a \in [0°, 360°]$ is the *solar azimuth angle* defined as the angle between the line from the observer to the sun projected on the ground and the line from the observer due north in a clockwise direction. It is either provided by the RS image metadata file or can be computed from the 1) image acquisition date and time and 2) (average) image-specific or pixel-based latitude/longitude spatial coordinates.
3) $\theta_p(n) \in [0°, 90°]$ is the pixel-based *slope angle* computed from the DEM exclusively, i.e., irrespective of the solar zenith and azimuth angles. It can easily be proved that the per-pixel slope $\theta_p(n)$ can be alternatively defined as the angle between the normal to the surface and the direction to the zenith [46], although this angle is confused with the sun zenith angle $\theta_z$ in [42, Fig. 2].
4) $\phi_0(n) \in [0°, 360°]$ is the pixel-based *aspect angle* measured clockwise from the north. It is computed from the DEM exclusively, i.e., irrespective of the solar zenith and azimuth angles.

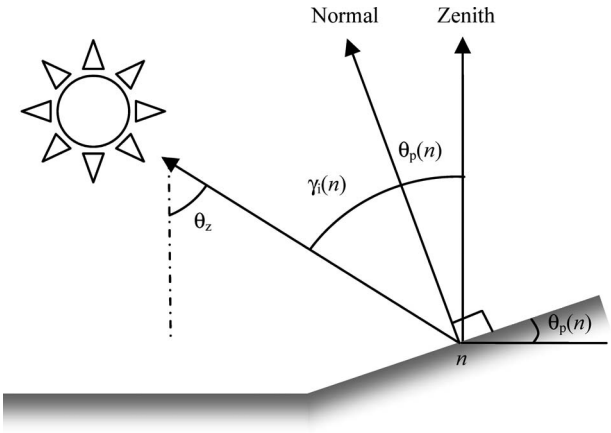


Fig. 2. If $\phi_a = \phi_0(n)$, then (1) becomes $\theta_z = \gamma_i(n) + \theta_p(n),\ n \in \{1, N\}$.

Equation (1) implies the following.

1) For a horizontal surface, such that $\theta_p(n) = 0,\ n \in \{1, N\}$, equality $\gamma_i(n) = \theta_z$ always holds.
2) If the per-pixel aspect angle is equivalent to the sun azimuth angle, i.e., $\phi_0(n) = \phi_a$, then (1) becomes (see Fig. 2)

$$\theta_z = \gamma_i(n) + \theta_p(n), \qquad \text{if } \phi_0(n) = \phi_a;\ n \in \{1, N\}. \tag{2}$$

3) If $\phi_0(n) = \phi_a$, i.e., if (2) holds, AND $\theta_p(n) = \theta_z$, $n \in \{1, \ldots, N\}$, then $\gamma_i(n) = 0$; thus, $IL(n) = 1$, i.e., this slope faces the sun perfectly.

According to the $IL(n)$ definition provided previously, the aim of TOC can be considered as a compensation for changes in the solar incident angle due to topographic influences. Several implications stem from this general definition.

It is well known that the solar irradiance (energy) at each terrain point has two components comprising three terms [19], [46], [47]: 1) a direct solar irradiance, called *sunlight* [18], and 2) an indirect [46] or diffuse [40] solar irradiance comprising the following two components. First, in nonflat terrain areas, light is reflected from other objects (e.g., adjacent slopes in rugged terrain) before being reflected from the pixel under consideration; this first component is called *reflected terrain radiance* and is null in flat terrain [6]. Second, in both flat and rugged terrain, radiation is reflected from the neighborhood of

the pixel under consideration, and next, it is scattered by the atmosphere into the viewing direction; this second component is called *skylight* [18] or *adjacency radiance* [6]. The contribution of indirect illumination to the radiance reflected by the target terrain area subject to direct illumination is relatively low, particularly in a flat terrain [48]. On *sunlit (sunny) slopes*, both direct and indirect light sources provide their contribution to the energy at the sensor, whereas on sun-shaded *(shady) slopes* direct sunlight at the surface is occluded.

In spite of their common use, the two terms *sunlit slopes* and *sun-shaded slopes*, which are totally exhaustive and mutually exclusive, suffer from vague or ambiguous definitions in RS literature. For example, in [29, p. 1056], shaded areas are defined as "slopes showing less than expected reflectance, whereas in sunny areas, the effect is the opposite." In [31], the term sun-shaded or shady slope is considered a synonym of slope facing away from the sun while the term sunny slope is used interchangeably with slope facing the sun. A formal definition of sun-shaded slopes and sunlit slopes either facing the sun or facing away from the sun as a function of the pixel-based solar incident angle $\gamma_i(n) \in [0°, 180°]$, $n = 1, \ldots, N$, and the solar zenith angle $\theta_z \in [0°, 90°]$ is provided in Section IV-A1.

To summarize, despite some confusion in the definitions of sun-shaded slopes and sunlit slopes either facing the sun or facing away from the sun found in RS literature, an alternative definition of traditional LTOC (isotropic) and NLTOC (anisotropic) methods (see Section I) refers to compensation for changes in terrain exposure to the direct (sunlight) component of solar energy at the surface. This is tantamount to saying that LTOC and NLTOC methods transform radiance (respectively, reflectance) values of sunlit slopes either facing the sun or facing away from the sun into radiance (respectively, reflectance) values of sunlit horizontal-like surfaces.

This latter definition of LTOC and NLTOC methods is not trivial. It means that, in slopes occluded from the sun, illuminated by no sunlight, LTOC and NLTOC methods cannot be applied. Rather, shaded slopes require a physically based surface-reflectance model (whose aim is to link surface properties with sensor-measured radiance) specific for skylight and reflected terrain irradiance [19], [42], [46]–[48]. If the aforementioned definition holds, i.e., if LTOC and NLTOC methods have nothing to do with shaded slopes, then the assessment of NLTOC methods across sunlit and shadow areas, such as that proposed in [39] and, perhaps [31], makes no theoretical sense.

## III. Previous Works

This section provides a summary of related works on the following subjects:

1) radiometric calibration of DNs into $TOARF_T \supseteq \rho_T$ values, which are required as input by the SRC first stage of the original two-stage SNLTOC method proposed in Section IV;
2) traditional methods for reducing topographic effects requiring no ancillary data;
3) LTOC, NLTOC, and SNLTOC methods requiring ancillary data (e.g., a DEM).

### A. Radiometric Calibration and Atmospheric Correction

Although it is often ignored in common practice by RS scientists and practitioners in disagreement with the QA4EO guidelines, radiometric calibration, which is the transformation of dimensionless DNs into a unit of measure related to a community-agreed radiometric scale, achieves the following objectives well known by a significant portion of existing literature and clearly acknowledged by international EO programs such as GEOSS and GMES (see Section I).

1) It ensures the harmonization and interoperability of multisource observational data and derived products such as those required by the ongoing GEOSS and GMES projects [12]–[14].
2) It makes RS data well behaved and well understood [11], which paves the way to automating the quantitative analysis of EO data [19], [24].

The first step in radiometric calibration, which is the so-called absolute radiometric calibration [27], is the linear transformation of a pixel value $DN(n,b) \geq 0$, with $n = 1, \ldots, N$ and $b = 1, \ldots, Bnd$, where $N$ is the total number of pixels and $Bnd$ is the number of spectral channels (bands), into a $TOARD_T$ value $TOARD_T(n,b) \geq 0$, expressed in a radiometric unit of measure, either $\mathrm{W}/(\mathrm{m}^2 \times \mathrm{sr} \times \mu\mathrm{m})$ (e.g., in the spaceborne Landsat, Satellite Pour l'Observation de la Terre (SPOT), Advanced Spaceborne Thermal Emission and Reflection (ASTER), and QuickBird optical sensors) or $\mathrm{mW}/(\mathrm{cm}^2 \times \mathrm{sr} \times \mu\mathrm{m})$ (e.g., in the spaceborne IKONOS and Indian RS Satellite (IRS) optical sensors) [6], as a function of the gain $G(b) \geq 0$ and offset $O(b) \geq 0$ calibration parameters for band $b = 1, \ldots, Bnd$, to be retrieved from the RS metadata file. For example, in the case of SPOT-1/-5 imagery [49]

$$0 \leq TOARD_T(n,b) = [DN(n,b)/G(b)] + O(b), \quad n = 1, \ldots, N;\ b = 1, \ldots, Bnd \tag{3}$$

where gain and offset parameters are identified, respectively, as "⟨PHYSICAL_GAIN⟩" and "⟨PHYSICAL_BIAS⟩" in the SPOT metadata digital image map (DIMAP) file format.

The model for obtaining dimensionless true terrain reflectance $\rho_T(n, \lambda, t, lat, long) \in [0,1]$ from the spectral radiance at the sensor's aperture $TOARD_T(n, \lambda)$ may be expressed as follows [29]:

$$\rho_T(n,\lambda,t,lat,long) = \frac{\pi \cdot d(t)^2 \cdot \left(\frac{TOARD_T(n,\lambda) - L_a(\lambda)}{\tau_{\mathrm{uw}}(\lambda)}\right)}{ESUN(\lambda) \cdot \cos(\theta_z(t,lat,long)) \cdot \tau_{\mathrm{dw}}(\lambda) + E_d(n,\lambda)} \in [0,1], \quad n = 1, \ldots, N \tag{4}$$

where $\lambda$ is the electromagnetic wavelength, $(lat, long)$ is the pixel position in geographic coordinates, and $d(t)$ is the Earth–sun distance in astronomical units to be interpolated from values found in literature as a function of the viewing day and time $t$, transformed into a Julian day value in

the range $\{1, 365\}$, such that $d(t)$ approximately belongs to range $1 \pm 3.5\%$ [50]. $L_a(\lambda) \geq 0$ is the *atmospheric upwelling radiance* scattered at the sensor by the atmosphere (called *airlight* [18], equivalent to an additive term to be assessed by dark-object subtraction techniques: If, by definition of a dark object, $\rho_T = (4) = 0$, then the unknown variable $L_a$ is equal to the measured $TOARD_T$ value [28]), and $E_d(n, \lambda) \geq 0$ is called *diffuse irradiance at the surface* [29], *ambient light*, or *indirect illumination* [46], contains no information on the surface properties of the pixel, and comprises two components: 1) in nonflat terrain areas, *reflected terrain radiance* [6] or 2) in both flat and rugged terrain, *skylight* [18] or *adjacency radiance* [6] (also refer to Section II). Overall, $E_d(\lambda)$ changes with wavelength; it can provide a relevant contribution to incident radiance in rugged terrains [28], [29], but is relatively low in flat terrains [48]. Furthermore, $\tau_{\mathrm{uw}}(\lambda) \in [0, 1]$ and $\tau_{\mathrm{dw}}(\lambda) \in [0, 1]$ are the *path atmospheric transmittances of the upwelling* (ground surface–sensor path) and *downwelling* (sun–ground surface path) *flows*, respectively, and $ESUN(\lambda)$ is the mean solar exoatmospheric (TOA, planetary) irradiance found in literature [29] (e.g., in the SPOT metadata DIMAP file format, parameter $ESUN(\lambda)$ is identified as "⟨SOLAR_IRRADIANCE_VALUE⟩"). $\theta_z \in [0°, 90°]$ is the sun's zenith angle in degrees (also refer to Section II), typically provided in the image metadata file or computed from the data acquisition time $t$ and per-scene or pixel-based latitude–longitude coordinates. The term $[ESUN(\lambda) \cdot \cos(\theta_z)]$ is called *sunlight* [18] or *direct illumination* [29] and represents the only radiation component reflected from the pixel under consideration that contains "pure" information on the surface properties of the pixel (also refer to Section II).

In (4), atmospheric effects are modeled by atmospheric parameters $\tau_{\mathrm{uw}}(\lambda) \in [0, 1]$, $\tau_{\mathrm{dw}}(\lambda) \in [0, 1]$, and $L_a(\lambda) \geq 0$. To retrieve these atmospheric parameters, ancillary data (summary statistics), which are rarely available in practice, should be collected at several locations within the RS image footprint at the time of RS image acquisition. This means that the problem of atmospheric correction is typically ill or poorly posed. Consequently, it is very difficult to solve and requires user's supervision to make it better posed [6] (also refer to Section I). In common practice, Baraldi has observed that RS images radiometrically calibrated into $\rho_T$ values by several EU institutions mentioned later in this paper are unreliable, namely, they are affected by spectral distortion causing scene-derived surface-reflectance spectra to disagree with reference surface-reflectance signatures found in existing literature (e.g., refer to [81, p. 273]) or in public domain spectral libraries such as the U.S. Geological Survey (USGS) mineral and vegetation spectral libraries, the Johns Hopkins University spectral library, and the Jet Propulsion Laboratory mineral spectral library [6], [56].

A reduction in interscene variability across time, space, and sensors can be achieved by a simplification of (4) into dimensionless $TOARF_T$ values belonging to the range [0, 1]. Starting from (4), $TOARF_T$ values are computed as a function of the electromagnetic wavelength for spectral band $b = 1, \ldots, Bnd$, by considering the following: 1) atmospheric effects negligible, such as for relatively "clear" scenes where $\tau_{\mathrm{uw}}(\lambda) \approx 1$, $\tau_{\mathrm{dw}}(\lambda) \approx 1$, and $L_a(\lambda) \approx 0$ [6], [29], and 2) flat and/or nonflat neighboring terrain effects negligible, i.e., $E_d(\lambda) \approx 0$ [29]. Thus, (4) becomes

$$TOARF_T(n, b, t, lat, long) = \frac{\pi \cdot d(t)^2 \cdot TOARD_T(n, b)}{ESUN(b) \cdot \cos\left(\theta_z(t, lat, long)\right)} \in [0, 1], \quad n = 1, \ldots;\ N, b = 1, \ldots, Bnd. \tag{5}$$

Although often overlooked by RS scientists and practitioners, it is well known in existing literature that the radiometric calibration of DNs into $TOARF_T = (5)$ values features several advantages over the radiometric calibration into $TOARD_T = (3)$ values.

1) The former is recommended before calculating various vegetation indices (VIs) [19]. In fact, while the relationships between the LAI and a great variety of well-known VIs calculated from $TOARD_T$ values are nonlinear, the relationships between LAI and the same VIs calculated from $TOARF_T$ are, in several cases, reasonably linear.
2) By accounting for seasonal and latitudinal differences in solar illumination, the former guarantees better interimage comparability/interpretation (classification, mapping) across time, space, and sensors [24], [25], which is in line with the goals of EO data harmonization and interoperability required by the GEOSS and GMES programs.
3) The former is more consistent with the scenario of low- and high-level image-processing capabilities to be developed onboard future intelligent fourth-generation EO satellites (FIEOSs) [52], [53]. The development of FIEOS, where onboard integration of sensors, data processors, and communication systems is pursued, should become a major scientific challenge to the RS community within the next ten years [52].

It is noteworthy that, when neighboring terrain effects are omitted, i.e., $E_d(\lambda) \approx 0$, then $\rho_T|_{Ed(\lambda)\approx 0} = (4)|_{Ed(\lambda)\approx 0} = f_1(TOARD_T)|_{Ed(\lambda)\approx 0}$ can be expressed as $\rho_T = |_{Ed(\lambda)\approx 0} = f_2(TOARF_T)$ as follows:

$$\begin{aligned}
\rho_T(n, \lambda, t, lat, long)|_{E_d(\lambda)\approx 0} &= (4)|_{E_d(\lambda)\approx 0} \in [0, 1] \\
&= TOARF_T(n, b, t, lat, long) \\
&\quad \times \frac{1}{\tau_{\mathrm{uw}}(\lambda) \cdot \tau_{\mathrm{dw}}(\lambda)} \\
&\quad - \frac{\pi \cdot d(t)^2}{ESUN(\lambda) \cdot \cos\left(\theta_z(t, lat, long)\right)} \\
&\quad \times \frac{L_a(\lambda)}{\tau_{\mathrm{uw}}(\lambda) \cdot \tau_{\mathrm{dw}}(\lambda)} \\
&= (5) \cdot AtmsphEffct_1(\lambda) \\
&\quad - \frac{\pi \cdot d(t)^2}{ESUN(\lambda) \cdot \cos\left(\theta_z(t, lat, long)\right)} \\
&\quad \times AtmsphEffct_2(\lambda), \\
&\qquad n = 1, \ldots, N;\ b = 1, \ldots, Bnd
\end{aligned} \tag{6}$$

where $TOARF_T(n, b, t, lat, long) = (5) \in [0, 1]$, $AtmsphEffct_1(\lambda) = \{1/[\tau_{\mathrm{uw}}(\lambda) \cdot \tau_{\mathrm{dw}}(\lambda)]\} \geq 1$, and

$AtmsphEffct_2(\lambda) = \{L_a(\lambda)/[\tau_{\mathrm{uw}}(\lambda)\cdot\tau_{\mathrm{dw}}(\lambda)]\} \geq L_a(\lambda) \geq 0$. Vice versa

$$
\begin{aligned}
&TOARF_T(n,b,t,lat,long)\\
&\quad = (5) \in [0,1]\\
&\quad = \rho_T(n,\lambda,t,lat,long)|_{E_d(\lambda)\approx 0} \cdot [\tau_{\mathrm{uw}}(\lambda)\cdot\tau_{\mathrm{dw}}(\lambda)]\\
&\qquad + \frac{\pi \cdot d(t)^2}{ESUN(\lambda)\cdot\cos\left(\theta_z(t,lat,long)\right)} \cdot L_a(\lambda)\\
&\quad = \frac{(4)|_{E_d(\lambda)\approx 0}}{AtmsphEffct_1(\lambda)}\\
&\qquad + \frac{\pi \cdot d(t)^2}{ESUN(\lambda)\cdot\cos(\theta_z(t,lat,long))} \cdot \frac{AtmsphEffct_2(\lambda)}{AtmsphEffct_1(\lambda)}.
\end{aligned}
$$

Equation (6) shows that, if $E_d(\lambda) \approx 0$, the following are true.

1) For a clear sky condition, when $\tau_{\mathrm{uw}}(\lambda) \approx 1$, $\tau_{\mathrm{dw}}(\lambda) \approx 1$, and $L_a(\lambda) \approx 0$ [6], [29], $AtmsphEffct_1(\lambda) \approx 1$ and $AtmsphEffct_2(\lambda) \approx 0$; thus, $\rho_T = (4) \approx (6) \approx TOARF_T = (5)$, i.e., if $E_d(\lambda) \approx 0$, then surface-reflectance values can be computed from $TOARF_T$ values when atmospheric effects are 1) accounted for, i.e., scene-specific parameters $\tau_{\mathrm{uw}}(\lambda)$, $\tau_{\mathrm{dw}}(\lambda)$, and $L_a(\lambda)$ are retrieved, or 2) considered negligible. In other words, if $E_d(\lambda) \approx 0$, then $TOARF_T = (5) \supseteq \rho_T = (4) \approx (6)$; in fact, according to (6), it is possible to intuitively consider $TOARF_T(\lambda) \approx \rho_T(\lambda) + AtmsphNoise(\lambda)$, where term $AtmsphNoise$ is zero for a clear sky condition. This (obvious) concept will be further recalled by the SRC system of systems, described in Section IV-A2, adopted as the automatic preliminary classification first stage of the novel two-stage SNLTOC approach.
2) Independent of wavelength $\lambda$, when atmospheric effects are omitted (ignored), i.e., $AtmsphEffct_1(\lambda) \approx 1$ and $AtmsphEffct_2(\lambda) \approx 0$ such that $\rho_T = (4) \approx (6) \approx TOARF_T = (5)$, numerical effects of the two simplified atmospheric terms $1 \leq AtmsphEffct_1(\lambda) = 1$ and $0 \leq L_a(\lambda) \leq AtmsphEffct_2(\lambda) = 0$ tend to counterbalance each other, i.e., whereas the first approximation causes an underestimation of the true $\rho_T$ values, the second approximation does otherwise. Across wavelengths, this property improves the effectiveness of $TOARF_T$ as an estimator of the true $\rho_T$ values.
3) When wavelength $\lambda$ increases, $TOARF_T$ provides a better approximation of $\rho_T$. It is well known that light scattering due to atmospheric conditions (haze consisting of gas molecules and water droplets) and aerosols (consisting of liquid droplets and solid particles suspended in the atmosphere and generated by either natural or anthropogenic sources) is inversely proportional to the energy wavelength $\lambda$, i.e., shorter wavelengths of the spectrum are scattered more than the longer wavelengths. Thus, a visible blue (B) channel is affected by scattering across all atmospheric conditions ranging from "very clear" (where scattering is proportional to a factor $\lambda^{-4}$) to "very hazy" (where scattering is proportional to a factor $\lambda^{-0.5}$) and cloudy (where complete scattering occurs, proportional to a factor $\lambda^0$) [28]. On the contrary, in the medium infrared (MIR) wavelengths, the amount of atmospheric scattering is known to be "quite small except for very hazy atmospheres and can be considered negligible" [28, p. 476]. In these various atmospheric conditions, ranging from very clear and clear visible wavelengths to any MIR portion of the electromagnetic spectrum unless it is very hazy, atmospheric effects can be omitted (ignored), i.e., $1 \leq AtmsphEffct_1(\lambda) \approx 1$ and $0 \leq L_a(\lambda) \leq AtmsphEffct_2(\lambda) \approx 0$ in (6), such that, if $E_d(\lambda) \approx 0$, then $\rho_T = (4) \approx (6) \approx TOARF_T = (5)$.

### *B. Methods for Reducing Topographic Influences on Solar Illumination*

TOC has been widely acknowledged in existing literature for more than 20 years [6], [18], [29]–[44], [54]. While some authors have indirectly approached reflectance variations caused by topographic effects by including DEM-driven information as ancillary input bands in multiband classification [29], several methods for correcting topographic effects on solar irradiance at the surface have been proposed [6], [29]–[44], [54]. They may be grouped into two categories: 1) those based on spectral band ratios and other empirical criteria requiring no ancillary data [55] and 2) those requiring the computation of the solar incident angle $\gamma_i(n) \in [0^\circ, 180^\circ]$, $n = 1, \ldots, N$, as a function of the sun's zenith angle, the sun's azimuth angle, and a DEM of the same spatial resolution as the image to be topographically normalized. These two families of algorithms are described next.

*1) Reduction of Topographic Effects Without Ancillary Data:*

*a) Band ratioing:* In TOC methods based on band ratios, reflectance is assumed to increase or decrease to the same degree in the two bands involved in the ratio. If this hypothesis holds, then the quotient between these two bands compensate for topographic influences. Unfortunately, while this assumption applies to the incident angle whose effects are independent of wavelength, it does not apply to the diffuse irradiance at the surface $E_d(\lambda)$ [see (4)]. In addition, band ratioing causes a loss in spectral resolution, which is a drawback in MS image classification [29].

*b) Class splitting into sunlit and shaded subclasses:* A "traditional" inductive supervised data-learning approach suitable for land cover classification in mountainous terrain is to split each target land cover class into two "illuminated" and "shadow" subclasses, i.e., per-class reference samples must be acquired in sunlit and shaded areas [39]. According to [39], this classification training strategy can give classification results similar to those obtained by a supervised classification of an MS image topographically corrected by an NLTOC method applied image-wide without any preliminary stratification. However, the so-called traditional approach requires a degree of user interaction in defining possible land cover subclasses far greater than the latter. Above all, it is noteworthy that (S)NLTOC methods aim at compensating for changes in terrain exposure to direct sunlight, i.e., (S)NLTOC methods do not apply to shadow areas where diffuse light-specific reflectance models must be employed instead (refer to Section II). The automatic

detection of occluded areas in spaceborne imagery requires ancillary data, namely, a DEM, the sun's zenith angle, and the sun's azimuth angle. If this ancillary data are missing, then a manual photointerpretation of occluded areas is typically affected by commission errors with slopes facing away from the sun (refer to Section II). To conclude, (S)NLTOC approaches and supervised class splitting into sunlit and shaded subclasses are complementary rather than alternative approaches.

*c) Standard SAM:* Due to its relative insensitiveness to topographic and atmospheric effects, the spectral angle mapper (SAM) is considered a standard classifier implemented in several commercial image-processing software toolboxes such as the Environment for Visualizing Images (ENVI), licensed by ITT Industries, Inc. [56]. In a $D$-dimensional measurement (feature) space, SAM computes the spectral angle $\alpha$ formed between a reference vector from the origin $\bar{r}$, representing a reference spectrum (signature) belonging to a collection of so-called endmember spectra [56], and the vector from the origin representing an unclassified pixel $\bar{v}$. The unclassified pixel is assigned to the reference class forming the smallest angle with the pixel vector.

The vector pair in between angles is computed as [57], [58]

$$SAM(\vec{v},\vec{r}) = \arccos(\alpha) = \arccos\left(\frac{<\vec{v},\vec{r}>}{\|\vec{v}\|\cdot\|\vec{r}\|}\right) \in [0,\pi] \quad (7)$$

where $\langle\vec{v},\vec{r}\rangle = \sum_{d=1}^{D} v_d r_d$ is the dot product between vectors $\bar{v}$ and $\bar{r}$, $\|\vec{v}\| = \sqrt{\sum_{d=1}^{D}(v_d)^2}$ is the magnitude (intensity) operator, and $\cos\alpha = (\langle\vec{v},\vec{r}\rangle/\|\vec{v}\|\cdot\|\vec{r}\|) \in [-1,1]$ is the normalized dot product. It is to be noted that the so-called Cosine of the Angle Concept (CAC) classifier employs the normalized dot product in place of (7) [57]. Both SAM and CAC are invariant to linearly scaled variations of vectors $\bar{v}$ and $\bar{r}$ when they are both multiplied by a coefficient belonging to the domain of real numbers $\Re$.

The fuzzy prior knowledge exploited by SAM is the following: "spectra of the same type of surface objects are *approximately* linearly scaled versions of one another due to the atmospheric and topographic variations" [57]–[59]. According to existing literature (e.g., [60]), this statement is known to be extremely fuzzy (vague, qualitative), as shown in Fig. 3, where a set of reflectance patterns, extracted from Landsat images radiometrically calibrated into $TOARF_T$ values and belonging to the endmember collection spectra employed to develop SRC [45] (refer to Section IV-A2), can be compared.

An additional theoretical drawback of both SAM and CAC is that, by ignoring a comparison between magnitudes $\|\vec{v}\|$ and $\|\vec{r}\|$, they employ no intensity (brightness, panchromatic [61]) information criteria in their decision rule. This information loss is well known in existing literature where, starting from SAM, alternative transformed distance concepts were proposed, e.g., refer to [62].

*2) TOC Methods Exploiting Ancillary Data:* To estimate the flat-normalized (horizontal) reflectance $TOARF_H(n,b)$, where $n = 1,\ldots,N$ and $b = 1,\ldots,Bnd$, from an input MS image radiometrically calibrated into $TOARF_T(n,b)$ values, with $n = 1,\ldots,N$ and $b = 1,\ldots,Bnd$, several TOC methods require the precomputation of the pixel-based illumination, $IL(n) = \cos(\gamma_i(n)) = (1) \in [-1,1]$, $n = 1,\ldots,N$, as a function of the sun's zenith angle $\theta_z \in [0°, 90°]$, the sun's azimuth angle $\phi_a \in [0°, 360°]$, and a DEM of the same spatial resolution as the MS image to be topographically normalized (see Section II). These TOC approaches can be grouped into

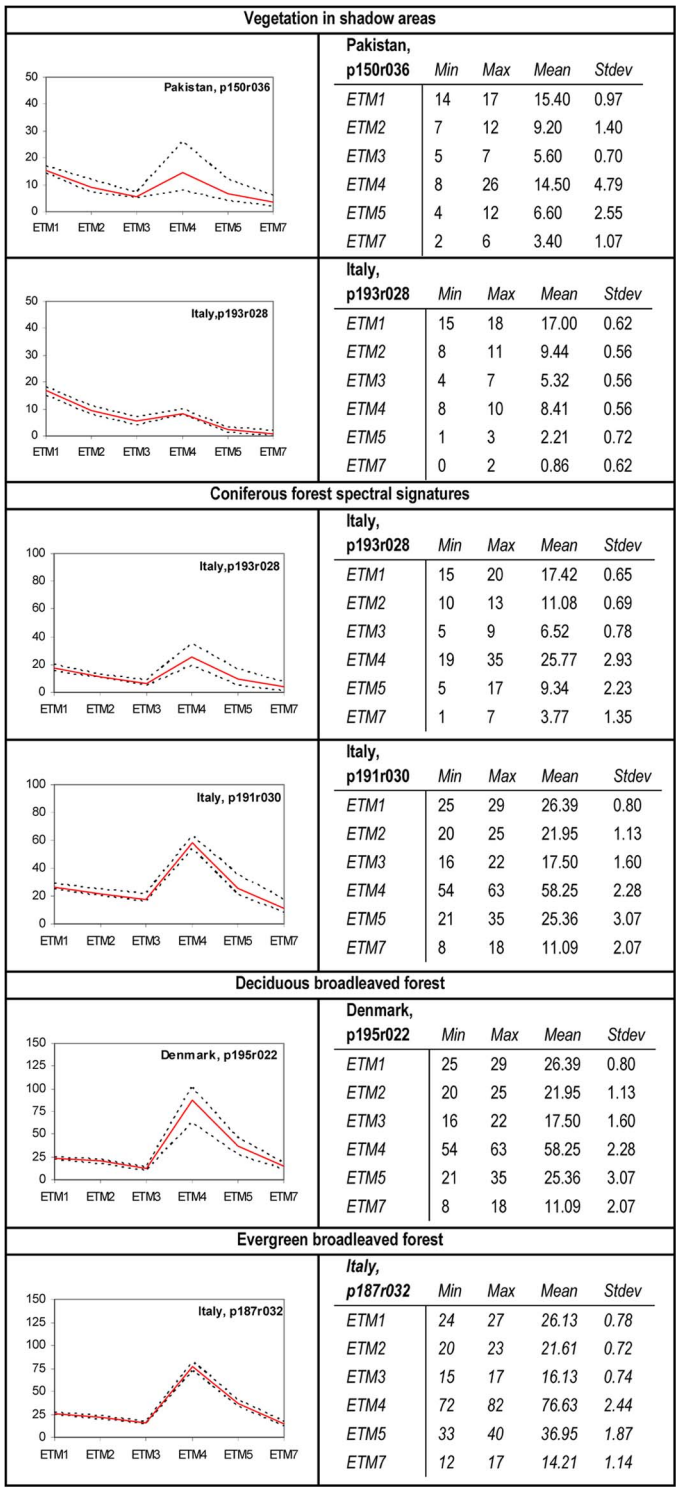


Fig. 3. Endmember collection spectra employed to design the decision rule set in SRC [45]. Spectral signatures in $TOARF_T$ values, belonging to the continuous range [0, 1] linearly scaled onto the discrete range $\{0, 255\}$ (with a discretization error equaling 0.4%), are extracted from Landsat-7 ETM+ images.

the following two subcategories, depending on whether they assume the surface reflectance as being independent of the observation and incident angles (see Section I).

1) LTOC (isotropic) approaches. The Lambertian assumption is very simple but unrealistic because most land cover types are rugged and feature non-Lambertian behavior.
2) NLTOC (anisotropic) approaches comprising either nonstratified or stratified (SNLTOC) methods. On a theoretical basis, the bidirectional reflectance distribution function (BRDF) describes how reflectance varies in each land cover type by considering all possible angles of incidence and observation. In practice, the determination of BRDF is extremely complex. To provide a simplified estimation of a non-Lambertian spectral reflectance model, NLTOC and SNLTOC methods have been developed starting from different assumptions about the real (3-D) scene depicted in an (2-D) MS image.

Ordinary LTOC and NLTOC methods are surveyed and discussed next to highlight several inconsistencies found in existing literature.

*a) LTOC (isotropic) methods:* The simplest and best known LTOC method is the cosine LTOC equation. Widely adopted in most image-processing software toolboxes [56], it is computed as follows [29], [31], [34], [35]:

$$TOARF_H(n,b) = TOARF_T(n,b)\left(\frac{\cos\theta_z}{\cos\gamma_i(n)}\right), \quad n = 1,\ldots,N;\ b = 1,\ldots,Bnd \quad (8)$$

where incident angle $\gamma_i(n) \in [0^\circ, 180^\circ]$, and thus, $\cos\gamma_i(n) = IL(n) \in [-1,+1]$ (see Section II), and where the sun's zenith angle $\theta_z \in [0^\circ, 90^\circ]$ is used to take into account the nonverticality of direct sun rays. Several considerations stem from (8).

1) In (8), the larger the incident angle $\gamma_i(n)$ in range $[0^\circ, 90^\circ]$, i.e., the lower the per-pixel illumination $IL(n)$ in range [0, +1], the higher the corrected reflectance $TOARF_H(n,b)$.
2) When $\gamma_i(n) \in (90^\circ, 180^\circ]$, i.e, $IL(n) \in [-1, 0)$, then (8) $< 0$, which has no physical meaning. To the best of our knowledge, the sole explicit strategy on employing (8) when $\gamma_i(n) \in (90^\circ, 180^\circ]$ is found in [36], where it is written that, if $\gamma_i(n) \geq 85^\circ$, then the pixel information value is low and topographic normalization does not help. This is tantamount to saying that, when $\gamma_i(n) \in [85^\circ, 180^\circ]$, (8) is not applied.
3) For a horizontal surface, where $\gamma_i(n) = \theta_z \in [0^\circ, 90^\circ]$ (see Section II), (8) becomes $TOARF_H(n,b) = TOARF_T(n,b)$, i.e., the measured terrain surface $TOARF_T(n,b)$ is left unchanged after topographic normalization. This means that, when (8) is adopted, horizontal surfaces can be skipped in topographic normalization to save computation time.

In contrast with the RS image preprocessing protocol recommended in Section I, if (8) is meant to be applied to $TOARD_T$ rather than to $TOARF_T$ values, i.e., when topographic normalization is applied in series with absolute radiometric calibration [see (3)] but before the transformation of $TOARD_T$ into $TOARF_T$ values [refer to (5)], (8) becomes [34], [35]

$$TOARD_H(n,b) = \frac{TOARD_T(n,b)}{\cos\gamma_i(n)}, \quad \text{with } n = 1,\ldots,N;\ b = 1,\ldots,Bnd \quad (9)$$

where incident angle $\gamma_i(n) \in [0^\circ, 180^\circ]$; thus, $\cos\gamma_i(n) = IL(n) \in [-1,+1]$ (see Section II). The following are worth noting.

1) According to [36], when $\gamma_i(n) \in [85^\circ, 180^\circ]$, (9) should not be applied (see aforementioned comments).
2) If $\gamma_i(n) \in [0^\circ, 90^\circ]$, i.e., $IL(n) \in [0,+1]$, then (9) shows that $TOARD_H(n,b) \geq TOARD_T(n,b)$ $n \in \{1, N\}$ and $b = 1,\ldots,Bnd$. Condition $\gamma_i(n) \in [0^\circ, 90^\circ]$ includes horizontal surfaces, where $\gamma_i(n) = \theta_z \in [0^\circ, 90^\circ]$ (refer to Section II), such that (9) becomes $TOARD_H(n,b) = (TOARD_T(n,b)/\cos\theta_z) \geq TOARD_T(n,b)$. This means that, unlike (8), whose effect on $TOARF_T$ values belonging to horizontal surfaces is null, (9) must be applied to the whole $TOARD_T$ image, including horizontal surfaces. The reason for this difference between (8) and (9) is that, in line with the RS image preprocessing protocol recommended in Section I, (8) is applied in series with (5), such that the denominator $\cos(\theta_z)$ employed in (5) is elicited by the numerator $\cos(\theta_z)$ adopted by (8).

Unfortunately, differences between (8) and (9) appear to be not always understood in literature. For example, in [31], (8) is wrongly referred to as radiance rather than reflectance while (9) is incorrectly identified as topographically normalized reflectance rather than radiance in [44]. More dangerous than that, in [39, p. 3839], (9) is not applied to horizontal surfaces.

*Limitations:*

1) Several authors have shown that (8) and (9) overcorrect the image in areas of "low" $IL(n)$ values [29], [34], [35]. The empirical (fuzzy) nature of this statement can be better formalized as follows. In (8) and (9), low $IL(n)$ values should be identified as values where $IL(n) = \cos\gamma_i(n) < \cos\theta_z$ with $\theta_z \in [0^\circ, 90^\circ]$, i.e., $\gamma_i(n) \in (\theta_z, 180^\circ]$. This condition corresponds to 1) nonhorizontal nonoccluded surfaces facing away from the sun if $\gamma_i(n) \in (\theta_z, 90^\circ]$ and 2) occluded surfaces belonging to shadow casters (self-shadows) if $\gamma_i(n) \in (90^\circ, 180^\circ]$ (see Section IV-A1).
2) Topographic normalization introduced by (8) and (9) is wavelength independent. This assumption is unrealistic because diffuse irradiance at the surface [refer to term $E_d(\lambda)$ in (4)] is highly wavelength dependent [28], [29].
3) Most land cover types are rugged and feature non-Lambertian behavior.

*b) NLTOC (anisotropic) methods:* NLTOC and SNLTOC methods employ different hypotheses to constrain the problem of surface-roughness estimation. In particular, NLTOC methods adopt the following hypothesis [29].

*Hypothesis 1:* The pixel-based corrected horizontal (flat-normalized) reflectance $TOARF_H(n,b)$, where $n = 1,\ldots,N$

and $b = 1, \ldots, Bnd$, is assumed to be per-band image-wide constant (homogeneous), i.e., $TOARF_H(n, b) = \text{Constant}(b)$, where $n = 1, \ldots, N$ and $b = 1, \ldots, Bnd$. This is tantamount to saying that the whole image belongs to a single land cover class.

Some authors consider *Hypothesis 1* so poorly constrained that unrealistic but simpler LTOC methods are preferred to NLTOC approaches [29]. To replace *Hypothesis 1* with a more realistic constraint, SNLTOC approaches assume the following.

*Hypothesis 2:* Before topographic normalization takes place, the input MS image radiometrically calibrated into $TOARF_T(n, b)$ values, where $n = 1, \ldots, N$ and $b = 1, \ldots, Bnd$, must be provided with an *exhaustive and mutually exclusive partition (map)* equivalent to a *land-cover-class-specific surface-roughness stratification* $Strtm(n) \in \{1, S\}$, $n = 1, \ldots, N$, where $S$ is the total number of strata, such that $S \geq C \geq 1$, where $C$ is the total number of land cover classes (excluding class "unknown") predetected in the input image $TOARF_T(n, b)$, where $n = 1, \ldots, N$ and $b = 1, \ldots, Bnd$. In other words, an SNLTOC approach assumes that, first, each predefined stratum $s \in \{1, S\}$ features a typical or "average" surface roughness. Second, the map-conditional topographically corrected (horizontal) reflectance $TOARF_H[n, b|Strtm(n); n = 1, \ldots, N, \quad b = 1, \ldots, Bnd, \quad Strtm(n) \in \{1, S\}]$ is assumed to be per-band per-stratum piecewise constant, i.e., $TOARF_H[n, b|Strtm(n) = s; n \in \{1, N\}, s = 1, \ldots, S, b = 1, \ldots, Bnd] = \text{Constant}[b, s; s = 1, \ldots, S, b = 1, \ldots, Bnd]$.

In practice, SNLTOC approaches are limited by the need for *a priori* knowledge of the spatial structure (namely, roughness) of the landscape (refer to Section I) [37]. For example, several papers in literature employ SNLTOC approaches capable of satisfying *Hypothesis 2*, where the number of target classes $C$ is as coarse as one to three [31], [34]–[39], [43]. It is noteworthy that the stratification strategy adopted in [44], which is DEM driven but land cover class independent, does not satisfy the aforementioned *Hypothesis 2*.

*3) Minnaert Equation:* In existing literature, the best known NLTOC and SNLTOC approaches are based on the ideas of Minnaert, who first proposed a semiempirical equation to assess the roughness of the moon's surface [29]. According to Minnaert's ideas, the LTOC equation (8) is revised as follows in the so-called Minnaert NLTOC equation [29]:

$$TOARF_H(n, b) = TOARF_T(n, b) \left[ \frac{\cos \theta_z}{\cos \gamma_i(n)} \right]^{K(b)}, \quad n = 1, \ldots, N; \; b = 1, \ldots, Bnd \quad (10)$$

where incident angle $\gamma_i(n) \in [0°, 180°]$, and thus, $\cos \gamma_i(n) = \text{IL}(n) \in [-1, +1]$ (see Section II), and where coefficient $K(b) \in [0, 1]$ is a dimensionless real number, called the Minnaert constant for spectral band $b = 1, \ldots, Bnd$, capable of modeling the non-Lambertian behavior of the surface due to surface roughness. If $K(b) = 1$, the surface behaves as a perfect Lambertian reflector. If $K(b) \to 0$, the surface is porous and exhibits asymmetrical diffuse scattering (which explains the low values of $K(b)$ for class forest) [36].

To estimate the value of $K(b)$ for each spectral band $b = 1, \ldots, Bnd$, (10) can be linearized as follows:

$$\begin{aligned} Y(n, b) &= \log_{10} [TOARF_T(n, b)] \\ &= \log_{10} [TOARF_H(b)] + K(b) \log_{10} \left[ \frac{\cos \gamma_i(n)}{\cos \theta_z} \right] \\ &= D(b) + A(b) \cdot X(n) \end{aligned} \quad (11)$$

where $n = 1, \ldots, N$, $b = 1, \ldots, Bnd$, and $D(b) = \log_{10}[TOARF_H(b)]$ and $A(b) = K(b)$ are the two regression coefficients of the observed reflectance values $Y(n, b) = \log_{10}[TOARF_T(n, b)]$, where $n = 1, \ldots, N$ and $b = 1, \ldots, Bnd$, versus incident angle-dependent terms $X(n) = \log_{10}[\cos \gamma_i(n) / \cos \theta_z]$, $n = 1, \ldots, N$.

In practice, estimated Minnaert constant values $K(b) > 1$ and $K(b) < 0$ indicate that the adopted regression method and its $Y(n, b)$ and $X(n)$ data sets are poor, e.g., when data sets $Y(n, b)$ and $X(n)$ feature large and unstable variations due to the presence of "outliers," namely, pixels belonging to different strata of surface roughness within the image-wide data set of observed reflectance values $TOARF_T(n, b)$, where $n = 1, \ldots, N$ and $b = 1, \ldots, Bnd$ [36]. Thus, the estimated Minnaert constant values $K(b) > 1$ and $K(b) < 0$ should be rounded to values 1 and 0, respectively, in line with [36], although this is rarely done in practice, e.g., refer to [44].

When (9) is employed in place of (8), (10) becomes

$$TOARD_H(n, b) = \frac{TOARD_T(n, b)}{[\cos \gamma_i(n)]^{K(b)}} = \frac{TOARD_T(n, b)}{IL(n)^{K(b)}}, \quad n = 1, \ldots, N; \; b = 1, \ldots, Bnd. \quad (12)$$

For the sake of completeness, the SNLTOC version of the Minnaert NLTOC equation (10) incorporates *Hypothesis 2*, defined previously, to become

$$TOARF_H(n, b|Strtm(n) = s) = TOARF_T(n, b|Strtm(n) = s) \left[ \frac{\cos \theta_z}{\cos \gamma_i(n)} \right]^{K(b,s)} \quad (13)$$

where $n \in \{1, N\}$, $b = 1, \ldots, Bnd$, $s = 1, \ldots, S$, and $k(b, s) \in [0, 1]$.

*Limitations:*

1) In their original formulation, the NLTOC equations (10) and (11) adopt the unrealistic *Hypothesis 1*. In [34], an SNLTOC version of (10) adapted to incorporate a stratified or layered approach [see (13)] performs better than the NLTOC equation (10) by improving classification accuracies of land cover types after SNLTOC.
2) In [29], (10) is found to overcorrect the $TOARF_T$ image in areas of low $IL(n)$ values, like (8) (refer to Section III-B2a).

*4) Enhanced Minnaert Equation:* In [54], the Minnaert NLTOC equation (10) was further modified to include the slope

of the terrain, which is $\theta_p(n) \in [0°, 90°]$, $n = 1, \ldots, N$, as follows [29], [34], [35]:

$$TOARF_H(n,b) = TOARF_T(n,b)\cos\theta_p(n) \times \left[\frac{\cos\theta_z}{\cos\gamma_i(n)\cos\theta_p(n)}\right]^{K(b)}, \quad n = 1,\ldots,N;\ b = 1,\ldots,Bnd \quad (14)$$

where incident angle $\gamma_i(n) \in [0°, 180°]$, and thus, $\cos\gamma_i(n) = IL(n) \in [-1, +1]$ (see Section II), $K(b) \in [0, 1]$ (as discussed previously), and $\theta_z \in [0°, 90°]$.

The NLTOC-enhanced Minnaert equation (14) for $TOARD_T$ values becomes [31], [36]–[38], [44]

$$TOARD_H(n,b) = \frac{TOARD_T(n,b)\cos\theta_p(n)}{[\cos\gamma_i(n)\cos\theta_p(n)]^{K(b)}}, \quad n = 1,\ldots,N;\ b = 1,\ldots,Bnd. \quad (15)$$

For the sake of completeness, the SNLTOC version of the enhanced Minnaert NLTOC equation (14) incorporates *Hypothesis 2*, defined previously, to become

$$TOARF_H(n,b,|Strtm(n) = s) = TOARF_T(n,b,|Strtm(n) = s) \times \cos\theta_p(n) \cdot \left[\frac{\cos\theta_z}{\cos\gamma_i(n)\cos\theta_p(n)}\right]^{K(b,s)}, \quad n \in \{1, N\};\ b = 1,\ldots,Bnd;\ s = 1,\ldots,S;\ k(b,s) \in [0,1]. \quad (16)$$

*Limitations:* According to [29] where an NLTOC approach is adopted, (14) suffers from the same limitations as the Minnaert equation (10). This conclusion is in contrast with [35], where (14) employed in an NLTOC approach performs better than the ordinary Minnaert equation (10) by reducing overcorrection when $IL(n)$ is low and by increasing image-wide homogeneity. In [35], in line with theoretical expectations, the SNLTOC equation (16) performs better than the NLTOC equation (14).

*5) C Correction Method:* In an NLTOC framework, the C correction method assumes a linear correlation between the observed terrain reflectance of each spectral band $TOARF_T(n,b)$ and illumination $IL(n) = \cos\gamma_i(n) \in [0°, 180°]$ as follows [29], [34], [35]:

$$Y(n,b) = TOARF_T(n,b) = TOARF_H(b) + C(b)IL(n) = E(b) + C(b)\cdot X(n) \quad (17)$$

where $n = 1,\ldots,N$, $b = 1,\ldots,Bnd$, and the terms $E(b) = TOARF_H(b)$, which is assumed to be constant for the entire image band $b$ in line with *Hypothesis 1*, and $C(b)$ are the regression coefficients, namely, the former is the intercept and the latter is the gradient of the regression equation $TOARF_T(n,b)$ versus $IL(n)$. Next, starting from the equations proposed in [29], the C correction method is defined as

$$TOARF_H(n,b) = TOARF_T(n,b)\cdot\left(\frac{C(b)\cos\theta_z + E(b)}{C(b)\cos\gamma_i(n) + E(b)}\right) = TOARF_T(n,b)\cdot\left(\frac{C(b)\cos\theta_z + E(b)}{C(b)IL(n) + E(b)}\right), \quad n = 1,\ldots,N;\ b = 1,\ldots,Bnd. \quad (18)$$

The SNLTOC version of the C correction equation (18) incorporates *Hypothesis 2*, defined previously, to become

$$TOARF_H(n,b|Strtm(n) = s) = TOARF_T(n,b|Strtm(n) = s) \times \left(\frac{C(b,s)\cos\theta_z + E(b,s)}{C(b,s)\cos\gamma_i(n) + E(b,s)}\right), \quad n \in \{1, N\};\ b = 1,\ldots,Bnd;\ s = 1,\ldots,S. \quad (19)$$

*Limitations:* According to [29], in an NLTOC framework, the limitations of (18) are the same as for the Minnaert equation (10) (refer to the earlier part of this paper). This conclusion is in line with [34], [35], and [41], where only small differences were observed between (10) and (18) in an NLTOC framework, although (18) is considered simpler to use.

*6) Smoothed C Correction Method:* In [29], it was observed that, in an NLTOC framework, (10), (14), and (18) cause an overcorrection of the horizontal reflectance $TOARF_H(n,b)$ where $IL(n)$ is low. Thus, in (10), (14), and (18), a reduction of the slope angle $\theta_p(n) \in [0°, 90°]$ is forced. To justify this strategy, consider that, in (10), if $\theta_p(n) \Rightarrow 0$, then $\gamma_i(n) \Rightarrow \theta_z$; thus, $\cos(\theta_z)/\cos\gamma_i(n) \Rightarrow 1$ and $TOARF_H(n,b) \Rightarrow TOARF_T(n,b)$ $\forall K(b) \in [0,1]$ and $\forall n \in \{1, N\}$. In practice, in (1), the slope angle $\theta_p \in [0°, 90°]$ is replaced by the smoothed slope angle $\bar{\theta}_p \in [0, \theta_p]$ where, according to [29]

$$\bar{\theta}_p(n) = \frac{\theta_p(n)}{Smt}, \qquad Smt = 3, 5, 7;\ n = 1,\ldots,N \quad (20)$$

where the smoothing factor $Smt \geq 1$.

In [29], the Minnaert NLTOC equation (10), the enhanced Minnaert NLTOC equation (14), the C NLTOC equation (18), and the smoothed C NLTOC equations (18) and (20) are compared on the basis of their capability of decreasing within-class variance (i.e., increasing intraclass homogeneity). On the average, the smoothed C correction method with a correction factor $Smt = 5$ gave the best performance.

*Limitations:*

1) The unrealistic *Hypothesis 1* is implicitly adopted.
2) The smoothed C NLTOC method is provided with one free parameter $Smt$ to be user defined based on heuristics.

## IV. Novel Operational Two-Stage SNLTOC System

This section is the core of the present work, where the novel two-stage operational SLTOC system is proposed. The data flow diagram (DFD) of the original operational automatic

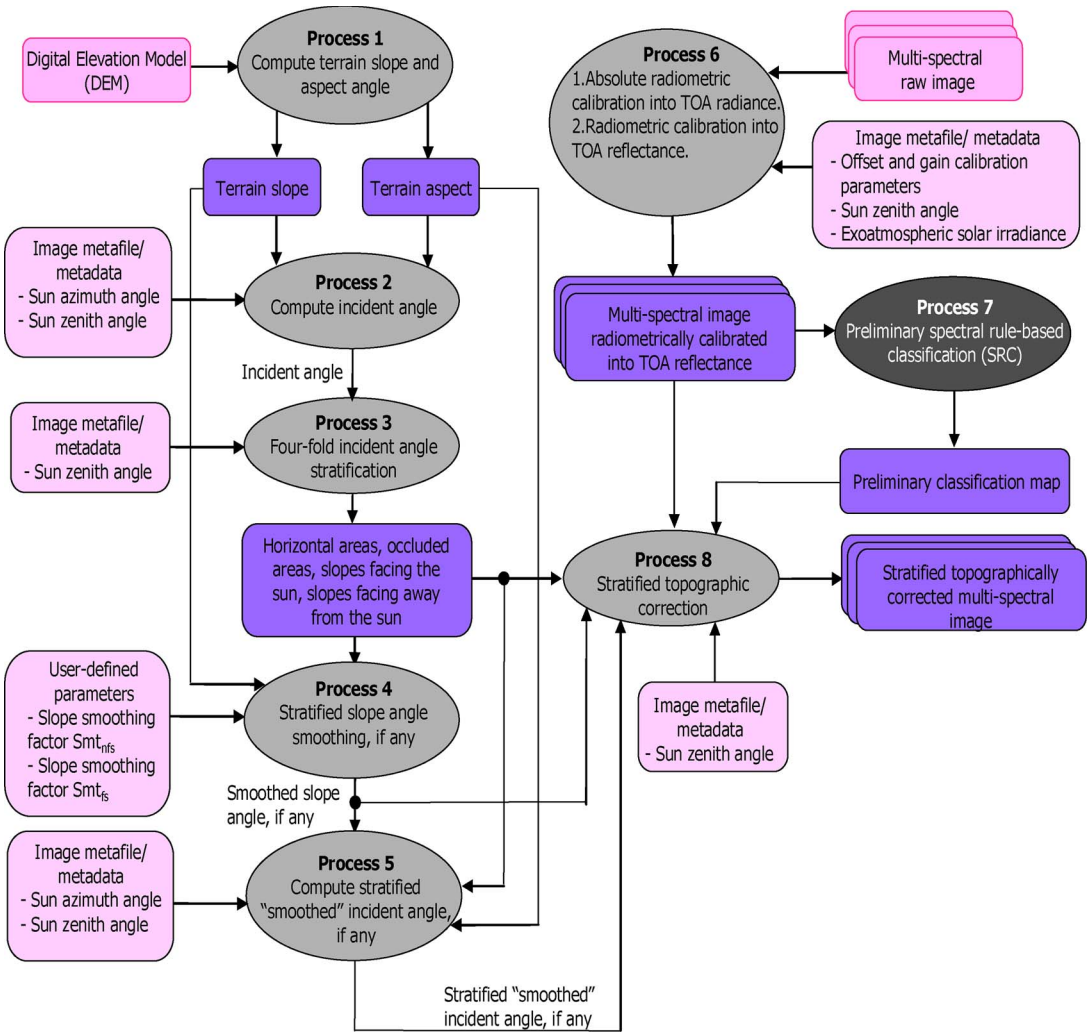


Fig. 4. DFD of the proposed operational two-stage SNLTOC system. According to [8], in a DFD, a process is shown as a bubble, a data flow is shown as an arrow, and a data store is shown as a rectangle with rounded corners.

two-stage SNLTOC approach is shown in Fig. 4 [8]. This system comprises, in cascade (also refer to Section I), the following.

1) A first-stage automatic MS image stratification. This partition maps each input pixel into a discrete and finite set of totally exhaustive and mutually exclusive strata (layers) provided with a well-understood physical and semantic meaning relevant to the provision of an operational SNLTOC solution. This stratification strategy combines the following.
   a) Four slices generated from the continuous domain of change of the subsymbolic (asemantic) pixel-based solar incident angle $\gamma_i(n) \in [0^\circ, 180^\circ]$, $n = 1, \ldots, N$, computed from a DEM and the sun's position. Refer to Processes 1–3 in Fig. 4.
   b) Symbolic (semantic) strata generated from the MS image by a fully automated SRC presented and discussed in related papers [21]–[23], [45]. Refer to Processes 6 and 7 in Fig. 4.
2) An ordinary second-stage SNLTOC method selected from among alternative approaches surveyed in Section III-B2b. Refer to Processes 4, 5, and 8 in Fig. 4.

### A. *First-Stage Automatic MS Image Stratification*

The concept of stratification is well known in statistics and system design. In statistics, stratified sampling means that "a sampling frame is divided into nonoverlapping groups or strata, e.g., equivalent to geographical areas. A sample is taken from each stratum, and when this sample is a simple random sample, it is referred to as stratified random sampling." One advantage is that "stratification will always achieve greater precision provided that the strata have been chosen so that members of the same stratum are as similar as possible with respect to the characteristic of interest." For example, in [34], an SNLTOC equation (13) performs better than the NLTOC equation (10). A possible disadvantage is that the identification of appropriate strata may be difficult [63]. Hereafter, this potential disadvantage does not hold because stratification is pursued automatically.

It is worthy to note that, in system design, the concept of stratification is adopted as a synonym of modularization, which enforces the well-known divide-and-conquer problem-solving principle. It works by recursively breaking down a problem into two or more subproblems of the same (or related) type, until these become simple enough to be solved directly [64].

Finally, it is worth mentioning that the stratified or layered approach works analogously to the focus of visual attention, which is selectively shifted in both biological vision (during so-called attentive vision [65], [66]) and artificial IUSs to detect subtle image features (namely, points and regions or, vice versa, region boundaries, i.e., edges) within a localized image area [51], [67], [68].

*1) Continuous Incident Angle Domain Slicing:* Stratification criteria employing per-pixel terrain properties, such as the pixel-based slope angle $\theta_p(n) \in [0^\circ, 90^\circ],\ n = 1, \ldots, N$, computed from a DEM irrespective of the sun's position are not a novelty in SNLTOC applications. For example, in [34] and [35], a dichotomous slope-thresholding approach is adopted, where slope values below $10^\circ$ are omitted from SNLTOC. In [39], where (15) is employed in an NLTOC framework, horizontal surfaces are masked [which is inappropriate (refer to Section III-B2a)]. In [44], ten strata based on slope ranges, but irrespective of land cover types that affect the target surface roughness (refer to Section I), are employed as input to an SNLTOC method.

In place of the pixel-based slope angle $\theta_p(n) \in [0^\circ, 90^\circ]$, $n = 1, \ldots, N$, stratification irrespective of the sun's position [34], [35], [39], [44], the per-pixel solar incident angle $\gamma_i(n) \in [0^\circ, 180^\circ]$, computed via (1) from a DEM and the sun's zenith and azimuth angles $\theta_z \in [0^\circ, 90^\circ]$ and $\phi_a \in [0^\circ, 360^\circ]$, can be mapped onto four slices, provided with a well-understood physical meaning, as a discrete function of the sun's zenith angle. These four strata $Strtm(n, \gamma_i(n) = (1), \theta_z) \in \{1, S = 4\}$ are described next.

1) ***Self-shadows [82], i.e., (shaded) pixels occluded from the sun and belonging to shadow-casting objects***, where $\gamma_i(n) \in [90^\circ, 180^\circ]$, i.e., $IL(n) \in [-1, 0],\ n \in \{1, N\}$, illuminated by indirect light exclusively (refer to Section II). This condition is acknowledged in [39, p. 3833] where it is stated that pixels featuring negative illumination (indicated erroneously as negative incident angle values, which do not exist) "will be illuminated solely by the diffuse skylight effect." These pixels must be masked in the stratum-specific selection of training samples for a two-stage SNLTOC second stage [42], which makes SNLTOC approaches more effective and more efficient (in terms of computation time). This is in line with [42], where "bad pixels are masked if their incident angles are bigger than a certain value (for example, $90^\circ$)." Two important observations follow.
   a) ***Context-sensitive determination of cast shadows***, i.e., shadows cast on the ground by objects occluding the direct sunlight, in series with the pixel-based self-shadow detection [where $\gamma_i(n) \in [90^\circ, 180^\circ]$ (see earlier part of this paper)]. For example, the prestratification approach proposed in [42] employs a context-sensitive so-called sun-ray-tracing algorithm suitable for shadow casting. Inputs of the sun-ray-tracing algorithm are a DEM and the sun's azimuth angle $\phi_a \in [0^\circ, 360^\circ]$. As output, it generates a so-called line of sight (LOS) image. Each pixel in a LOS image stores the minimum required solar elevation angle for that pixel to be unshadowed (sunlit) as a function of the given solar azimuth angle $\phi_a$ and the available DEM. Alternative real-time shadow-casting algorithms using shadow volumes extracted from an irregular mesh of vertices have been developed in computer graphics and virtual reality, e.g., refer to [69]. In general, when the sun's elevation angle decreases, shadows cast on the ground increase their length dramatically and proportional to the cotangent of the sun's elevation angle. It is worthy to note that, if a sun-ray-tracing algorithm were incorporated in our operational two-stage SNLTOC system to detect cast shadows, this sun-ray-tracing algorithm could be made more efficient ("intelligent") by providing it with an input mask consisting of pixels where $\gamma_i(n) \in [90^\circ, 180^\circ],\ n \in \{1, N\}$, i.e., occluded pixels belonging to shadow-casting objects (self shadows [82]).
   b) ***Physically based surface-reflectance model for shaded (occluded) pixels***. Shaded pixels, belonging to self-shadows, such that $\gamma_i(n) \in [90^\circ, 180^\circ],\ n \in \{1, N\}$, or cast shadows (as discussed previously), should employ a physically based surface-reflectance model specific for indirect illumination. For example, in computational geometry and terrain modeling [46], the so-called ambient occlusion is commonly used as a lighting technique to simulate a subtle indirect illumination effect accounting for multiple scattering due to nearby surfaces. In [46], ambient occlusion is computed by the OpenGL extension ARB_OCCLUSION_QUERY [70] for every point in an irregular mesh of vertices, which is the data structure commonly used in terrain modeling. This query employs, as input parameter, the resolution of the local window for the context-sensitive occlusion calculation. Since it is computationally expensive, the ambient occlusion can be precalculated once and for all for a given DEM.
2) ***Sunlit (sunny) pixels, unless occluded from the sun by one or more shadow-casting objects***, where $\gamma_i(n) \in [0^\circ, 90^\circ)$, i.e., $IL(n) \in (0, 1],\ n \in \{1, N\}$. Every pixel belonging to this layer is exposed to direct sunlight in addition to indirect light (see Section II) unless it is occluded from the sun by a shadow-casting object located in the surroundings of the pixel depending on the topography of the terrain and the sun's position. Based on per-pixel (context-insensitive) terrain properties, it is impossible to state whether an $n$th pixel featuring $\gamma_i(n) \in [0^\circ, 90^\circ)$ falls in a shadow cast by an object located near the pixel (see earlier discussion). If shaded, this pixel should be masked in an SNLTOC second stage (refer to earlier discussion). Otherwise, if a pixel featuring $\gamma_i(n) \in [0^\circ, 90^\circ)$ is not occluded from the sun by a shadow caster, then it is exposed to both direct sunlight and indirect light. Therefore, its reflectance value tends to be superior to those of pixels belonging to the same land cover type localized on slopes occluded from the sun and illuminated by indirect light exclusively where $\gamma_i(n) \in [90^\circ, 180^\circ]$.

When $\gamma_i(n) \in [0^\circ, 90^\circ)$, $n \in \{1, N\}$, this range of values can be further split into three layers featuring a physical meaning relevant to the SNLTOC problem solution as described next.

a) ***Sunlit horizontal pixels, unless occluded from the sun by one or more shadow-casting objects***, where slope angle $\theta_p(n) \approx 0$, $n \in \{1, N\}$, and thus, according to (1), $\gamma_i(n) \approx \theta_z$ (see Fig. 2). For example, in this case, (13) becomes $TOARF_H(n, b|Strtm(n)) \approx TOARF_T(n, b|Strtm(n))$ $\forall K(b, s) \in [0, 1]$, $n \in \{1, N\}$, $b = 1, \ldots, Bnd$, and $Strtm(n) \in \{1, S\}$, i.e., reflectance values in horizontal surfaces are left unchanged. Thus, sunlit pixels belonging to horizontal surfaces should be excluded from (13) to save computation time (see Section III-B2a).

b) ***Sunlit nonhorizontal pixels facing the sun, unless occluded from the sun by one or more shadow-casting objects***, where incident angle $\gamma_i(n) \in [0^\circ, \theta_z)$, $n \in \{1, N\}$. Thus, in (13), the term $\cos\theta_z / \cos\gamma_i(n) < \cos\theta_z \leq 1$ and (13) becomes $TOARF_H(n, b|Strtm(n)) < TOARF_T(n, b/Strtm(n))$. It is noteworthy that, when $\gamma_i(n) = 0$, i.e., the slope is perfectly facing the sun because conditions $[\phi_0(n) = \phi_a]$ AND $[\theta_p(n) = \theta_z]$ hold [see (2)] $\cos\theta_z / \cos\gamma_i(n) = \cos\theta_z \leq 1$. This means that, based on (13), per-stratum mean reflectance values on sunlit slopes facing the sun are expected to decrease.

c) ***Sunlit nonhorizontal pixels facing away from the sun, unless occluded from the sun by one or more shadow-casting objects***, where incident angle $\gamma_i(n) \in (\theta_z, 90^\circ)$, $n \in \{1, N\}$. Thus, in (13), the term $\cos\theta_z / \cos\gamma_i(n) > 1$ and (13) becomes $TOARF_H(n, b|Strtm(n)) > TOARF_T(n, b/Strtm(n))$. This means that, based on (13), per-stratum mean reflectance values on sunlit slopes facing away from the sun are expected to increase. In combination with the opposite behavior of (13) upon sunlit slopes facing the sun (refer to earlier comments in this paper), it means that the spectral variability (standard deviation) of a land cover class-specific stratum, computed across sunlit slopes facing the sun and facing away from the sun, where $\gamma_i(n) \in [0^\circ, \theta_z)$ OR $\gamma_i(n) \in (\theta_z, 90^\circ)$, $n \in \{1, N\}$, is expected to decrease.

To the best of our knowledge, the proposed stratification of the incident angle domain of change, i.e., $\gamma_i(n) \in [0^\circ, 180^\circ]$, $n = 1, \ldots, N$, into the four aforementioned slices is original. If so, this would be surprising if we consider the amount of work on the subject of TOC found in the literature. For example, in [31], the TOC method proposed by Civco [32] was tested on vegetation class-specific large samples falling on the slope either facing the sun or away from the sun. Unfortunately, in [31], slopes either facing the sun or away from the sun are also called sunny slopes and either shady or sun-shaded slopes, respectively, which is quite misleading according to the terminology introduced earlier in this paper (also refer to Sections II and III-B2). The same misunderstanding appears to hold in [39] where an ordinary NLTOC method is compared against a standard plug-in maximum likelihood classifier whose Gaussian basis functions are generated independently from land cover class (e.g., grass) samples belonging to sunlit and shadow areas to be merged into one output class.

To summarize, the main contribution of this section to existing knowledge on the TOC subject is to point out that, when a two-stage SNLTOC system is input with a stratified MS image radiometrically calibrated into $TOARF_T(n, b/Strtm(n))$ values, with $n = 1, \ldots, N$, $b = 1, \ldots, Bnd$, and $Strtm(n) \in \{1, S\}$, the SNLTOC linear regression second stage, comprising (13), (16), or (19) discussed in Section III-B2b, must mask out (omit) horizontal pixels together with shaded pixels belonging to self-shadows or cast shadows. This is tantamount to saying that such a two-stage SNLTOC method applies exclusively to sunlit slopes either facing the sun or facing away from the sun, in agreement with the preliminary masking strategy adopted in [42] (although that work selected occluded pixels belonging to shadow casters on the basis of DEM-driven considerations that are more empirical than those reported previously in this paper).

*2) Automatic Preliminary MS Image Classification:* It is obviously true that, in general, surface roughness changes with land cover class (as a special case, two different land cover types observed from space, for example, (calm) water and (smooth) snow, may feature the same surface roughness), although surface roughness may vary locally within class (e.g., within a deciduous forest). In addition, changes in roughness do not necessarily imply changes in spectral signature (spectral category), but changes in symbolic (semantic) spectral categories [for example, *vegetation* versus *bare soil or built-up* (refer to the latter part of this paper)] imply, in general, a change in surface roughness (as a special case, two different spectral categories observed from space, for example, *strong vegetation (SV)* and *average vegetation (AV)*, may feature a difference in surface roughness equal to zero).

To conclude, it is unquestionable that, *in primis*, land cover classes [(3-D) concepts] and, in addition, semantic spectral categories [(2-D) spectral-based semiconcepts] provide candidate areas for homogeneous surface-roughness estimation. *While land cover classes are provided with a superior semantic meaning, but are difficult to be detected automatically, spectral-based semiconcepts are provided with an inferior semantic meaning, but can be detected automatically as shown in recent works* [21]–[23], [45].

To the best of our knowledge, the integrated SRC system of systems constitutes the sole example found in existing literature of an operational fully automated classifier requiring neither user-defined parameters nor reference data samples to map onto a discrete and finite set of spectral categories an MS image, acquired across time, space, and sensors, radiometrically calibrated into $TOARF_T = (5)$ or $\rho_T = (4)$ values, the latter being an ideal case of the former when atmospheric effects are accounted for or are considered negligible (refer to Section III-A) [21]–[23], [45]. As a consequence, SRC may benefit from, but does not require, inherently ill-posed

atmospheric correction preprocessing stage. In other words, SRC considers ill-posed atmospheric correction an optional MS image preprocessing stage unlike competing classification approaches employing surface-reflectance spectra, such as the Atmospheric/Topographic correction (ATCOR3) [6], for which the solution of the ill-posed atmospheric correction problem becomes mandatory. Due to its operational properties, SRC is eligible for use as the automatic preliminary classification first stage in a two-stage stratified hierarchical RS-IUS architecture originally proposed by Shackelford and Davis [51], [68].

Starting from concepts (terms) of the terminology defined in the (3-D) world, namely, land cover classes belonging to taxonomies such as the USGS land cover taxonomy [18], the Coordination of Information on the Environment (CORINE) [71], and the International Geosphere–Biosphere Programme Discover (IGBP-DIS) [11], the rationale of SRC is to map a pixel-based vector of MS $TOARF_T$ values (see Section III-A) into a discrete and finite set of (2-D) color-based semiconcepts. *Each spectral-based semiconcept is 1) a semantic conjecture based solely on the per-pixel (noncontextual) color (spectral, i.e., chromatic and achromatic) properties and 2) equivalent to a class (concept) set* comprising either one (land cover) class or more (land cover) classes affected by spectral overlap. Thus, by definition, spectral categories are mutually exclusive in terms of spectral overlap. In particular, the SRC set of (mutually exclusive) spectral-based semiconcepts is finite and totally exhaustive, in line with the Congalton requirements [88]. This set of spectral-based semiconcepts comprises six *parent* spectral categories (supercategories, eventually split into a hierarchical tree of subcategories [45]) listed as follows according to their order of detection: *1) cloud; 2) either snow or ice; 3) either water or shadow; 4) vegetation; 5) either bare soil or built-up; and 6) outliers.*

It has been proven that the original seven-band Landsat-like SRC system (LSRC), together with its downscaled versions suitable for mapping MS imagery whose spectral resolution overlaps with, but is inferior to, the Landsat-5 Thematic Mapper (TM) and Landsat-7 Enhanced TM (ETM)+ spectral resolution, such as the four-band SPOT-like SRC (SSRC) system, are effective, efficient, and robust to changes in the input data set acquired across time, space, and sensors [21]–[23], [45]. LSRC together with its downscaled versions, such as SSRC, are identified as the integrated SRC system of systems [21], [22].

Starting from [45], where enough information is provided to the reader for the LSRC implementation to be reproduced, the SSRC system is generated by removing the excess spectral channels from the LSRC rule set, namely [21], [22]

1) (E)TM1 (B);
2) (E)TM62 [thermal IR (TIR)];
3) (E)TM7 [medium IR (MIR2)].

For the remaining spectral bands, the following equalities are enforced, where bands CH1 to CH4 identify the four SPOT-like bands monotonically increasing with wavelength:

1) (E)TM2 [Visible Green (G)] → Channel 1 (CH1);
2) (E)TM3 [Visible Red (R)] → CH2;
3) (E)TM4 [near IR (NIR)] → CH3;
4) (E)TM5 (MIR1) → CH4.

From a theoretical standpoint, the following are the expected consequences of the loss in spectral resolution affecting SSRC in comparison with LSRC.

1) Due to the loss of the TIR channel, an increase in spectral confusion (decrease in spectral separability) between light-toned (highly reflective) soil types, particularly in mountainous (and cold) areas, with classes cloud, snow, and ice, is expected.
2) It is well known that light scattering due to atmospheric conditions (haze) and aerosols is inversely proportional to the energy wavelength $\lambda$ (refer to Section III-A). Thus, the B channel is affected by scattering across all atmospheric conditions ranging from very clear to very hazy and cloudy [28]. As a consequence, due to the loss of the B channel, a decrease in the capability of detecting haze, smoke plumes, and water types is expected in SSRC. The other spectral categories detected by LSRC and, as a consequence, by its downscaled version SSRC, were designed to be scarcely affected by atmospheric scattering by taking visible bands into scant consideration [45], in line with the well-known Landsat-7 automatic cloud cover assessment (ACCA) algorithm [24]. In practice, weights of visible channels are low in the LSRC decision rules based on a convergence-of-evidence mechanism.
3) Due to the loss of the MIR2 channel, a decrease in the capability of discriminating bare soil types is expected in SSRC. For example, several burned area indexes employ MIR2 in comparison with the NIR channel [49]. However, in general, weights of the MIR2 channel are low in the LSRC decision rule set based on a convergence-of-evidence approach [45], i.e., the importance of the MIR2 channel is not relevant in LSRC.
4) An overall decrease in the number of detected spectral categories is expected due to the fact that, when adapted to the four-band SPOT-like spectral resolution, the following occur: 1) Several LSRC's spectral indexes and their fuzzy sets cannot be computed (refer to [45, Table 3]); 2) different LSRC spectral rules may coincide (refer to [45, Table 4]); 3) several LSRC spectral categories cannot be computed (refer to [45, Table 5]); and 4) different LSRC spectral categories may coincide. Overall, the number of spectral types detected by the downscaled LSRC version reduces from 46 in LSRC to 32 in SSRC, which is approximately equal to a 30% loss in comparison with LSRC [21], [22].

As will be recalled in Section VII, it is noteworthy that, starting from the "standard fine" classification map where spectral categories are equivalent to leaves in the hierarchical rule-based decision tree (respectively, 46 leaves in LSRC (refer to [45, Table 7]) and 32 leaves in SSRC, as aforementioned), LSRC (respectively, SSRC) derives two additional "standard" classification maps, featuring a medium and a coarse semantic granularity, potentially useful for different end users. The "intermediate set of spectral categories," equal to 24 (respectively, 20 for SSRC), is generated by grouping leaves of the decision tree up to their mother category, if any (for LSRC, refer to

[45, Table 7]). The "small (coarse) set of spectral categories," equal to 17 (respectively, 14 for SSRC), is obtained by an arbitrary (user-specific) semantic-driven grouping of spectral categories belonging to the "intermediate set of spectral categories." For example, as will be employed in Section VII, the SSRC "standard coarse" semantic granularity comprises the following 14 spectral categories (also refer to [45, Table 7]): 1) *vegetation*; 2) *shadow area with vegetation*; 3) *rangeland*; 4) *weak rangeland*; 5) *pit bog* (also typical of forests and vegetated agricultural fields); 6) *greenhouse* (also typical of forests and vegetated agricultural fields); 7) *barren land and built-up*; 8) *shadow area with barren land* (also typical of built-up areas, particularly asphalt roads, lava rock, etc.); 9) *water or shadow*; 10) *cloud*; 11) *thin cloud*; 12) *smoke plume*; 13) *snow*; and 14) *outliers*.

To conclude, when compared to alternative symbolic (semantic) stratification techniques adopted as the first stage in a two-stage SNLTOC approach found in literature [31], [34]–[38], [42], SRC features several advantages. Compared to one to three land cover types predetected manually or semiautomatically (refer to Section I) [31], [34]–[36], [42], SRC provides a standard fine information granularity which is 1) automatically detected and 2) much finer than the former's.

When compared to traditional parametric or nonparametric supervised classifiers such as the supervised SAM classifier revised in Section III-B1c, the spectral prior knowledge-based SRC is complementary and not at all alternative in operational terms as described in Appendix I.

When compared to well-known unsupervised (unlabeled) data-learning (e.g., clustering) algorithms adopted as the first stage of a traditional two-stage hybrid (unsupervised and supervised) data-learning classifier (such as in [37] and [38], where an ISODATA clustering algorithm is applied to a univariate NDVI image, and in [43] where an extended $k$-means unsupervised data-learning algorithm capable of automatically defining the number of clusters is applied to an MS image), SRC features several advantages highlighted in Appendix II.

### B. Second-Stage Automatic SNLTOC Method

In cascade to the two-stage SNLTOC stratification first stage (refer to Section IV-A), a second-stage SNLTOC method comprising the stratified Minnaert equation (13), the stratified enhanced Minnaert equation (16), or the stratified smoothed C equations (19) and (20), does the following: 1) Free parameter(s) of the selected SNLTOC method are estimated per input stratum $s = 1, \ldots, S$, by means of a robust linear regression technique, e.g., implemented in the Interactive Data Language (IDL), licensed by ITT Industries, Inc. [56], and 2) the trained SNLTOC method is applied per input stratum $s = 1, \ldots, S$.

To benefit from the degree of novelty of the stratification criteria proposed in Section IV-A, a stratified version of (20) is presented next, together with the pseudocode of the second-stage SNLTOC module.

*1) Stratified Smoothing Slope Criterion:* To exploit the novel stratification strategy proposed in Section IV-A, a stratified version of (20) was conceived as follows:

$$\begin{cases} \bar{\theta}_p(n|Strtm = s1) = \frac{\theta_p(n|Strtm=s1)}{Smt_{\mathrm{fs}}} \\ \bar{\theta}_p(n|Strtm = s2) = \frac{\theta_p(n|Strtm=s2)}{Smt_{\mathrm{nfs}}} \end{cases}, \qquad n \in \{1, N\} \tag{21}$$

where the stratum instantiation $s1 \in \{1, S\}$ identifies a per-class layer $c1 \in \{1, C \leq S$, refer to *Hypothesis 2* in Section III-B2b$\}$ generated by SRC (refer to Section IV-A2) and overlapping with the DEM-driven stratum of nonhorizontal pixels facing the sun (refer to Section IV-A1) while stratum $s2 \in \{1, S\}$, $s2 \neq s1$, belongs to the same per-class layer $c1 \in \{1, C\}$ and overlaps with nonhorizontal pixels facing away from the sun (refer to Section IV-A1). In (21), smoothing factors $Smt_{\mathrm{nfs}} \geq Smt_{\mathrm{fs}} \geq 1$ are user defined, e.g., based on a trial-and-error strategy. Standard values are $Smt_{\mathrm{nfs}} = 3$ and $Smt_{\mathrm{fs}} = 1$.

The advantage of (21) compared to (20) is that the former allows 1) the reduction of undesired overcorrection effects of, for example, the Minnaert SNLTOC equation (13) for low $IL(n)$ values by increasing the system parameter $Smt_{\mathrm{nfs}} \geq 1$ when incident angle $\gamma_i(n) \in (\theta_z, 90^\circ)$, i.e., in nonhorizontal slopes facing away from the sun, and, simultaneously, 2) the conservation of (not a decrease in) the desired capability of, for example, the Minnaert SNLTOC equation (13) in reducing terrain reflectance values in slopes facing the sun, i.e., when incident angle $\gamma_i(n) \in [0^\circ, \theta_z)$, by letting $Smt_{\mathrm{fs}} = 1$.

The drawback of (21) in comparison with (20) is that the former requires two system parameters to be user defined based on heuristics, whereas the latter requires only one free parameter. Moreover, the exploitation of (21) increases the computation time of the two-stage SNLTOC system (refer to Fig. 4).

*2) Pseudocode:* The two-stage SNLTOC second stage, equivalent to Process 8 in Fig. 4, is described in the pseudocode in Table I. Its advantages are as follows.

1) SNLTOC computation time is optimized by masking horizontal surfaces and occluded slopes belonging to shadow casters.
2) The preliminary classification map generated by SRC enforces the better constrained and realistic *Hypothesis 2* in place of the traditional *Hypothesis 1* (refer to Section III-B2b).
3) It combines (21) with the following: 1) the stratified Minnaert equation (13); 2) the stratified enhanced Minnaert equation (16); and 3) the stratified C correction equation (19). If $Smt_{\mathrm{nfs}} = Smt_{\mathrm{fs}} = 1$, then (21) becomes ineffective. Otherwise, $Smt_{\mathrm{nfs}} = 3$ and $Smt_{\mathrm{fs}} = 1$ by default.

## V. Study Areas, Testing Images, and Ancillary Data

The Forestry Department of Regione Veneto (FDRV), Italy, is the institution in charge of the management and protection of forests across the Veneto region in Northern Italy. Areas of activity of the FDRV are forestry planning, hydrogeological surveys, and control of forest fires.

A forest cartography of the Veneto region at scale 1 : 10 000, generated by manual photointerpretation of airborne 1-m

TABLE I
PROCESS 8 IN FIG. 4: SECOND STAGE OF THE TWO-STAGE SNLTOC SYSTEM IN PSEUDOCODE

Inputs:
- MS image radiometrically calibrated into $TOARF_T$ values, $TOARF_T(n, b)$, $n = 1, \ldots, N$, $b = 1, \ldots, Bnd$.
- Preliminary classification map, $PCM(n)$, $n = 1, \ldots, N$, with $PCM(n) \in \{1, C\}$.
- DEM-driven strata (binary masks) comprising pixels belonging to: Horizontal areas, $HA(n) \in \{0, 1\}$; Occluded slopes belonging to shadow casters, $OCS(n) \in \{0, 1\}$; Slopes facing the sun, $SFS(n) \in \{0, 1\}$; Slopes facing away from the sun, $SFAS(n) \in \{0, 1\}$, $n = 1, \ldots, N$.
- Illumination, $IL(n) \in [-1, 1]$, $n = 1, \ldots, N$.
- Surface slope image, $\theta_p(n) \in [0, 90°]$, $n = 1, \ldots, N$, if required by the selected SNLTOC method.
- Sun zenith angle $\theta_z \in [0, 90°]$.

Process 8 in Fig. 4: Stratified topographic correction algorithm.

1. FOR band $b = 1, \ldots, Bnd$, DO BEGIN
2. Compute the binary mask $MSK(n) = [HA(n)$ OR $OCS(n)]$, $n = 1, \ldots, N$.
3. Initialize $TOARF_H(n, b) = TOARF_T(n, b) * MSK(n)$, $n = 1, \ldots, N$. ;these reflectance values are left unchanged
4. ENDFOR
5. FOR each $c$-th spectral category in PCM, $c = 1, \ldots, C$, DO BEGIN
6. Compute the binary mask $MSK(n) = PCM(n \mid c)$ AND $[SFS(n)$ OR $SFAS(n)]$, $n = 1, \ldots, N$.
7. FOR band $b = 1, \ldots, Bnd$, DO BEGIN
8. Compute the masked dataset $MSKTOARF(n) = TOARF_T(n, b) * MSK(n)$, $n = 1, \ldots, N$.
9. Compute the masked dataset $MSKIL(n) = IL(n) * MSK(n)$, $n = 1, \ldots, N$.
10. Compute the dataset pair $X(n) = f_1[MSKIL(n), \theta_p(n), \theta_z]$ and $Y(n) = f_2[MSKTOARF(n), \theta_p(n)]$, $n = 1, \ldots N$, where $f_1(\cdot)$ and $f_2(\cdot)$ depend on the selected SNLTOC method, refer to Section III.B.2 above.
11. Robust linear regression for estimating parameters A and B: $Y(n) = A \cdot X(n) + B$, $n = 1, \ldots, N$.
12. Apply the SNLTOC equation $TOARF_H(n, b) = TOARF_T(n, b) * f_3[MSKTOARF(n), MSKIL(n), \theta_p(n), \theta_z, A, B]$, $n = 1, \ldots N$, where $f_3(\cdot)$ depends on the selected SNLTOC method, refer to Section III.B.2 above.
13. ENDFOR
14. ENDFOR

resolution orthophotos in true colors acquired in August–September 2000, was delivered by FDRV to end users in 2005.

In collaboration with the European Commission Joint Research Centre (EC-JRC), a comparison between airborne and spaceborne data mapping techniques and derived output products was planned and carried out in 2008.

### A. Study Area and Observation Period

A rugged and mountainous area in the vicinity of the city of Vicenza (Italy) was selected as the testing site where accurate ground surveys of forest types were conducted by FRDV from the year 2006 to the present. The geographic coordinates of the area of interest are as follows: upper left corner latitude–longitude coordinates (45.61, 11.32) and lower right corner latitude–longitude coordinates (45.14, 11.92).

To overlap with the acquisition time of available airborne imagery (see the following section), the summer season of the year 2006 was set as the target observation period.

### B. Airborne Imagery

Uncalibrated 0.5-m-resolution three-band true-color photogrammetric images of the study area were acquired by an airborne camera in September 2006.

### C. Spaceborne Imagery

According to [83], a set of RS images suitable for comparing the performance of alternative algorithms should be as follows: 1) as small as possible; 2) consistent with the aim of testing; and 3) as realistic as possible, i.e., each member of the set reflects a given type of images encountered in practice.

In the frame of the ESA Category 1 policy of free access to data in the ESA IMAGE2006 online archive at the European scale for scientific users [84], two satellite MS images of the surface area of interest acquired in the target observation period were selected for testing.

The first selected RS image is a four-band SPOT-4 high-resolution visible and infrared (HRVIR) image comprising a G, an R, a NIR, and a MIR channel and featuring 20-m spatial resolution, with an acquisition date and time equal to July 21, 2006 at 10:34:42, path 060, row 258, orthorectified by the Deutsches Zentrum für Luft- und Raumfahrt (DLR) and delivered to ESA in the framework of the GMES IMAGE2006 component and development of the European mosaic [84].

The second selected RS image is a SPOT-like four-band IRS-P6 Linear Imaging Self-Scanner (LISS)-III image comprising a G, R, NIR, and MIR channel and featuring a 23.5-m spatial resolution, with an acquisition date and time equal to June 13, 2006 at 10:15:05, orbit 13786, frame 37, orthorectified by the DLR and delivered to ESA in the framework of the GMES IMAGE2006 component and development of the European mosaic [84].

Unfortunately, in disagreement with the QA4EO guidelines delivered by the CEOS to which the aforementioned European institutions ESA, DLR, and EC belong [23], the two selected images retrieved from the ESA IMAGE2006 online archive were not provided with their original calibration metadata files. These two metafiles were incidentally recovered from the EC-JRC IMAGE2006 repository by P. Soille of the EC-JRC who radiometrically calibrated the two orthorectified images into $TOARF_T$ values (refer to Section III-A).

### D. DEM

The standard requirements of a DEM for rugged terrains are listed next.

1) A root mean square (rms) coregistration error with the MS image to be draped over the DEM should be $\leq 0.5$ pixels according to [85] and $< 1/5$ of a pixel based on change detection application requirements [86].

2) DEM spatial resolution should be $\leq (1/4) \div 1$ times the spatial resolution of the MS sensor [6].

To assess the robustness of alternative SNLTOC approaches to changes in the input data set, two DEMs were selected.

1) The well-known 90-m spatial resolution Shuttle Radar Topography Mission (SRTM). It is noteworthy that, given the two testing images described in Section VI-C, the SRTM does not satisfy the second recommendation listed previously.
2) A 25-m spatial resolution digital terrain model (DTM), georeferenced to the Italian national grid Gauss-Boaga-1, with Hayford-1924 datum. Provided by Regione Veneto, it was generated from contour lines and known altitude points acquired from cartographic maps provided by the Istituto Geografico Militare Italiano (Florence, Italy).

It is worthy to note that, in the target study area (refer to Section VI-A), the maximum height value varies around 900–1000 m, namely, 894-m height in the 25-m resolution DTM and 1061-m height in the 90-m resolution SRTM. The maximum slope is estimated at about 48°, namely, 47.76° in the DTM and 48.14° in the SRTM.

## VI. Methods

### A. Reference Data Set

This section computes the reference sample size as a function of the classification project requirements. Although well-known in the existing literature [87], [88], this issue is typically neglected by RS scientists and practitioners.

In this paper, the forest classification problem inherited from FRDV is dealt with as a one-class classification problem. In this classification case, it is well known that a classification overall accuracy (OA) probability estimate $p_{\mathrm{OA}} \in [0, 1]$ is a random variable (sample statistic) with a confidence interval $\pm\delta$ (also known as error tolerance, such that $0 < \delta < p_{\mathrm{OA}} \in [0, 1]$) associated with it, i.e., $p_{\mathrm{OA}}$ is a function of the specific reference sample set being used for its assessment. As a consequence, the reference sample size can be estimated from a given target classification accuracy and confidence interval $p_{\mathrm{OA}} \pm \delta$ [87], [88]. For example, based on the assumption that reference samples are independent and identically distributed (i.i.d.; which does not strictly hold in the case of image mapping due to spatial autocorrelation between neighboring pixels), the testing sample set size $M_{\mathrm{test}}$ needed to estimate a target $p_{\mathrm{OA}} \pm \delta$ at a desired confidence level (e.g., if confidence level $= 95\%$ then the critical value is 1.96) becomes [88]

$$M_{\mathrm{test}} = \frac{(1.96)^2 \cdot p_{\mathrm{OA}} \cdot (1 - p_{\mathrm{OA}})}{\delta^2}. \tag{22}$$

For example, if in a dichotomous (e.g., one-forest class) classification problem, where the target $p_{\mathrm{OA}} \pm \delta$ is equal to $0.85 \pm 0.05$ at a confidence level of 95%, then $M_{\mathrm{test}} = (22) \approx 196$ i.i.d. (e.g., forest) samples. Typically, ground-truth samples belong to connected regions of interest (ROIs) located across an RS image footprint. Thus, ROIs are inherently affected by autocorrelation, i.e., they violate the i.i.d. assumption; therefore, the size of these ROIs should be largely superior to the $M_{\mathrm{test}}$ value provided by (22).

In the present one-forest class project, forest ROIs were extracted from two different sources of prior semantic knowledge. As a consequence, two independent forest ground-truth sample data sets were collected, featuring different combinations of reference sample cardinality and reliability as described next.

1) ROIs extracted from a first ground-truth knowledge base of certified quality, but smaller in size, namely, 1) 0.5-m orthophotos in true colors acquired in September 2006 (refer to Section V-B) and 2) ground surveys conducted from the year 2006 to the present. This reference data set was overlapped with the two testing satellite images as follows.
   a) SPOT-4 image draped over the SRTM or DTM (refer to Section V-D). The forest-class reference data set consists of 9770 pixels, hereafter referred to as reference data set 1(a).
   b) IRS-P6 LISS-III image draped over the SRTM or DTM (refer to Section V-D). The forest-class reference data set consists of 21 999 pixels, hereafter referred to as reference data set 1(b).
2) ROIs extracted from a second ground-truth knowledge base of uncertified quality, but larger in size than the former, namely (refer to Sections I–V), forest cartography at scale 1 : 10 000 generated by FDRV from 1-m resolution orthophotos acquired in August–September 2000. This reference data set was overlapped with the available RS imagery as follows.
   a) SPOT-4 image draped over the SRTM or DTM (refer to Section VI-D). The forest-class reference data set consists of 163 393 pixels, hereafter referred to as reference data set 2(a).
   b) IRS-P6 LISS-III image draped upon the SRTM or DTM (refer to Section VI-D). The forest-class reference data set consists of 305 244 pixels, hereafter referred to as reference data set 2(b).

It is noteworthy that, to compensate for their autocorrelation superior to zero, the four aforementioned reference data sets feature a size far larger than the 200 i.i.d. samples required by (22).

### B. Image Preprocessing

As discussed in Section I, RS image preprocessing steps 1.a (linear transformation of DNs into $TOARD_T$ values) [refer to (3)] and 1.b (nonlinear transformation of $TOARD_T$ into $TOARF_T$ values) [refer to (5)] were applied to the SPOT-4 and IRS-P6 testing images described in Section V-C. Next, the two radiometrically calibrated MS input images were projected onto the European Terrestrial Reference System 1989, usually referred to as ETRS89, which is the EU-recommended frame of reference for European geodata, while the SRTM data portion of interest was projected onto a geographic (latitude/longitude) projection with the WGS84 horizontal datum and the EGM96 vertical datum. Finally, the two selected DEMs (refer to Section V-D) were resampled at the spatial resolution of the MS image at hand by cubic convolution and reprojected onto the

ETRS89 system. The four estimated rms coregistration errors were below one pixel, which was considered satisfactory based on project requirements (refer to Section V-D).

### C. Software Solutions

Several commercial RS image-processing software toolboxes can be employed for image preprocessing tasks such as image resampling, orthorectification, geographic projection, 3-D surface viewing, etc. Unfortunately, in most cases, these software toolboxes do not support RS image radiometric calibration into $TOARF_T$ values (refer to Section III-A). This observation supports the opinion that, although the problem of RS image radiometric calibration is well known in the existing literature, it is often underestimated in RS common practice (also refer to Section III-A). In our experiments, all image preprocessing operations (see Section VI-B), except the radiometric calibration of DNs into $TOARF_T$ values, were performed with the ENVI commercial software, licensed by ITT Industries, Inc. [56]. The software for the radiometric calibration of DNs into $TOARF_T$ values for the testing SPOT-4 and IRS-P6 image pair was implemented by the EC-JRC in the IDL, licensed by ITT Industries, Inc. [56].

The SSRC module, downscaled from the LSRC system described in [45], and the two-stage SNLTOC system (refer to Fig. 4), including the second-stage algorithm sketched in Table I, were implemented by the EC-JRC in the IDL programming language.

### D. SNLTOC Quality Indexes

Inherently, no evaluation measure can be injective. For example, different classification maps may produce the same confusion matrix, and different confusion matrices may generate the same confusion matrix accuracy measure (e.g., Kappa coefficient). These observations suggest that no single universally acceptable measure of accuracy should be employed in practice. Instead, a variety of uncorrelated quality indexes are required. Although in agreement with a part of existing literature [88], [89], this statement is in contrast with the high scientific impact of universal image quality indexes widely and "profitably used" by the scientific community of image and signal processing [90].

In [29], [31], and [39], several quality indexes suitable for assessing results of an NLTOC procedure are reviewed and selected. In [38], quality indexes are adopted in an SNLTOC framework. These two sets of quality criteria are discussed next.

1) Image-wide changes in pixel-based spectral patterns (spectral shapes [57], reflectance patterns [58]) before and after NLTOC should be small [29]. This statement, although vague, appears reasonable. However, in practice, it is enforced by requiring that image-wide summary statistics, namely, mean and standard deviation, should be maintained before and after NLTOC. In [31], image-wide per-class mean values must be maintained before and after NLTOC because the mean values of each land cover type on sunlit slopes facing away from the sun (identified erroneously as the shady side) should increase while those on sunlit slopes facing the sun (identified erroneously as the sunny side) should decrease.
2) For each land-cover-class-specific reference data set, the image-wide spectral standard deviation after NLTOC should decrease irrespective of the pixel-based solar incident angle [29], [31].
3) In [38], the per-class local spectral variance computed by means of a semivariogram analysis must decrease after SNLTOC.
4) A spectrally homogenous class (namely, snow) is expected to feature a radiance value constant across incident angles after SNLTOC [38].
5) In [38], the quality assessment of a land-cover-specific stratified linear regression enforced by a two-stage SNLTOC approach is twofold. First, the estimated slope of the linear regression, equivalent to the Minnaert constant, must belong to range [0, 1] and monotonically decrease with surface roughness, i.e., if the Minnaert constant equals 1, then an isotropic surface model holds (see Section III-B2b). Second, the square of the correlation between terms in the linear regression $r^2 \in [0, 1]$ monotonically increases with the capacity of the estimated Minnaert constant (slope) to characterize the class-specific relationship between topography and solar energy at the surface [37]–[39]. For example, in [38], when the enhanced Minnaert SNLTOC equation (16) is applied to the NIR band of a SPOT-3 image for classes nonvegetation, vegetation, and snow, respectively, then $r^2$ equals 0.40, 0.51, and 0.57, and the Minnaert constant equals 0.40, 0.44, and 0.48. In [39], when the enhanced Minnaert NLTOC equation (14) is applied image-wide to the three bands of a SPOT-2 image, $r^2$ ranges from 0.17 to 0.57.
6) In [39], supervised classification accuracy on a testing sample must increase after (S)NLTOC.

The quality criterion 1) listed previously (mean and standard deviation to be maintained before and after NLTOC) is maximized when image-wide spectral statistics after NLTOC are left unchanged, i.e., when no NLTOC takes place. Therefore, it does not guarantee *consistency* with the (S)NLTOC objective and is ignored hereafter.

The NLTOC quality assessment criterion 2) listed previously (image-wide spectral standard deviation after NLTOC should decrease) contradicts the first criterion and is consistent with the target of an (S)NLTOC procedure. Therefore, the first SNLTOC quality index adopted hereafter requires per-stratum spectral standard deviation to decrease after SNLTOC, where each stratum consists of slopes facing the sun and facing away from the sun within the same spectral category (refer to Section IV-A).

The quality criterion 3) listed previously (per-class radiance constant across incident angles) is difficult to apply because of the lack of per-class (e.g., snow) spectrally homogeneous slopes in spaceborne MS imagery. It is ignored hereafter.

The physical meaning of the estimated Minnaert constant within range [0, 1], if any, and the maximization of the square correlation $r^2$ in stratified linear regression, refer to the aforementioned points 4) and 5), provide the second and third SNLTOC quality criteria adopted hereafter.

In addition to the three aforementioned quality factors taken from existing literature, a fourth original (S)NLTOC quality index is conceived to assess how well the pixel-based spectral (reflectance) pattern (shape) is maintained after SNLTOC. This means that, for example, a pixel that looks like snow before (S)NLTOC must look like snow after (S)NLTOC. In practice, the within-stratum spectral mean is required to change by a similar amount (in terms of absolute or percentage quantity? This aspect remains vague to the authors of this paper.) after (S)NLTOC irrespective of band. Although stemming from the same rationale somehow expressed in point 1) previously, this implementation differs from those proposed in [29], [31], [38], and [39].

Finally, related to point 6), a fifth original (S)NLTOC quality index using semantics is adopted. It requires spectral-based semiconcepts [e.g., *vegetation* (refer to Section IV-A2)] provided as output by (S)SRC both before and after SLNTOC to be semantically consistent with land cover concepts (e.g., *forest*) provided by an independent reference data set (see Section VI-A). If this semantic consistency is proven before SNLTOC occurs, its merit is due to (S)SRC alone. If this semantic consistency holds after SNLTOC, its merit ought to be assigned to the two-stage SNLTOC system as a whole. The latter semantic consistency implicitly requires the two-stage SNLTOC system to maintain the overall shape of the pixel-based spectral signature for every pixel in the image, which is the same SNLTOC system requirement assessed by the fourth (S)NLTOC quality index selected previously.

## VII. Experimental Results

In [91] and [92], the following algorithm benchmarking criteria are proposed.

1) At least two real and standard/ appropriate data sets must be adopted to demonstrate the potential utility of an algorithm.
2) The proposed algorithm must be compared against at least one existing technique.
3) At least one-fifth of the total paper length should be devoted to evaluation.

To fulfil the aforementioned requirements, this experimental session is organized as follows.

1) The selected testing data set is two source and two resolution. It comprises a four-band 20-m-resolution SPOT-4 HRVIR image and a four-band 23.5-m resolution IRS-P6 LISS-III image (refer to Section V-C).
2) Two different DEMs, namely, a 90-m resolution SRTM and a 25-m resolution DTM are selected (refer to Section V-D). The latter is expected to guarantee enhanced SNLTOC performance.
3) To the best of our knowledge, no automatic SNLTOC system alternative to the operational automatic two-stage SNLTOC algorithm proposed in Section IV exists in RS literature. As a consequence, the latter is compared to no alternative approach. Rather, three different instantiations (A)–(C) of the proposed two-stage SNLTOC architecture are implemented and quantitatively compared by means of two different reference data sets as described next.
   a) First-stage stratification implemented according to Section IV-A. To maintain the size (cardinality) of output strata statistically significant, the selected granularity of the SSRC output map is standard coarse, featuring 14 spectral categories, i.e., $C = 14$ (refer to Section IV-A2). Thus, the total number of input image strata is (refer to *Hypothesis 2* in Section III-B2b) $S = 2$ (horizontal areas + occluded areas, to be ignored) + 14 (spectral categories) $* 2$ (slopes facing the sun + slopes facing away from the sun) $= 30$. As a consequence (refer to Table I above), the total number of linear regressions to be performed, $N_{LR}$, is equal to $C = 14$.
   b) Competing second-stage SNLTOC methods where the stratified smoothing slope (21) (refer to Section IV-B1) is combined with (refer to Section III-B2b) the following: (A) the stratified Minnaert equation (13); (B) the stratified enhanced Minnaert equation (16); and (C) the stratified C correction equation (19). If $Smt_{\mathrm{nfs}} = Smt_{\mathrm{fs}} = 1$, then the stratified smoothing slope (21) is ineffective. Otherwise, $Smt_{\mathrm{nfs}} = 3$ and $Smt_{\mathrm{fs}} = 1$ by default (refer to Section III-B2b).
   c) Two independent sets of ground-truth ROIs are employed for result validation [e.g., within-stratum variance is expected to decrease after SNLTOC (refer to Section VI-D)]. The first reference data set features inferior cardinality but superior reliability than the second data set (refer to Section V-A).

### A. Second-Stage SNLTOC Method Selection

In [29], the smoothed C NLTOC equations (18) and (20) outperform alternative NLTOC methods described in Section III-B2b. In disagreement with [29], in [35], the enhanced Minnaert NLTOC equation (14) performs better than the C NLTOC equation (18), and in line with theoretical expectations, the enhanced Minnaert SNLTOC equation (16) performs better than its nonstratified counterpart (14), when the number of predefined input strata $S = C = 2$ (forest and nonforest).

These conclusions are expected to be of scant utility in the selection of the best second-stage SNLTOC method among those surveyed in Section III-B2b in the framework of the proposed two-stage SNLTOC system whose number of input strata $S = 30 > C = 14 = N_{LR}$ (see this earlier discussion).

Table II compares quantitative results collected when the three aforementioned competing implementations (A)–(C) of the proposed two-stage SNLTOC system employ, as input, the NIR band (CH3) of the testing IRS-P6 image draped over the DTM. Table II shows that, if $Smt_{\mathrm{nfs}} = 3$ and $Smt_{\mathrm{fs}} = 1$, then implementation (C) maximizes the spectral category-specific linear regression variables $r_c^2$, $c = 1, \ldots, C = 14$ (also refer to Table I), which is somehow in line with the conclusions in [29]. However, absolute values of these square correlations

TABLE II

LAND COVER STRATIFIED REGRESSION ANALYSIS. SEMANTIC MEANING OF SPECTRAL CATEGORIES: (1) VEGETATION. (2) SHADOW AREA WITH VEGETATION. (3) RANGELAND. (4) WEAK RANGELAND. (5) PIT BOG (ALSO TYPICAL OF FORESTS AND VEGETATED AGRICULTURAL FIELDS). (6) GREENHOUSE (ALSO TYPICAL OF FORESTS AND VEGETATED AGRICULTURAL FIELDS). (7) BARREN LAND AND BUILT-UP. (8) SHADOW AREA WITH BARREN LAND (ALSO TYPICAL OF BUILT-UP AREAS, PARTICULARLY ASPHALT ROADS, LAVA ROCK, ETC.). (9) WATER OR SHADOW. (10) CLOUD. (11) THIN CLOUD. (12) SMOKE PLUME. (13) SNOW. (14) OUTLIERS (EMPTY, IN THIS CIRCUMSTANCE). (IN GRAY HIGHLIGHT) RELEVANT VALUES. (IN DARK GRAY HIGHLIGHT) MINNAERT CONSTANT VALUES WITHOUT A CLEAR PHYSICAL MEANING

| Image: IRS-P6 draped upon the DTM, Band 3 (NIR). | | Smoothed slope, $Smt_{fs}$=1, $Smt_{nfs}$=3. | | | | | | No smoothed slope, $Smt_{fs}$=1, $Smt_{nfs}$=1. | | | | | |
|---|---|---|---|---|---|---|---|---|---|---|---|---|---|
| | | Minnaert Eq. (13) | | Enhanced Minnaert Eq. (16) | | C-correction Eq. (19) | | Minnaert Eq. (13) | | Enhanced Minnaert Eq. (16) | | C-correction Eq. (19) | |
| Spectral category index | No. samples | Angular coeff. = Minnaert coeff. $\in$ [0, 1] | $r^2 \in$ [0, 1] | Angular coeff. = Minnaert coeff. $\in$ [0, 1] | $r^2 \in$ [0, 1] | Angular coeff. | $r^2 \in$ [0, 1] | Angular coeff. = Minnaert coeff. $\in$ [0, 1] | $r^2 \in$ [0, 1] | Angular coeff. = Minnaert coeff. $\in$ [0, 1] | $r^2 \in$ [0, 1] | Angular coeff. | $r^2 \in$ [0, 1] |
| Spctrl. Ct. 1 | 570131 | 0.821 | 0.142 | 0.722 | 0.100 | 70.938 | 0.142 | 0.219 | 0.093 | 0.541 | 0.913 | 23.954 | 0.111 |
| Spctrl. Ct. 2 | 90371 | 0.719 | 0.076 | 0.709 | 0.069 | 55.054 | 0.084 | 0.123 | 0.025 | 0.522 | 0.958 | 17.705 | 0.046 |
| Spctrl. Ct. 3 | 112334 | 0.574 | 0.031 | 0.643 | 0.049 | 41.929 | 0.035 | 0.055 | 0.012 | 0.514 | 0.966 | 8.808 | 0.019 |
| Spctrl. Ct. 4 | 7574 | 0.422 | 0.010 | 0.153 | 0.009 | 19.132 | 0.013 | -0.023 | 0.000 | 0.494 | 0.949 | -2.815 | 0.000 |
| Spctrl. Ct. 5 | 4088 | 0.000 | 0.001 | 0.182 | 0.007 | 0.031 | 0.001 | -0.035 | 0.000 | 0.493 | 0.960 | -3.702 | 0.003 |
| Spctrl. Ct. 6 | 3209 | 0.000 | 0.000 | 0.315 | 0.021 | 0.001 | 0.000 | 0.000 | 0.000 | 0.511 | 0.962 | -1.553 | 0.000 |
| Spctrl. Ct. 7 | 1741 | -2.117 | 0.030 | 0.189 | 0.010 | -153.693 | 0.030 | 0.055 | 0.005 | 0.507 | 0.950 | 5.634 | 0.002 |
| Spctrl. Ct. 8 | 2642 | 0.000 | 0.003 | 0.535 | 0.034 | 7.164 | 0.002 | 0.009 | 0.012 | 0.523 | 0.968 | 1.359 | 0.006 |
| Spctrl. Ct. 9 | 576 | -0.001 | 0.000 | 0.552 | 0.069 | -0.045 | 0.000 | 0.032 | 0.050 | 0.512 | 0.910 | 4.709 | 0.038 |
| Spctrl. Ct. 10 | 796 | -1.904 | 0.028 | 0.189 | 0.035 | -167.956 | 0.039 | 0.093 | 0.055 | 0.534 | 0.931 | 9.260 | 0.026 |
| Spctrl. Ct. 11 | 927 | -0.276 | 0.008 | 0.431 | 0.022 | -20.122 | 0.010 | 0.000 | 0.003 | 0.524 | 0.973 | -0.010 | 0.000 |
| Spctrl. Ct. 12 | 295 | -0.468 | 0.028 | 0.685 | 0.027 | -41.050 | 0.028 | -0.004 | 0.010 | 0.548 | 0.990 | -2.760 | 0.008 |
| Spctrl. Ct. 13 | 9 | 31.175 | 0.927 | 31.904 | 0.922 | 1414.230 | 0.921 | 15.694 | 0.806 | 13.386 | 0.807 | 643.26 | 0.804 |

are extremely low, i.e., below those ($\approx 0.5$) found in [38] where $S = 2$ (refer to Section VI-D). High values ($> 0.8$) of the spectral category-specific linear regression variables $r_c^2$, $c = 1, \ldots, C = 14$, are obtained with implementation (B) if and only if the enhanced Minnaert SNLTOC equation (16) is adopted in combination with no smoothing effect, i.e., $Smt_{\mathrm{fs}} = Smt_{\mathrm{nfs}} = 1$, which is fairly in line with the conclusions found in [35]. Additional advantages of (16) versus (19) and (21) are that the former is automatic (i.e., it requires no system parameter to be user defined) and computationally more efficient (see Fig. 4).

These conclusions were found invariant to changes in the input MS image and DEM. Thus, (16) is the only one adopted in the further testing of the proposed two-stage SNLTOC system.

### B. Two-Stage SNLTOC System Results

Three preliminary classification maps, featuring a standard fine semantic granularity comprising 32 spectral categories (see Section IV-A2), are automatically generated by SSRC from the testing SPOT (respectively, IRS) image 1) without SNLTOC, 2) with SNLTOC based on the SRTM, and 3) with SNLTOC based on the DTM [see Figs. 5–8 (respectively, Figs. 9–12 for IRS)].

Table III (respectively, Table IV for IRS) is generated from the SPOT (respectively, IRS) image to investigate the first and fourth quality indexes selected in Section VI-D, namely: 1) the within-forest class variance, measured in ground-truth ROIs, expected to decrease after SNLTOC and 2) the within-forest class mean, measured in ground-truth ROIs, whose rate of change after SNLTOC should be homogeneous (constant) across spectral bands.

Table V (respectively, Table VI) is generated from the SPOT (respectively, IRS) image to investigate the fifth quality index proposed in Section VI-D, namely, ground-truth forest ROIs should overlap with vegetation spectral categories automatically detected by SSRC.

In the following discussion of Tables III–VI, wherever necessary, land cover classes are defined according to the USGS [18], the CORINE [71], and the IGBP-DIS [11] land cover taxonomies.

*1) Spot-4 Image Data Set:* To make Tables III and V more meaningful, their quantitative results are commented in the following.

*a) Reference data set 1(a): ROIs of forest areas from orthophotos and ground surveys*

*Case 1—No TOC:* Table III provides statistics generated from the input radiometrically calibrated SPOT-4 image before

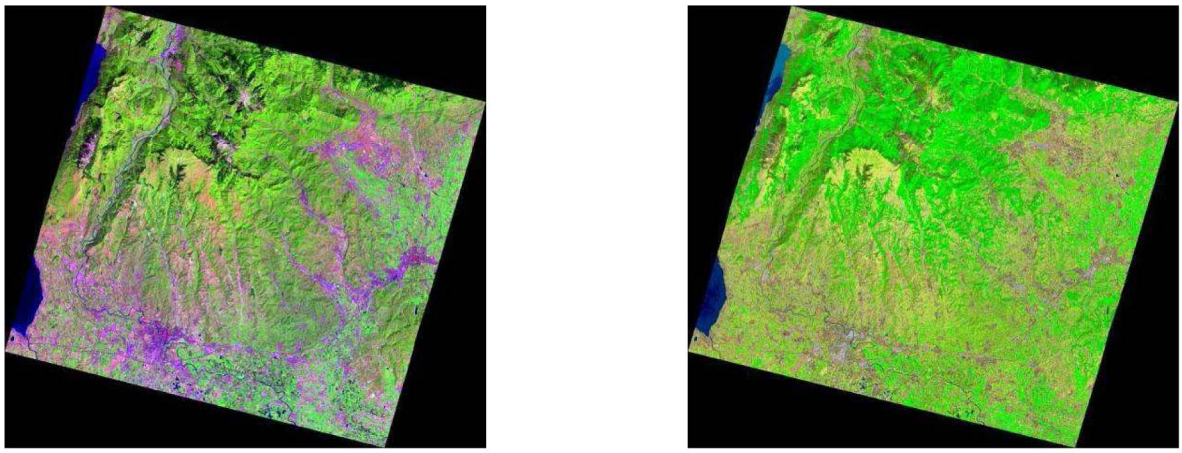

(a) (b)

Fig. 5. (a) SPOT-4 HRVIR image. Spatial resolution: 20 m. Acquisition time: July 21, 2006 at 10:34:42. Path: 060. Row: 258. Orthorectified and radiometrically calibrated into $TOARF_T$ values, shown in false colors (R: band 4, G: band 3, and B: band 1). (b) Preliminary spectral classification map, shown in pseudocolors, generated by SSRC from the SPOT-4 image shown in (a). Water and shadow areas are in blue, clouds are in white, snow and ice are in light blue, vegetation types are in different shades of green, rangeland types are in different shades of light green, and barren land types are in different shades of brown and gray.

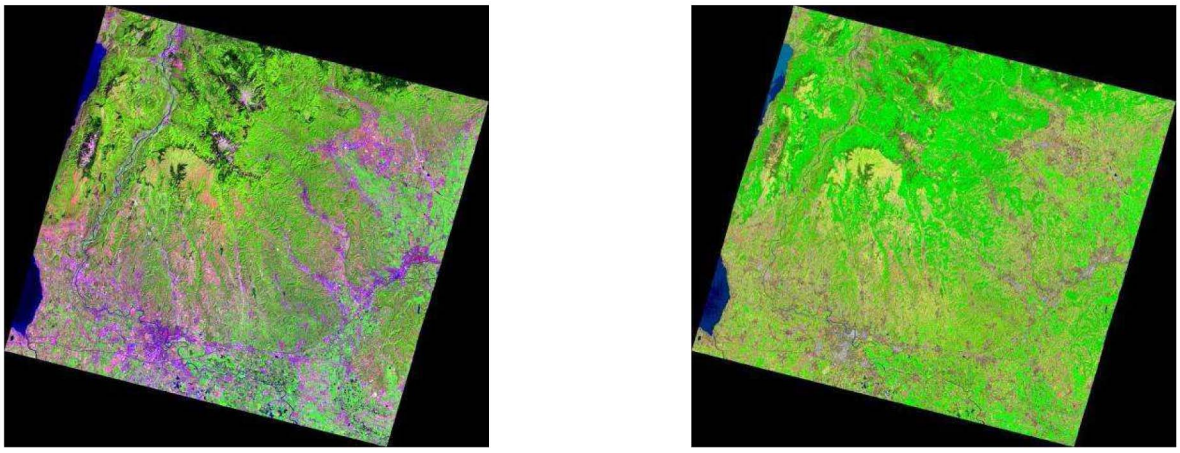

(a) (b)

Fig. 6. (a) SPOT-4 SRTM-based SNLTOC image generated from Fig. 5(a) and (b). (b) Preliminary spectral classification map, shown in pseudocolors [same as in Fig. 5(b)], generated by SSRC from the SPOT-4 image shown in (a).

(a) (b) (c)

Fig. 7. (a) Zoomed area extracted from Fig. 5(a), shown in grayscale from false colors (R: band 4, G: band 3, and B: band 1). (b) Zoomed area extracted from Fig. 6(a), shown in grayscale from false colors (R: band 4, G: band 3, and B: band 1). (c) Three-dimensional surface view of (a) draped over the SRTM.

SNLTOC takes place to be used as a reference by the SNLTOC approach with SRTM and by the SNLTOC approach with DTM.

Table V, in line with theoretical expectations, shows the following.

1) Six vegetation spectral categories feature a degree of overlap with the reference forest data set 1(a) superior to 0.5% and, overall, cover 99.62% of the forest ground truth. The acronyms of these six vegetation spectral categories [sorted according to their decreasing LAI values (see the following discussion)] are SVVHNIR, SVHNIR, SVMNIR, AVHNIR, AVMNIR, and AVLNIR.
2) Aside from few reference samples belonging to mixed pixels, no semantic inconsistency between SSRC and the reference forest data set 1(a) is found. This confirms the SSRC reliability and robustness to changes in the input data set acknowledged in related works [21]–[23], [45].

These quantitative results were validated by visual (qualitative) photointerpretation of year 2006 orthophotos (see Section V-B) where relationships between land cover classes and the six aforementioned vegetation spectral categories were identified as follows.

1) Strong Vegetation (SV) featuring Very High NIR Leaf (in the SSRC decision tree) Spectral Category (LSC) (SVVHNIR). It overlaps with very high density deciduous forests and agricultural fields.

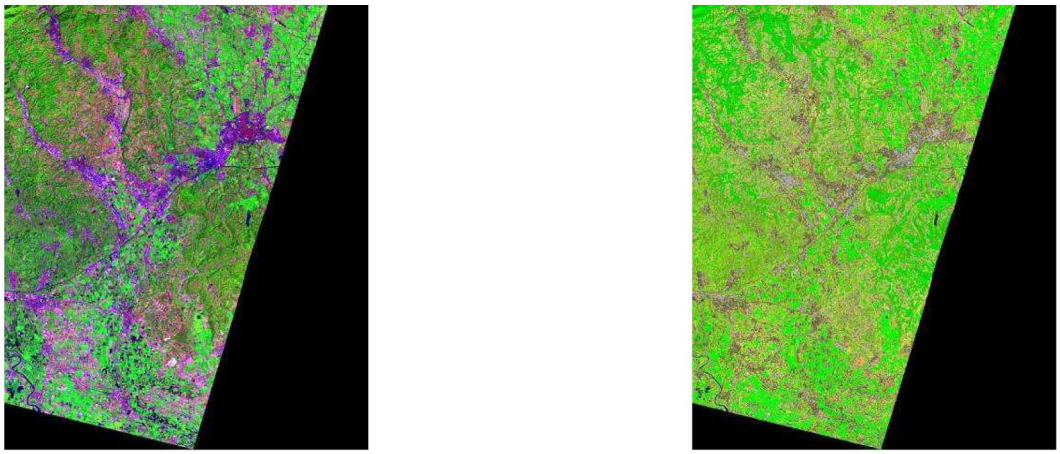

(a) (b)

Fig. 8. (a) SPOT-4 DTM-based SNLTOC image generated from Fig. 5(a) and (b). (b) Preliminary spectral classification map, shown in pseudocolors [same as in Fig. 5(b)], generated by SSRC from the SPOT-4 image shown in (a).

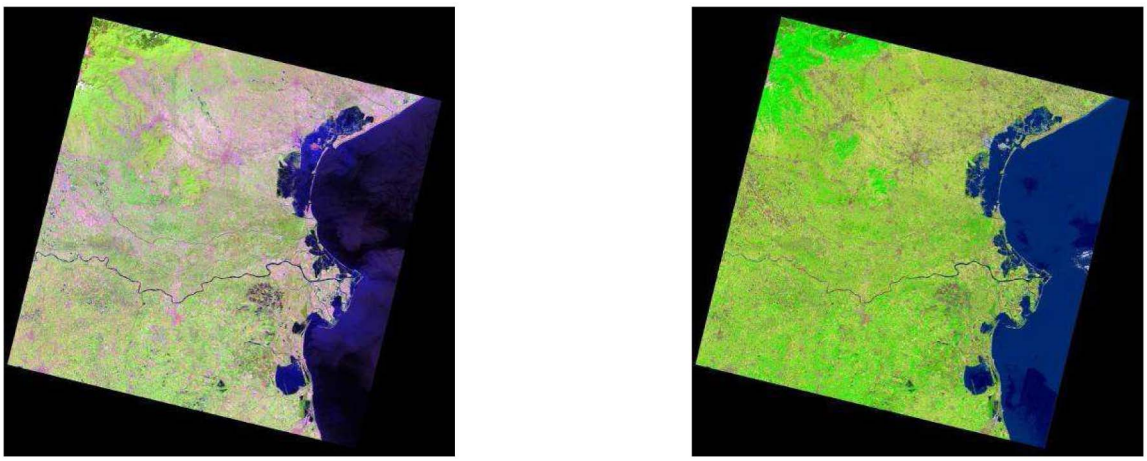

(a) (b)

Fig. 9. (a) IRS-P6 LISS-III image. Spatial resolution: 23.5 m. Acquisition time: June 13, 2006 at 10:15:05.83. Orbit: 13 786. Frame: 37. Orthorectified and radiometrically calibrated into $TOARF_T$ values, shown in false colors (R: band 4, G: band 3, and B: band 1). (b) Preliminary spectral classification map, shown in pseudocolors [same as in Fig. 5(b)], generated by SSRC from the IRS-P6 image shown in (a).

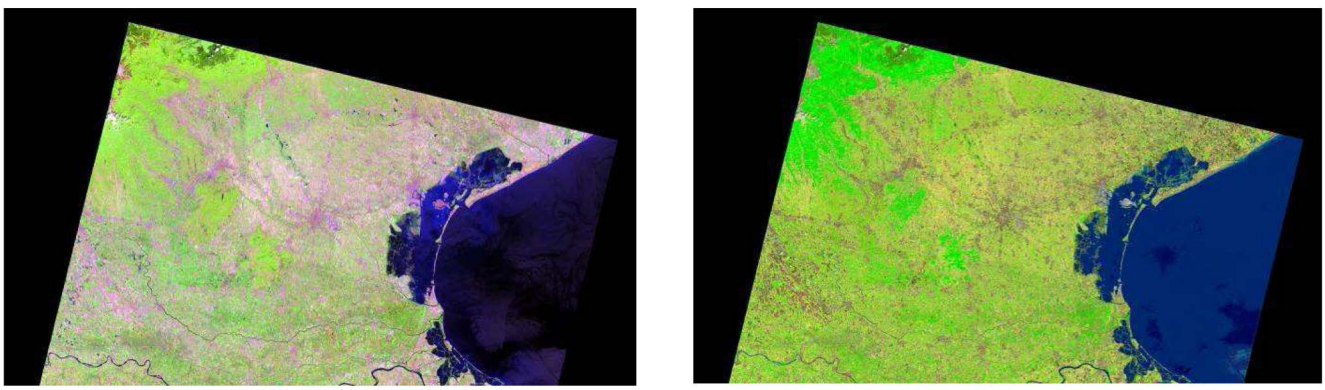

(a) (b)

Fig. 10. (a) IRS-P6 SRTM-based SNLTOC image generated from Fig. 9(a) and (b). (b) Preliminary spectral classification map, shown in pseudocolors [same as in Fig. 5(b)], generated by SSRC from the IRS-P6 image shown in (a).

2) SV with High-NIR LSC (SVHNIR). It overlaps with high-density deciduous forests, agricultural fields, and pastures (grasslands).

3) SV with Medium-NIR LSC (SVMNIR). It overlaps with high-density evergreen forests, mainly broad leaved, and high-density deciduous forests.

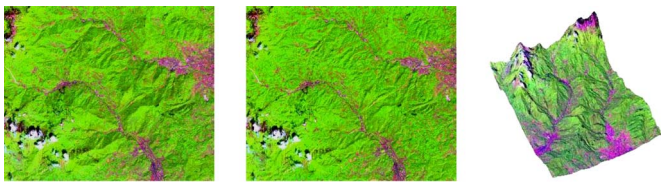

(a) (b) (c)

Fig. 11. (a) Zoomed area extracted from Fig. 9(a), shown in grayscale from false colors (R: band 4, G: band 3, and B: band 1). (b) Zoomed area extracted from Fig. 10(a), shown in grayscale from false colors (R: band 4, G: band 3, and B: band 1). (c) Three-dimensional surface view of (a) draped over the SRTM.

4) AV candidate area featuring High-NIR LSC (AVHNIR). It overlaps with deciduous forests, agricultural fields, and pastures.
5) AV candidate area featuring Medium-NIR LSC (AVMNIR). It overlaps with evergreen forests, mainly broad leaved, and deciduous forests.
6) AV candidate area featuring Low-NIR LSC (AVLNIR). It overlaps with evergreen forests, mainly needle leaved.

These relationships confirm the effectiveness of the LAI adopted by SSRC to detect, in combination with a plethora of other decision criteria, vegetation phenomena in RS imagery (refer to [45]).

*Case 2—SRTM-based SNLTOC:* Based on Table III, in line with theoretical expectations, the following are observed.

1) Within-forest class variance decreases in all spectral bands after SNLTOC.
2) The overall shape of the forest spectral signature is maintained (the mean statistic slightly increases irrespective of the spectral band) after SNLTOC.

Based on Table V, in line with theoretical expectations, the following are noticed.

1) Forest samples fall in a set of six vegetation spectral categories coincident with that of Case 1, but the overall occurrence of the most significant four spectral categories in both Cases 1 and 2, namely, spectral categories SVHNIR, SVMNIR, AVHNIR, and AVMNIR (in decreasing LAI order), is superior in Case 2 to that in Case 1. In other words, the within-forest class variance after SNLTOC is reduced with respect to the original no-TOC data set (Case 1); in fact, the same set of forest pixels is mapped onto an inferior number of vegetation color types (spectral categories).
2) No semantic inconsistency between vegetation spectral categories detected by SSRC and the reference forest data set 1(a) occurs.

*Case 3—DTM-based SNLTOC:* Based on Table III, in line with theoretical expectations, we observe the following.

1) Within-forest class variance decreases in all spectral bands after SNLTOC, and this decrease is superior to that with SRTM (Case 2) in all bands but one, in agreement with the claimed superior quality of the adopted DTM with respect to the SRTM (refer to Section V-D).
2) The overall shape of the forest spectral signature is maintained (the mean statistic slightly increases irrespective of the spectral band).

Based on Table V, in line with theoretical expectations, the following are noted.

1) Forest samples fall in a set of six vegetation spectral categories coincident with that of Cases 1 and 2, but the overall occurrence of the most significant four spectral categories in Cases 1, 2, and 3, namely, SVHNIR, SVMNIR, AVHNIR, and AVMNIR (in decreasing LAI order), is superior in Case 3 to that in Cases 1 and 2. In other words, the within-forest class variance is reduced in Case 3 with respect to Cases 1 and 2. This result accounts for the finer resolution of the DTM with respect to the SRTM, which is in line with theoretical expectations.
2) No semantic inconsistency between vegetation spectral categories detected by SSRC and the reference forest data set 1(a) occurs.

*b) Reference data set 2(a): ROIs of forest areas from cartography*

*Case 1—No TOC:* Table III provides statistics generated from the input radiometrically calibrated SPOT-4 image before SNLTOC takes place to be used as a reference by the SNLTOC approach with SRTM and by the SNLTOC approach with DTM.

Based on Table V and in comparison with results gathered with reference data set 1(a) (see Case 1 in Section VII-B1a), the following are noteworthy.

1) Six vegetation spectral categories, namely, SVVHNIR, SVHNIR, SVMNIR, AVHNIR, AVMNIR, and AVLNIR (sorted according to their decreasing LAI values), covering 99.62% of the (more reliable) reference forest data set 1(a), account for 87.38% of the (less reliable) reference forest data set 2(a). Four additional spectral categories, namely, Average Shrub Rangeland (ASR) featuring High-NIR LSC (ASRHNIR), ASR with Medium-NIR LSC (ASRMNIR), ASR with Low-NIR LSC (ASRLNIR), and Either Wetland or Dark Rangeland (WEDR) (sorted according to their decreasing LAI values), overlap with reference data set 2(a) with occurrence above 0.5%. This reveals the larger spectral dynamic of reference data set 2(a) with respect to reference data set 1(a), which accounts for the unknown accuracy of the former and its inferior reliability due to a question of temporality [the former employs forest cartography for the year 2000 as a source of reference knowledge for RS images acquired in the year 2006 (refer to Section VI-A)].
2) No semantic inconsistency between vegetation spectral categories detected by SSRC and the reference forest data set 2(a) occurs. However, spectral categories ASRHNIR, ASRMNIR, ASRLNIR, and WEDR feature medium to low LAI values; thus, they are unlikely to belong to forest land covers. This apparent inconsistency is further investigated in the following.

Based on the visual photointerpretation of year 2006 orthophotos (see Section V-B), the following relationships between spectral categories ASRHNIR, ASRMNIR, and ASRLNIR and land cover classes were identified (see Fig. 13).

1) ASRHNIR. It overlaps with agricultural land, herbaceous rangeland, or shrub and brush rangeland.

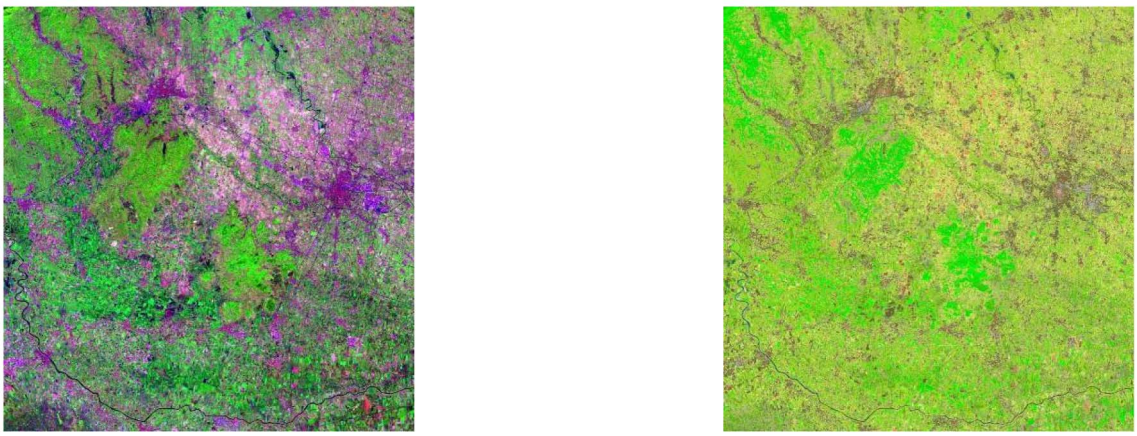

(a) (b)

Fig. 12. (a) IRS-P6 DTM-based SNLTOC image generated from Fig. 9(a) and (b). (b) Preliminary spectral classification map, shown in pseudocolors [same as in Fig. 5(b)], generated by SSRC from the IRS-P6 image shown in (a).

TABLE III
SPOT-4 INPUT IMAGE. REFLECTANCE MEAN AND STANDARD DEVIATION OF REFERENCE FOREST SAMPLES IN THE 1) RAW (NON-TOC) SPOT-4 IMAGE, 2) SRTM-BASED SNLTOC SPOT-4 IMAGE, AND 3) DTM-BASED SNLTOC SPOT-4 IMAGE. (IN GRAY HIGHLIGHT) RELEVANT VALUES

| SPOT-4 without TOC | | | | | SPOT-4 with SNLTOC (SRTM, 90 m) | | | | | | | SPOT-4 with SNLTOC (DTM, 25 m) | | | | | | |
|---|---|---|---|---|---|---|---|---|---|---|---|---|---|---|---|---|---|---|
| ROIs of forest areas from orthophotos and ground surveys | | | | | ROIs of forest areas from orthophotos and ground surveys | | | | | | | ROIs of forest areas from orthophotos and ground surveys | | | | | | |
| | Min | Max | Mean | Stdev | | Min | Max | Mean | Stdev | delta Mean | delta Stdev | | Min | Max | Mean | Stdev | delta Mean | delta Stdev |
| Band 1 | 14 | 25 | 16,83695 | 1,16203 | Band 1 | 14 | 25 | 17,225281 | 1,003482 | 2,31% | -13,64% | Band 1 | 13 | 25 | 17,133422 | 0,947963 | 1,76% | -18,42% |
| Band 2 | 9 | 20 | 11,86929 | 1,30175 | Band 2 | 9 | 19 | 12,29089 | 1,117211 | 3,55% | -14,18% | Band 2 | 9 | 25 | 12,319169 | 1,130237 | 3,79% | -13,18% |
| Band 3 | 36 | 107 | 69,71771 | 10,35046 | Band 3 | 37 | 117 | 72,727431 | 9,139176 | 4,32% | -11,70% | Band 3 | 42 | 104 | 72,530514 | 7,74306 | 4,03% | -25,19% |
| Band 4 | 21 | 60 | 37,54493 | 5,33106 | Band 4 | 25 | 59 | 39,176561 | 4,076508 | 4,35% | -23,53% | Band 4 | 25 | 56 | 39,154823 | 3,610985 | 4,29% | -32,27% |
| ROIs of forest areas from cartography | | | | | ROIs of forest areas from cartography | | | | | | | ROIs of forest areas from cartography | | | | | | |
| | Min | Max | Mean | Stdev | | Min | Max | Mean | Stdev | delta Mean | delta Stdev | | Min | Max | Mean | Stdev | delta Mean | delta Stdev |
| Band 1 | 0 | 59 | 18,31941 | 3,12484 | Band 1 | 0 | 59 | 18,476674 | 3,061647 | 0,86% | -2,02% | Band 1 | 0 | 60 | 18,218108 | 2,888812 | -0,55% | -7,55% |
| Band 2 | 0 | 80 | 14,29878 | 4,74117 | Band 2 | 0 | 80 | 14,468481 | 4,666621 | 1,19% | -1,57% | Band 2 | 0 | 83 | 14,250219 | 4,368832 | -0,34% | -7,85% |
| Band 3 | 0 | 129 | 70,30016 | 9,99967 | Band 3 | 0 | 127 | 71,428603 | 9,626825 | 1,61% | -3,73% | Band 3 | 0 | 128 | 71,218378 | 8,82919 | 1,31% | -11,71% |
| Band 4 | 0 | 110 | 40,88712 | 8,19292 | Band 4 | 0 | 114 | 41,493838 | 7,707926 | 1,48% | -5,92% | Band 4 | 0 | 111 | 41,398586 | 7,232688 | 1,25% | -11,72% |

TABLE IV
IRS-P6 LISS-III DATA SET. REFLECTANCE MEAN AND STANDARD DEVIATION OF REFERENCE FOREST SAMPLES IN THE 1) RAW (NON-TOC) IRS-P6 LISS-III IMAGE, 2) SRTM-BASED SNLTOC IRS-P6 LISS-III IMAGE, AND 3) DTM-BASED SNLTOC IRS-P6 LISS-III IMAGE. (IN GRAY HIGHLIGHT) RELEVANT VALUES

| IRS-P6 without TOC | | | | | IRS-P6 with SNLTOC (SRTM, 90 m) | | | | | | | IRS-P6 with SNLTOC (DTM, 25 m) | | | | | | |
|---|---|---|---|---|---|---|---|---|---|---|---|---|---|---|---|---|---|---|
| ROIs of forest areas from orthophotos and ground surveys | | | | | ROIs of forest areas from orthophotos and ground surveys | | | | | | | ROIs of forest areas from orthophotos and ground surveys | | | | | | |
| | Min | Max | Mean | Stdev | | Min | Max | Mean | Stdev | delta Mean | delta Stdev | | Min | Max | Mean | Stdev | delta Mean | delta Stdev |
| Band 1 | 17 | 25 | 19,87263 | 0,96665 | Band 1 | 16 | 25 | 19,90095 | 1,016796 | 0,14% | 5,19% | Band 1 | 16 | 24 | 19,88378 | 0,95932 | 0,06% | -0,76% |
| Band 2 | 10 | 19 | 13,03896 | 0,92568 | Band 2 | 9 | 19 | 13,104596 | 1,064565 | 0,50% | 15,00% | Band 2 | 9 | 18 | 13,02464 | 1,06647 | -0,11% | 15,21% |
| Band 3 | 40 | 120 | 79,61289 | 10,00546 | Band 3 | 43 | 130 | 80,077413 | 9,427419 | 0,58% | -5,78% | Band 3 | 43 | 115 | 80,64266 | 8,59413 | 1,29% | -14,11% |
| Band 4 | 24 | 53 | 40,05428 | 3,93736 | Band 4 | 25 | 54 | 40,316196 | 3,453407 | 0,65% | -12,29% | Band 4 | 29 | 50 | 40,74401 | 2,81587 | 1,72% | -28,48% |
| ROIs of forest areas from cartography | | | | | ROIs of forest areas from cartography | | | | | | | ROIs of forest areas from cartography | | | | | | |
| | Min | Max | Mean | Stdev | | Min | Max | Mean | Stdev | delta Mean | delta Stdev | | Min | Max | Mean | Stdev | delta Mean | delta Stdev |
| Band 1 | 0 | 59 | 21,28729 | 2,22458 | Band 1 | 0 | 59 | 21,192272 | 2,239942 | -0,45% | 0,69% | Band 1 | 16 | 59 | 20,999735 | 2,090001 | -1,35% | -6,05% |
| Band 2 | 0 | 87 | 14,76732 | 3,24544 | Band 2 | 0 | 84 | 14,672852 | 3,247251 | -0,64% | 0,06% | Band 2 | 9 | 83 | 14,48103 | 3,078989 | -1,94% | -5,13% |
| Band 3 | 0 | 124 | 79,73781 | 9,53583 | Band 3 | 0 | 131 | 79,351098 | 9,291704 | -0,48% | -2,56% | Band 3 | 20 | 120 | 79,28534 | 8,473831 | -0,57% | -11,14% |
| Band 4 | 0 | 129 | 43,05652 | 5,63505 | Band 4 | 0 | 129 | 42,803994 | 5,399672 | -0,59% | -4,18% | Band 4 | 14 | 129 | 42,841496 | 4,944962 | -0,50% | -12,25% |

2) ASRMNIR. It overlaps with open deciduous and mixed forests (called woody savannas in the IGBP-DIS classification scheme [11]).
3) ASRLNIR. It overlaps with permanent crops (particularly olive groves) or shrub and brush rangeland.

These relationships confirm the effectiveness of the LAI adopted by SSRC, but appear inconsistent with the existing overlap between spectral categories ASRHNIR, ASRMNIR, and ASRLNIR and the reference forest data set 2(a), as shown in Fig. 13. Since these pixels do not satisfy the forest-class

TABLE V
SPOT-4 INPUT IMAGE. SEMANTIC CONSISTENCY OF REFERENCE FOREST SAMPLES WITH PRELIMINARY SPECTRAL MAP INDEXES GENERATED BY SSRC FROM 1) RAW (NON-TOC) SPOT-4 IMAGE, 2) SRTM-BASED SNLTOC SPOT-4 IMAGE, AND 3) DTM-BASED SNLTOC SPOT-4 IMAGE. (IN GRAY HIGHLIGHT) RELEVANT VALUES

| SPOT-4 image | | | | | | | | |
|---|---|---|---|---|---|---|---|---|
| ROIs of forest areas from orthophotos and ground surveys 1(a) | | | | | | | | |
| | Raw image (non TOC) | | SNLTOC image with SRTM, 90m | | | SNLTOC image with DTM, 25m | | |
| SRC - spectr. cat. index | Ground truth forest samples | % ( > 0.5) | Ground truth forest samples | % | DELTA | Ground truth forest samples | % | DELTA |
| SVHNIR | 4078 | 41.74% | 4598 | 47.06% | 5.32% | 4867 | 49.84% | 8.10% |
| AVMNIR | 2388 | 24.44% | 2577 | 26.38% | 1.93% | 2559 | 26.20% | 1.76% |
| SVMNIR | 1471 | 15.06% | 997 | 10.20% | -4.85% | 848 | 8.68% | -6.37% |
| AVHNIR | 854 | 8.74% | 1029 | 10.53% | 1.79% | 1218 | 12.47% | 3.73% |
| AVLNIR | 764 | 7.82% | 126 | 1.29% | -6.53% | 73 | 0.75% | -7.07% |
| SVVHNIR | 178 | 1.82% | 413 | 4.23% | 2.41% | 170 | 1.74% | -0.08% |
| rest | 37 | 0.38% | 30 | 0.31% | - | 31 | 0.32% | - |
| **Total** | 9770 | 100.0% | 9770 | 100.0% | 0.00% | 9766 | 100.0% | 0.00% |
| ROIs of forest areas from cartography 2(a) | | | | | | | | |
| SVHNIR | 49132 | 30.07% | 51884 | 31.75% | 1.68% | 54903 | 33.65% | 3.59% |
| AVMNIR | 39851 | 24.39% | 41381 | 25.33% | 0.94% | 40730 | 24.97% | 0.58% |
| AVHNIR | 29163 | 17.85% | 30016 | 18.37% | 0.52% | 31856 | 19.53% | 1.68% |
| ASRMNIR | 12835 | 7.86% | 13150 | 8.05% | 0.19% | 13161 | 8.07% | 0.21% |
| SVMNIR | 12190 | 7.46% | 9819 | 6.01% | -1.45% | 10293 | 6.31% | -1.15% |
| AVLNIR | 6715 | 4.11% | 2577 | 1.58% | -2.53% | 1689 | 1.04% | -3.07% |
| ASRHNIR | 5534 | 3.39% | 5269 | 3.22% | -0.16% | 4995 | 3.06% | -0.33% |
| SVVHNIR | 3809 | 2.33% | 5037 | 3.08% | 0.75% | 2482 | 1.52% | -0.81% |
| WEDR | 1158 | 0.71% | 1158 | 0.71% | 0.00% | 923 | 0.57% | -0.14% |
| ASRLNIR | 1085 | 0.66% | 1014 | 0.62% | -0.04% | 788 | 0.48% | -0.18% |
| rest | 1921 | 1.17% | 2088 | 1.28% | - | 1315 | 0.80% | - |
| **Total** | 163393 | 100.0% | 163393 | 100.0% | | 163135 | 100.0% | |

definition adopted by, for example, the IGBP-DIS classification scheme, which considers, as forest lands, those dominated by woody vegetation with a percent cover $> 60\%$ and height exceeding 2 m, they were rejected by the reference forest data set 2(a).

To summarize, as already outlined in [21], [22], and [45], due to its effectiveness and reliability, (S)SRC can be adopted as a source of semantic information, which is automatically generated from RS imagery and capable of improving the (often unknown) quality of any available ground-truth data set (e.g., CORINE).

*Case 2—SRTM-based SNLTOC:* Based on Table III, in line with theoretical expectations, we note the following.

1) Within-forest class variance decreases in all spectral bands after SNLTOC, and this decrease is inferior to that with the more reliable reference data set 1(a).
2) The overall shape of the forest spectral signature is maintained (the mean statistic slightly increases irrespective of the spectral band).

Based on Table V, in line with theoretical expectations, the following observations are noted.

1) Forest samples fall in a set of ten spectral categories coincident with that of Case 1, but the overall occurrence of the most significant four spectral categories in both Cases 1 and 2, namely, spectral categories SVHNIR, AVHNIR, AVMNIR, and ASRMNIR (sorted according to their decreasing LAI value), is superior in Case 2 to that in Case 1. In other words, the within-forest class variance is reduced with respect to the original no-TOC data set (Case 1).
2) As in Case 1, based on the photointerpretation of year 2006 orthophotos, the reference forest samples overlapping with spectral categories ASRHNIR, ASRMNIR, and ASRLNIR were considered incorrect and rejected from the forest ground truth 2(a).
3) No semantic inconsistency between the vegetation spectral categories detected by SSRC and the (revised) reference forest data set 2(a) occurs.

*Case 3—DTM-based SNLTOC:* Based on Table III, in line with theoretical expectations, the following are noteworthy.

1) Within-forest class variance decreases in all spectral bands after SNLTOC. This decrease is superior to that with SRTM (Case 2) and inferior to that assessed with the more reliable reference data set 1(a).
2) The overall shape of the forest spectral signature is maintained (although the mean statistic slightly decreases in

TABLE VI
IRS-P6 LISS-III DATA SET. SEMANTIC CONSISTENCY OF REFERENCE FOREST SAMPLES WITH PRELIMINARY SPECTRAL MAP INDEXES GENERATED BY SSRC FROM THE 1) RAW (NON-TOC) IRS-P6 LISS-III IMAGE, 2) SRTM-BASED SNLTOC IRS-P6 LISS-III IMAGE, AND 3) DTM-BASED SNLTOC IRS-P6 LISS-III IMAGE. (IN GRAY HIGHLIGHT) RELEVANT VALUES

| IRS-P6 image | | | | | | | | |
|---|---|---|---|---|---|---|---|---|
| ROIs of forest areas from orthophotos and ground surveys 1(b) | | | | | | | | |
| | Raw image (non TOC) | | SNLTOC image with SRTM, 90m | | | SNLTOC image with DTM, 25m | | |
| SRC - spectr. cat. index | Ground truth forest samples | % ( > 0.5) | Ground truth forest samples | % | DELTA | Ground truth forest samples | % | DELTA |
| SVHNIR | 11272 | 51.24% | 11536 | 52.44% | 1.20% | 12312 | 55.98% | 4.74% |
| AVHNIR | 4094 | 18.61% | 4598 | 20.90% | 2.29% | 4664 | 21.21% | 2.60% |
| SVVHNIR | 3391 | 15.41% | 3372 | 15.33% | -0.09% | 3304 | 15.02% | -0.39% |
| AVMNIR | 2718 | 12.36% | 2125 | 9.66% | -2.70% | 1469 | 6.68% | -5.68% |
| SVMNIR | 309 | 1.40% | 216 | 0.98% | -0.42% | 125 | 0.57% | -0.84% |
| AVLNIR | 133 | 0.60% | 60 | 0.27% | -0.33% | 30 | 0.14% | -0.47% |
| rest | 82 | 0.37% | 92 | 0.42% | - | 89 | 0.40% | - |
| **Total** | 21999 | 100.0% | 21999 | 100.0% | | 21993 | 100.0% | |
| ROIs of forest areas from cartography 2(b) | | | | | | | | |
| AVHNIR | 108851 | 35.65% | 108520 | 35.55% | -0.11% | 110157 | 36.08% | 0.43% |
| SVHNIR | 106353 | 34.84% | 111082 | 36.38% | 1.55% | 123068 | 40.31% | 5.47% |
| SVVHNIR | 41403 | 13.56% | 38255 | 12.53% | -1.03% | 32050 | 10.50% | -3.06% |
| AVMNIR | 26797 | 8.78% | 25946 | 8.50% | -0.28% | 21324 | 6.98% | -1.79% |
| ASRHNIR | 8372 | 2.74% | 7655 | 2.51% | -0.23% | 7179 | 2.35% | -0.39% |
| ASRMNIR | 6850 | 2.24% | 7593 | 2.49% | 0.24% | 7239 | 2.37% | 0.13% |
| SVMNIR | 1949 | 0.64% | 1587 | 0.52% | -0.12% | 805 | 0.26% | -0.37% |
| rest | 4726 | 1.54% | 4663 | 1.52% | - | 3502 | 1.14% | - |
| **Total** | 305301 | 100.0% | 305301 | 100.0% | | 305324 | 100.0% | |

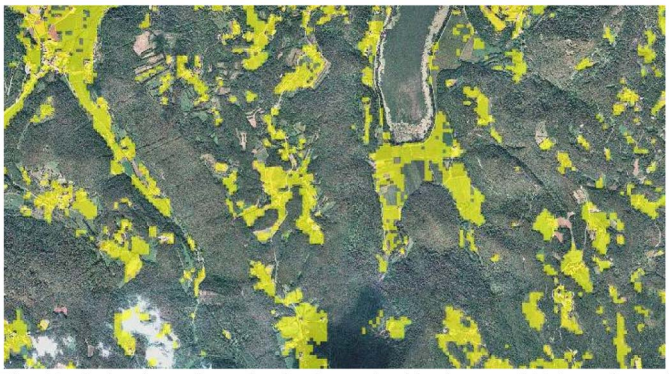

Fig. 13. (In real colors) Orthophoto acquired in the year 2006 overlapped with (in yellow) spectral categories ASRHNIR, ASRMNIR, and ASRLNIR of the SSRC map generated from the SRTM-based SNLTOC SPOT-4 image. These two spectral categories clearly overlap with agricultural fields, pastures, and other types of nonforest land.

two out of four spectral bands and slightly increases in the remaining two bands).

Based on Table V, in line with theoretical expectations, we notice the following.

1) Forest samples fall in a set of ten spectral categories coincident with that of Cases 1 and 2, but the overall occurrence of the most significant four spectral categories in Cases 1, 2, and 3, namely, SVHNIR, AVHNIR, AVMNIR, and ASRMNIR (sorted according to their decreasing LAI value), is superior in Case 3 to that in Cases 1 and 2. In other words, the within-forest class variance is reduced in Case 3 with respect to Cases 1 and 2. This should account for the finer resolution of DTM with respect to SRTM.
2) As in Case 1, based on the photointerpretation of year 2006 orthophotos, the reference forest samples overlapping with spectral categories ASRHNIR, ASRMNIR, and ASRLNIR were considered incorrect and rejected from the forest ground truth 2(a).
3) No semantic inconsistency between vegetation spectral categories detected by SSRC and the (revised) reference forest data set 2(a) occurs.

*2) IRS-P6 Image Data Set:* To make Tables IV and VI more meaningful, their quantitative results are commented next.

*a) Reference data set 1(b): ROIs of forest areas from orthophotos and ground surveys*

*Case 1—No TOC:* Table IV provides statistics generated from the input radiometrically calibrated IRS-P6 image before SNLTOC takes place to be used as a reference by the SNLTOC approach with SRTM and by the SNLTOC approach with DTM.

Based on Table VI, in line with theoretical expectations, the following are observed.

1) Six vegetation spectral categories, namely, SVVHNIR, SVHNIR, SVMNIR, AVHNIR, AVMNIR, and AVLNIR (sorted according to their decreasing LAI values), feature a degree of overlap with the reference forest data set 1(b) superior to 0.5% and, overall, cover 99.63% of the forest ground truth. These spectral types are in common with the SPOT-4 image Case 1 (refer to Section VII-B1a).
2) No semantic inconsistency between vegetation spectral categories detected by SSRC and the reference forest data set occurs, which confirms the SSRC reliability and robustness to changes in the input data set, in line with [45].

*Case 2—SRTM-based SNLTOC:* Based on Table IV, in partial agreement with theoretical expectations, the following are noticed.

1) Within-forest class variance decreases in only two of four spectral bands after SNLTOC.
2) The overall shape of the forest spectral signature is maintained (the mean statistic slightly increases irrespective of the spectral band).

Based on Table VI, observations analogous to those driven from reference data set 1(a) in the SRTM-based SNLTOC SPOT-4 image Case 2 reported in Section VII-B1a hold here.

*Case 3—DTM-based SNLTOC:* Based on Table IV, in partial agreement with theoretical expectations, we note the following.

1) Within-forest class variance decreases in only three out of four spectral bands after SNLTOC, and this decrease is superior to that with SRTM.
2) The overall shape of the forest spectral signature is maintained after SNLTOC (although the mean statistic slightly increases in three out of four spectral bands and slightly decreases in the fourth spectral band).

Based on Table VI, observations analogous to those driven by reference data set 1(a) in the DTM-based SNLTOC SPOT-4 image Case 3 reported in Section VII-B1a hold here.

*b) Reference data set 2(b): ROIs of forest areas from cartography*

*Case 1—No TOC:* Table IV provides statistics generated from the input radiometrically calibrated IRS-P6 image before SNLTOC takes place to be used as a reference by the SNLTOC approach with SRTM and by the SNLTOC approach with DTM.

Based on Table VI, observations analogous to those driven by reference data set 2(a) in the no-TOC SPOT-4 image Case 1 reported in Section VII-B1b hold here.

*Case 2—SRTM-based SNLTOC:* Based on Table IV, in partial agreement with theoretical expectations, we notice the following.

1) Within-forest class variance decreases in two out of four spectral bands, and this decrease is inferior to that with the more reliable reference data set 1(b).
2) The overall shape of the forest spectral signature is maintained (the mean statistic slightly decreases irrespective of the spectral band).

Based on Table VI, we observe the following, in agreement with theoretical expectations.

1) Forest samples fall in a set of spectral categories coincident with that of Case 1. After SNLTOC, the spectral category SVHNIR gains occurrence although the overall occurrence of the most significant four spectral categories in both Cases 1 and 2, namely, SVVHNIR, SVHNIR, AVHNIR, and AVMNIR (sorted according to their decreasing LAI value), remains unchanged. This means that the spectral spread of class forest is reduced after SNLTOC.
2) No semantic inconsistency between vegetation spectral categories detected by SSRC and the reference forest data set 2(b) occurs.

*Case 3—DTM-based SNLTOC:* Based on Table IV, in partial agreement with theoretical expectations, the following are noted.

1) Within-forest class variance decreases in all spectral bands after SNLTOC. This decrease is superior to that with SRTM (Case 2), but it is not always inferior to that with the more reliable reference data set 1(b).
2) The overall shape of the forest spectral signature is maintained (the mean statistic slightly decreases irrespective of the spectral band).

Based on Table VI, we observe the following, in agreement with theoretical expectations.

1) After SNLTOC, the spectral category SVHNIR gains occurrence although the overall occurrence of the most significant four spectral categories in Cases 1, 2, and 3, namely, SVVHNIR, SVHNIR, AVHNIR, and AVMNIR (sorted according to their decreasing LAI value), remains unchanged. This means that the spectral spread of class forest is reduced in Case 3 with respect to Cases 1 and 2.
2) No semantic inconsistency between vegetation spectral categories detected by SSRC and the reference forest data set 2(b) occurs.

*3) Discussion of Results:* The quantitative SNLTOC results shown in Tables III–VI require the availability of an independent reference (ground truth, e.g., *forest*) data set. Absolute values of quality indexes generated from Tables III–VI are not significant. Rather, their relative values are important for comparing alternative SNLTOC solutions. Overall, the agreement of these relative values with theoretical expectations is impressive. Tables III–VI prove the following. First, the proposed automatic two-stage SNLTOC system is effective in reducing the within-(forest) class variance while no significant distortion in pixel-based spectral signatures is introduced. This effectiveness decreases monotonically with the spatial resolution of the DEM (i.e., effectiveness increases as the spatial resolution of the DEM becomes finer). Second, the first-stage automatic SSRC module is effective and robust to changes in the input data set; thus, it can be adopted as the core of an automatic two-stage SNLTOC system.

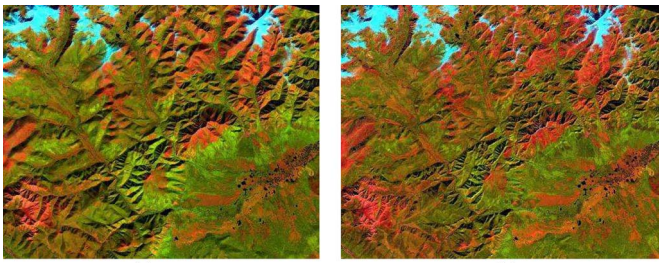

(a) (b)

Fig. 14. (a) Landsat 7 ETM+ image of Siberia (path: 033, row: 033, acquisition date: September 14, 2000), shown in false colors (R: band ETM5, G: band ETM4, and B: band ETM1), with 30-m resolution and calibrated into TOA reflectance. (b) Two-stage SNLTOC of (a), based on the SRTM. (Top right in the image) Maximum mountain height: 2230 m. (Bottom right in the image) Flat height: 460 m.

(a) (b) (c)

Fig. 15. (a) Forest/nonforest binary classification map generated from the IRS-P6 LISS-III image shown in Fig. 9(a) by SAM implemented in ENVI. Maximum angle threshold (in radians) $= 0.1$. Forest sample data set cardinality $= 21\,999$. Overall accuracy $(\mathrm{OA}) = 20\,820/21\,999 = 94.64\%$. (b) Example of combination of the forest map generated by SAM, shown in (a), with the mutually exclusive and totally exhaustive classification map, automatically generated by SSRC, shown in Fig. 9(b). The land cover class forest shown in (a) is shown in a bright green pseudocolor. (c) Continuous intelligent SVI: Second-derivative greenness index computed by SSRC from Fig. 9(a) masked by a binary vegetation mask extracted from the SSRC map shown in Fig. 9(b).

### C. Qualitative SNLTOC Results in a High Mountainous Site

The capability of the proposed automatic two-stage SNLTOC system to deal with RS images of high-altitude regions (featuring elevation, for example, $>$ 1500 m), with sparse vegetation and bare soil, where rock and snow cover dominate the landscape, is investigated qualitatively (since no independent ground-truth data set is available, which is often the case in RS image mapping problems) in a Landsat 7 ETM+ image of Siberia (path: 033, row: 033, acquisition date: 2000-14-09) calibrated into $TOARF_T$ values (see Section III-A). In this test site, according to the available 90-m-resolution SRTM, the maximum mountainous height is 2230 m with a flat terrain height of 460 m.

To deal with Landsat imagery, the proposed two-stage SNLTOC system adopts, as its preliminary classification first stage, the automatic LSRC module (refer to Section IV-A2) in place of the SSRC system adopted in Section VII-B. The LSRC standard coarse output map features 17 spectral categories, i.e., $C = 17$ (refer to Section IV-A2); thus, the total number of input image strata is $S = 2$ (horizontal areas + occluded areas) + 17 (spectral categories) $*$ 2 (slopes facing the sun + slopes facing away from the sun) $= 36$, thus $N_{LR} = C = 17$ (also refer to Section VII).

The radiometrically calibrated input image and the SNLTOC output image can be visually compared in Fig. 14(a) and (b). A visual assessment of these two images shows that the SNLTOC transformation provides an effective compensation for changes in the solar incident angle. This qualitative conclusion is confirmed by experimental evidence. Several ROIs belonging to classes bare soil, rangeland, woodland, and snow are identified across Fig. 14(a) by an expert photointerpreter. These ROIs overlap with slopes facing the sun and facing away from the sun according to the given DEM (refer to Section IV-A1). Spectral variance is diminished after SNLTOC in all selected ROIs. The overall shape of spectral signatures generated from the selected ROIs is well preserved after SNLTOC, which means that, in practice, a pixel belonging to a given class, for example, snow, looks like snow after SNLTOC [refer to Fig. 14(a) and (b)]. Finally, small but genuine image details appear well preserved after SNLTOC (although some artifacts are introduced due to the presence of spurious pits in the DEM). This merit is due to LSRC whose semantic partition of the Landsat image is pixel based (therefore intrinsically able to detect small but genuine image details), but effective and reliable, namely, unaffected by the typical salt-and-pepper classification noise effect characterizing ordinary pixel-based classifiers (such as maximum likelihood, neural networks, etc.) [72].

To conclude, this experiment shows that, in a high-altitude region (featuring maximum mountainous height equal to 2230 m with a flat terrain height of 460 m), the following are true: 1) The proposed automatic two-stage SNLTOC system is effective in reducing within-class variance while no significant distortion in pixel-based spectral signatures is introduced, and 2) the automatic LSRC module is effective and eligible for adoption as the core of an automatic two-stage SNLTOC system.

### D. Supervised Classification in Series With SNLTOC

In [21]–[23], and [45], it was clearly stated that an operational automatic SRC system is preliminary and not at all alternative to traditional algorithms capable of learning from either unlabeled (unsupervised) or labeled (supervised) data.

To highlight this fundamental concept in an operational framework, this section compares output products generated from the testing IRS-P6 satellite image draped over the DTM (refer to Section VII-B8) by the following: 1) SSRC (refer to Section IV-A2); 2) a two-stage SNLTOC system incorporating SSRC (refer to Section IV); and 3) a standard supervised data-learning classifier, for example, SAM (refer to Section III-B1c), which is well known for its relative insensitiveness to illumination and albedo effects [57], [58] (for a theoretical comparison between SAM and SRC, refer to Appendix I).

The reliable ground-truth knowledge base represented by the reference data set 1(b), consisting of 21 999 ground-truth forest samples distributed across the IRS-P6 satellite image (refer to Section VI-A), was selected for quantitative SNLTOC quality assessment (refer to Section VI-D).

In RS common practice, the forest-class reference data set 1(b) can be employed by SAM to solve a dichotomous (one-class) forest–nonforest classification problem. For example, Fig. 15(a) shows the binary forest map generated by SAM,

implemented in the ENVI software toolbox with a maximum angle threshold in radians equal to 0.1 (for outlier detection), from the IRS-P6 image shown in Fig. 9(a). In this one-class classification problem, computation time is equivalent to a few seconds with an OA probability $p_{\mathrm{OA}} \pm \delta = (20\,820/21\,999 = 94.64\%) \pm (22) = 0.0\%$.

Let us consider an alternative RS application scenario where, in addition (and not as an alternative) to SAM, an operational automatic two-stage SNLTOC system incorporating SSRC in its first stage (refer to Section IV) is made available to end users together with the DTM of the input IRS-P6 image. In this innovative operational frame, the same (identical) ground-truth forest data set 1(b) employed previously to generate Fig. 15(a) can be profitably exploited as follows.

1) A preliminary spectral map can be automatically generated by SSRC from Fig. 9(a) in a few minutes of computation time ($<$ 5 min when SSRC is implemented in the C programming language) on a desktop computer provided with a Dual Core Pentium processor [21]–[23]. As shown in Fig. 9(b), this output product, *per se*, can be employed to refine the semantic quality of the available ground-truth forest data set 1(b) (analogously to the ground-truth sample refinement conducted in Section VII-B8).
2) An automatic two-stage SNLTOC system can generate a topographically normalized MS image, shown in Fig. 12(a), from the input DTM, the preliminary SSRC map shown in Fig. 9(b), and the IRS-P6 image shown in Fig. 9(a) in a few minutes of computation time ($<$ 10 min when SNLTOC is implemented in the IDL programming language).
3) If useful, the SNLTOC image shown in Fig. 12(a) can be automatically reclassified by SSRC, e.g., see Fig. 12(b).
4) At this stage, the supervised information represented by the ground-truth forest data set 1(b) can come into play. The same (identical) SAM implementation exploiting the same (identical) ground-truth forest data set 1(b) previously adopted to generate Fig. 15(a) can now be employed to map the SNLTOC image shown in Fig. 12(a). The binary classification map generated by SAM from the SNLTOC image shown in Fig. 12(a) features $p_{\mathrm{OA}} \pm \delta = (21\,011/21\,999 = 95.51\%) \pm (22) = 0.0\%$. This value is (slightly) superior to the $p_{\mathrm{OA}} \pm \delta$ value $= (20\,820/21\,999 = 94.64\%) \pm 0.0\%$ estimated in Fig. 15(a), as mentioned earlier in this paper. This is one more evidence of the expected benefits of MS image topographic normalization before classification acknowledged in existing literature, e.g., classification $p_{\mathrm{OA}}$ values improved around 4%, namely, from 79% to 83%, in [34] and around 6%, namely, from 82% to 88%, in [36] after NLTOC and SNLTOC (also refer to Section VI-D).
5) Aside from improving the classification map generated by SAM in series with SNLTOC, the mutually exclusive and totally exhaustive classification map generated by SSRC at no cost (in terms of user supervision for parameter selection and collection of ground-truth samples), shown in Fig. 9(b), can be employed to replace pixels unclassified by SAM in Fig. 15(a), as shown in Fig. 15(b). In other words, Fig. 15(b) can replace Fig. 15(a) at no additional cost.

In operational terms, another important difference between SAM and (S)SRC is that, unlike the former, the latter generates several value-added products suitable for RS applications different from classification, including estimation of either canopy biophysical structure variables (e.g., LAI) or canopy biochemical properties (e.g., FAPAR) from a continuous spectral VI (SVI) [60]. Any traditional SVI, such as the well-known NDVI [19], is computed as an algebraic combination of pixel components from different wavelength bands to produce a scalar value. An SVI should be very sensitive to target vegetation factors (such as vegetation structure and the state of vegetation cover in terms of leaf water content, leaf chlorophyll content, age, mineral deficiencies, etc.) while being insensitive to other factors affecting spectral reflectance such as soil (background) properties in addition to solar/viewing geometry and atmospheric conditions [19]. In the case of (S)SRC, an intelligent SVI generated from Fig. 9(a) is shown in Fig. 15(c). It consists of a novel second-derivative greenness index, which is proposed in [21], [22] masked by a binary vegetation mask extracted from the preliminary (S)SRC map shown in Fig. 9(b). As a result, the intelligent SVI responds zero to nonvegetation surface types, which is not the case of any traditional SVI.

## VIII. Summary and Conclusion

The near-real-time availability of a preliminary spectral classification map automatically generated from MS imagery by SRC paves the way to the design and implementation of operational automatic RS-IUSs as potential components of operational GEOSS and GMES instantiations.

In this paper, the degree of novelty of SRC is exploited to provide an operational solution to the well-known RS image TOC problem traditionally considered an unsolvable circular dilemma: While image classification benefits from preliminary TOC, the latter requires *a priori* knowledge of surface roughness which is land cover class specific. The proposed TOC solution consists of an operational automatic two-stage SNLTOC system comprising, in cascade, a novel automatic RS image stratification first stage and a second-stage ordinary SNLTOC equation (16) selected from existing literature and incorporating the stratified or layered approach.

The innovative automatic MS image stratification first stage is twofold. First, given a DEM of the input MS image and the sun's azimuth and zenith angles, the pixel-based incident angle $\gamma_i(n) \in [0^\circ, 180^\circ]$, $n = 1, \ldots, N$, is computed. Next, the incident angle domain is partitioned into four strata as a pixel-based (context-insensitive) function of the solar zenith angle. These four DEM-driven slices are identified as follows:

1) self-shadows, i.e., occluded areas belonging to shadow casters (to be masked out in the second-stage SNLTOC method);

2) horizontal surfaces (to be masked out in the second-stage SNLTOC method);
3) slopes facing the sun;
4) slopes facing away from the sun.

Second, symbolic (semantic) strata are automatically generated by SRC from the MS image radiometrically calibrated into $TOARF_T \supseteq \rho_T$ values.

The advantages of the operational automated two-stage SNLTOC system applied to nonhorizontal nonoccluded surfaces, either facing the sun or facing away from the sun, and belonging to the same symbolic layer (spectral category) provided by SRC are expected to be the following: 1) Computation time is optimized by ignoring pixels belonging to the aforementioned surface types 1) or 2), and 2) within-stratum variance should be reduced while pixel-based spectral patterns (shapes) are expected to be well preserved, i.e., no spectral distortion should be introduced by topographic normalization.

Up to 19 experiments were conducted in collaboration with an independent institutional partner to validate the novel operational automated two-stage SNLTOC system. Collected quantitative results are quite consistent with theoretical expectations and allow to reach the following conclusions.

1) In terms of operational performance measurement, the automatic SRC first stage is considered effective, computationally efficient, and robust to changes in the input data set acquired across time, space, and optical imaging sensors. Collected quantitative results are quite consistent with theoretical expectations, i.e., the theoretical framework of SRC appears sound, and in line with results collected in previous works [21]–[23], [45]. Therefore, SRC is, *per se*, considered eligible for use in operational satellite-based measurement systems providing potential components to the GEOSS and GMES system instantiations.
2) Applied to nonhorizontal nonoccluded surfaces, either facing the sun or away from the sun, and belonging to the same symbolic layer provided by the first-stage SRC, the automatic two-stage SNLTOC system features the following advantages: 1) Its ease of use is unsurpassed; 2) computation time is optimized (by ignoring pixels in horizontal surfaces or occluded surfaces belonging to shadow casters); 3) within-stratum variance is reduced while pixel-based spectral patterns (shapes) are well preserved, i.e., no spectral distortion is introduced by topographic normalization; and 4) it is robust to changes in the input data set acquired across time, space, and sensors. To summarize, the proposed two-stage SNLTOC system satisfies, as a whole, the set of system quality requirements, reviewed in Section I, to be considered eligible for use in an operational flow of RS data and land cover information.

As a secondary result, the RS image recovery from the ESA IMAGE2006 online archive experienced in this work proves that, to date, in spite of their 10- to 20-year membership in the CEOS, European institutions such as the ESA, DLR, and EC-JRC, involved with ongoing international projects focused on spaceborne multisource multitemporal image mosaicking and mapping at continental scale, either underestimate or ignore in practice 1) the problem of transforming DNs into a community-agreed radiometric scale to enhance interimage comparability across time, space, and sensors as required by the QA4EO initiative in the framework of the GEOSS and GMES programs and 2) the well-known principle that data management, including data sharing and redundancy (duplication), is often more critical than data collection in guaranteeing the integrity (i.e., accuracy and completeness) of a database [39, p. 16].

Future developments of this paper will be the following.

1) Integration of a shadow-casting algorithm into the DEM-driven stratification phase (refer to Section IV-A1).
2) Implementation of an ambient occlusion algorithm for modeling indirect illumination in shadow (occluded) areas (refer to Section IV-A1).
3) Integration of spatial relationships into the two-stage SNLTOC system to detect slopes facing the sun and facing away from the sun that are adjacent to one another and belong to the same semantic layer (e.g., vegetation). Thus, local area estimation of SNLTOC regression parameters can be based on convergence of topographic (e.g., slopes facing the sun and facing away from the sun), semantic (e.g., vegetation), and spatial (e.g., adjacency) evidence.

## APPENDIX I
## SRC COMPARED TO SAM

It is noteworthy that there are at least four structural differences between SAM and SRC which make these two pixel-based vector data mapping approaches not at all alternative, but complementary in operational terms.

1) SRC maps each pixel onto a discrete and finite set of indexes based on both the pixel-based reflectance pattern (shape) and the data vector magnitude, while SAM pursues spectral pattern matching exclusively. This allows SRC to discriminate between, for example, a spectral category [color-based semiconcept (refer to Section IV-A2)] named vegetation in shadow areas [which can be spectrally indistinguishable from coniferous forest (see Fig. 3)] from spectral categories such as strong/average/weak vegetation in sun-exposed areas (where fuzzy sets strong/average/weak vegetations depend on both the LAI and the intensity of sunlight). In particular, in Fig. 3, the spectral category shadowed vegetation is not linearly scaled from the spectral categories strong/average/weak vegetation. Rather, the latter spectral types mainly differ in brightness (magnitude), i.e., they are approximately linearly scaled versions of one another analogously to dark- and light-toned soils (see [81, p. 276]). In this example, the discrimination capability of SAM is inferior to SRC's since the former would consider spectral categories strong/average/weak vegetation as indistinguishable.

2) SRC is prior knowledge based, i.e., it is nonadaptive to data, and is capable of providing a totally exhaustive and mutually exclusive classification of the input RS image without requiring any user supervision (see Section IV-A2). On the contrary, SAM is supervised (labeled) data driven, i.e., it requires the acquisition of ground-truth data across the study area for training.
3) SRC requires no user-defined parameter while SAM requires one user-defined parameter, namely, the maximum angle threshold (in radians) to consider pixels further away than the specified maximum angle threshold not classified (outliers).
4) SRC provides a classification map consisting of spectral semiconcepts [e.g., *vegetation* (see Section IV-A2)] less informative than land cover concepts (e.g., *forest*) provided by SAM, which counterbalances the superior degree of automation of the former.

## APPENDIX II
## SRC COMPARED TO UNSUPERVISED DATA-CLUSTERING ALGORITHMS

In classical philosophy, the general notion of *inference* (learning) comprises two types of learning mechanisms known as "*induction* [i.e., progressing from particular cases (e.g., training data) to general (e.g., estimated dependence or model)]," therefore called *bottom–up, fine to coarse, data driven,* or *learning by example*, and "*deduction* [i.e., progressing from general (e.g., model) to particular cases (e.g., output values)]," therefore called *top–down, coarse to fine, model driven,* or *learning by rule* [72]. In particular, "induction amounts to forming generalizations from particular true facts. This is an inherently difficult (ill-posed) problem and its solution requires *a priori* knowledge in addition to data" [72, p. 39].

When compared to well-known inductive unsupervised (unlabeled) data-learning algorithms, such as ISODATA and $k$-means typically employed in unlabeled data-clustering problems, the fully automated prior knowledge-based SRC mapping system is more successful in providing a preliminary understanding (mapping) of an MS image. This is due to the fact that the latter accounts for a dictionary of reference spectra in $TOARF_T$ values (see Fig. 3) representing its prior knowledge of the (3-D) world depicted in a spaceborne MS (2-D) image. The drawbacks of the former approach are as follows.

1) Since the goal of clustering is to group the data at hand rather than to provide an accurate characterization of unobserved (future) samples generated from the same probability distribution, the task of clustering may fall outside the framework of predictive (inductive) learning. In spite of this, clustering analysis often employs unsupervised data-learning techniques originally developed for vector quantization (such as the $k$-means unsupervised data-learning algorithm which belongs to the family of the crisp competitive minimum-distance-to-means algorithms [73], [74]) which is a predictive learning problem [72].
2) Unlabeled data clustering is an inherently ill-posed data mapping problem, whereas the spectral pattern matching performed by SRC is well posed. In fact, the goal of clustering is to separate a finite unlabeled data set at hand into a finite and discrete set of "natural" hidden data structures on the basis of an often subjectively chosen measure of similarity, i.e., chosen subjectively based on its ability to create "interesting" clusters [72], [75]–[78]. Thus, the subjective (ill-posed) nature of the nonpredictive clustering problem precludes an absolute judgement as to the relative effectiveness of all clustering techniques [78]. In spite of this, the inherent ill-posedness of unlabeled data-clustering problems is not clearly stated in existing literature where, as a consequence, dozens of papers proposing alternative clustering algorithms are published every year (perhaps in search of a "final" best clustering algorithm which cannot exist) [79].
3) Crisp (hard) competitive minimum-distance-to-means algorithms, such as $k$-means data clustering, try to minimize a sum-of-squares error function. To reduce the risk of being trapped in a local minimum of the error function, soft-to-hard rather than hard competitive clustering algorithms have been conceived [73], [74]. In addition, it is well known that either crisp or fuzzy $k$-means data-clustering algorithms cannot perform well with nonconvex types of data, i.e., they are effective if and only if data clusters are hyperspherical [80]. To overcome this problem, a $k$-means unsupervised data-learning algorithm capable of defining automatically the number of clusters splits a nonconvex data cluster, for example, a data cluster shaped like a banana, into several hyperspheres. Thus, these hyperspheres should be linked to map the banana-like data cluster. To perform nonconvex unlabeled data mapping, topologically preserving data-clustering algorithms have been developed [75]–[78].
4) Any clustering algorithm provides unlabeled data with a subsymbolic (asemantic) label (e.g., cluster 1, cluster 2, etc.), whereas SRC, which is prior knowledge based, provides unknown pixels with a label equivalent to a color-based semiconcept featuring a semantic meaning (e.g., vegetation, either water or shadow, etc.) (see Section IV-A2).
5) In terms of ease of use, every data-clustering algorithm requires at least one free parameter, to be either user defined or fixed by the application developer based on heuristics, to make the inherently ill-posed unlabeled data-clustering problem better posed. For example, it is paradoxical that the well-known $k$-means vector quantizer typically employed for unlabeled data clustering requires the user to predefine the number of clusters hidden in the data.
6) In terms of computation time, unlabeled data clustering is iterative while SRC is a one-pass mapping algorithm.
7) In terms of effectiveness and robustness to changes in the input data set, a qualitative (visual) assessment of the SRC maps shown in [45] should be sufficient to support the superiority of SRC versus $k$-means unlabeled data clustering among RS scientists and practitioners at

first glance. Typically, RS images mapped by pixel-based clustering algorithms are affected by a well-known salt-and-pepper classification noise effect which is absent in the SRC maps. This is due to the fact that SRC, which is also pixel-based, is successful in modeling the within-class spectral variance from prior spectral knowledge consisting of endmember collection spectra.

## ACKNOWLEDGMENT

A. Baraldi would like to thank P. Soille of EC-JRC for radiometrically calibrating the two testing images. The authors would also like to thank the Editor-in-Chief, the Associate Editor, and the anonymous reviewers for their helpful comments and their patience in reviewing this paper, as well as for their competence and willingness to help.

## REFERENCES

[1] G. Gutman, A. C. Janetos, C. O. Justice, E. F. Moran, J. F. Mustard, R. R. Rindfuss, D. Skole, B. L. Turner, II, and M. A. Cochrane, Eds. *Land Change Science*. Dordrecht, The Netherlands: Kluwer, 2004.

[2] O. Sjahputera, C. H. Davis, B. Claywell, N. J. Hudson, J. M. Keller, M. G. Vincent, Y. Li, M. Klaric, and C. R. Shyu, "GeoCDX: An automated change detection and exploitation system for high resolution satellite imagery," in *Proc. IGARSS*, Boston, MA, Jul. 6–11, 2008, pp. V-467–V-470.

[3] F. Sart, J. Inglada, R. Landry, and T. Pultz, "Risk management using remote sensing data: Moving from scientific to operational applications," in *Proc. SBSR Workshop*, Florianopolis, Brasil, Apr. 23–27, 2001. [Online]. Available: www.treemail.nl/download/sarti01.pdf

[4] [Online]. Available: www.fabricadebani.ro/userfiles/GEO_press_release.doc

[5] P. Zamperoni, "Plus ça va, moins ça va," *Pattern Recognit. Lett.*, vol. 17, no. 7, pp. 671–677, Jun. 1996.

[6] R. Richterin "Atmospheric/topographic correction (ATCOR) for satellite imagery," DLR, Wessling, Germany, Rep. DLR-IB 565-01/06, 2006. [Online]. Available: http://www.geosystems.de/atcor/index.html

[7] *eCognition User Guide 4*, Definiens Imaging GmbH, Munich, Germany, 2004.

[8] M. Page-Jones, *The Practical Guide to Structured Systems Design*. Englewood Cliffs, NJ: Prentice-Hall, 1988.

[9] Z. G. Wei, A. P. Macwan, and P. A. Wieringa, "A quantitative measure for degree of automation and its relation to system performance and mental load," *Hum. Factors*, vol. 40, no. 2, pp. 277–295, Jun. 1998.

[10] Q. Yu and D. A. Clausi, "SAR sea–ice image analysis based on iterative region growing using semantics," *IEEE Trans. Geosci. Remote Sens.*, vol. 45, no. 12, pp. 3919–3931, Dec. 2007.

[11] A. Strahler, D. Muchoney, J. Borak, M. Friedl, S. Gopal, E. Lambin, and A. Moody, *Modis Land Cover Product Algorithm Theoretical Basis Document (ATBD)*. ver. 5.0, MODIS Science Team. [Online]. Available: http://modis.gsfc.nasa.gov/data/atbd/atbd_mod12.pdf

[12] GEO, *GEO 2007–2009 Work Plan: Toward Convergence*, 2008. [Online]. Available: http://earthobservations.org

[13] GEO, *The Global Earth Observation System of Systems (GEOSS) 10-Year Implementation Plan*. adopted Feb. 16, 2005. [Online]. Available: http://www.earthobservations.org/docs/10-Year%20Implementation%20Plan.pdf

[14] [Online]. Available: http://www.gmes.info

[15] GEO/CEOSS, *A Quality Assurance Framework for Earth Observation*, Sep. 2008. ver. 2.0. [Online]. Available: http://calvalportal.ceos.org/CalValPortal/showQA4EO.do?section=qa4eoIntro

[16] [Online]. Available: http://www.ceos.org

[17] I. Dowman, "Foreword," in *International Society for Photogrammetry and Remote Sensing (ISPRS) Book Series—Post-Launch Calibration of Satellite Sensors*, S. A. Morain and A. M. Buedge, Eds. Leiden, The Netherlands: Balkema, 2004, p. IX.

[18] T. Lillesand and R. Kiefer, *Remote Sensing and Image Interpretation*. New York: Wiley, 1979.

[19] S. Liang, *Quantitative Remote Sensing of Land Surfaces*. Hoboken, NJ: Wiley, 2004.

[20] P. Mather, *Computer Processing of Remotely-Sensed Images—An Introduction*. Chichester, U.K.: Wiley, 1994.

[21] A. Baraldi, V. Puzzolo, L. Durieux, D. Simonetti, G. Conchedda, F. Holecz, and P. Blonda, "Automatic spectral rule-based preliminary classification of radiometrically calibrated SPOT-4/-5/IRS, AVHRR/MSG, AATSR, IKONOS/QuickBird/OrbView/GeoEye and DMC/SPOT-1/-2 imagery—Part I: System design and implementation," *IEEE Trans. Geosci. Remote Sens.,* to be published.

[22] A. Baraldi, V. Puzzolo, L. Durieux, D. Simonetti, G. Conchedda, F. Holecz, and P. Blonda, "Automatic spectral rule-based preliminary classification of radiometrically calibrated SPOT-4/-5/IRS, AVHRR/MSG, AATSR, IKONOS/QuickBird/OrbView/GeoEye and DMC/SPOT-1/-2 imagery—Part II: Classification accuracy assessment," *IEEE Trans. Geosci. Remote Sens.,* to be published.

[23] A. Baraldi, T. Wassenaar, and S. Kay, "Automatic preliminary spectral rule-based decision-tree classification of spaceborne very high resolution optical imagery—Mapping vegetation and bare soil types across the European Union's agricultural landscapes," *IEEE Trans. Geosci. Remote Sens.*, submitted for publication.

[24] R. R. Irish "Landsat 7 automatic cloud cover assessment (ACCA)," in *Proc. SPIE—Algorithms Multispectral, Hyperspectral, and Ultraspectral Imagery VI*, S. S. Shen and M. R. Descour, Eds., 2000, vol. 4049, pp. 348–355. [Online]. Available: http://landsathandbook.gsfc.nasa.gov/handbook/pdfs/ACCA_SPIE_paper.pdf

[25] C. Small, "The Landsat ETM+ spectral mixing space," *Remote Sens. Environ.*, vol. 93, no. 1/2, pp. 1–17, Oct. 2004.

[26] A. Baraldi, "Impact of radiometric calibration and specifications of spaceborne optical imaging sensors on the development of operational automatic remote sensing image understanding systems," *IEEE J. Sel. Topics Appl. Earth Obs. Remote Sens.*, vol. 2, no. 2, pp. 104–134, Jun. 2009.

[27] P. Henry and A. Meygret, "Calibration of VEGETATION camera on-board SPOT4," *Adv. Space Res.*, vol. 28, no. 1, pp. 49–58, 2001.

[28] P. S. Chavez, "An improved dark-object subtraction technique for atmospheric scattering correction of multispectral data," *Remote Sens. Environ.*, vol. 24, no. 3, pp. 459–479, Apr. 1988.

[29] D. Riaño, E. Chuvieco, J. Salas, and I. Aguado, "Assessment of different topographic corrections in Landsat TM data for mapping vegetation types," *IEEE Trans. Geosci. Remote Sens.*, vol. 41, no. 5, pp. 1056–1061, May 2003.

[30] A. Thomson and C. Jones, "Effects of topography on radiance from upland vegetation in North Wales," *Int. J. Remote Sens.*, vol. 11, no. 5, pp. 829–840, May 1990.

[31] K. H. Law and J. Nichol, "Topographic correction for differential illumination effects on IKONOS satellite imagery," *Int. Arch. Photogramm. Remote Sens. Spat. Inf. Sci.*, vol. 35, no. 3, pp. 641–646, 2004.

[32] D. L. Civco, "Topographic normalization of Landsat Thematic Mapper digital imagery," *Photogramm. Eng. Remote Sens.*, vol. 55, no. 9, pp. 1303–1309, 1989.

[33] P. M. Teillet, B. Guindon, and D. G. Goodenough, "On the slope-aspect correction of multispectral scanner data," *Can. J. Remote Sens.*, vol. 8, no. 2, pp. 84–106, 1982.

[34] A. Twele, M. Kappas, J. Lauer, and S. Erasmi, "The effect of stratified topographic correction on land cover classification in tropical mountainous regions," in *Proc. ISPRS Comm. VII Symp.*, Enschede, The Netherlands, May 8–11, 2006, pp. 432–437.

[35] A. Twele and S. Erasmi, "Evaluating topographic correction algorithms for improved land cover discrimination in mountainous areas of Central Sulawesi," in *Remote Sensing and GIS for Environmental Studies*, vol. 113, S. Erasmi, B. Cyffka, and M. Kappas, Eds. Göttingen, Germany: Verlag Erich Goltze, 2005, pp. 287–295.

[36] T. Tokola, J. Sarkeala, and M. Van der Linden, "Use of topographic correction in Landsat TM-based forest interpretation in Nepal," *Int. J. Remote Sens.*, vol. 22, no. 4, pp. 551–563, Mar. 2001.

[37] M. P. Bishop and J. D. Colby, "Anisotropic reflectance correction of SPOT-3 HRV imagery," *Int. J. Remote Sens.*, vol. 23, no. 10, pp. 2125–2131, May 2002.

[38] M. P. Bishop, J. F. Shroder, and J. D. Colby, "Remote sensing and geomorphometry for studying relief production in high mountains," *Geomorphology*, vol. 55, no. 1–4, pp. 345–361, Sep. 2003.

[39] L. Blesius and F. Weirich, "The use of the Minnaert correction for land cover classification in mountainous terrain," *Int. J. Remote Sens.*, vol. 26, no. 17, pp. 3831–3851, Sep. 2005.

[40] J. D. Shepherd and J. R. Dymond, "Correcting satellite imagery for the variance of reflectance and illumination with topography," *Int. J. Remote Sens.*, vol. 24, no. 17, pp. 3831–3851, Sep. 2005.

[41] E. R. McDonald, X. Wu, P. Caccetta, and N. Campbell, "Illumination correction of Landsat TM data in South East NSW," in *Proc. 10th ARSPC*, Adelaide, Australia, Aug. 21–25, 2000. [Online]. Available: http://www.environment.gov.au/land/publications/pubs/illumination.pdf

[42] X. Wu, S. Furby, and J. Wallace, "An approach for terrain illumination correction," in *Proc. 12th ARSPC*, Fremantle, Australia, Oct. 2004. [Online]. Available: http://www.cmis.csiro.au/rsm/research/pdf/wu_x_12ARSPC_TerrainIllumination.pdf

[43] G. Palubinskas, R. Muller, and P. Reinartz, "Radiometric normalization of optical remote sensing imagery," in *Proc. IGARSS*, Jul. 21–25, 2003, vol. 2, pp. 720–722.

[44] D. Lu, H. Ge, S. He, A. Xu, G. Zhou, and H. Du, "Pixel-based Minnaert correction method for reducing topographic effects on a Landsat 7 ETM+ image," *Photogramm. Eng. Remote Sens.*, vol. 74, no. 11, pp. 1343–1350, Nov. 2008.

[45] A. Baraldi, V. Puzzolo, P. Blonda, L. Bruzzone, and C. Tarantino, "Automatic spectral rule-based preliminary mapping of calibrated Landsat TM and ETM+ images," *IEEE Trans. Geosci. Remote Sens.*, vol. 44, no. 9, pp. 2563–2586, Sep. 2006.

[46] D. Foldes and B. Benes, "Occlusion-based snow accumulation simulation," in *Proc. 4th Workshop VRIPHYS*, 2007, pp. 35–41. [Online]. Available: http://www.envision.purdue.edu/pdfs/papers/Foldes07Vriphys.pdf

[47] S. Sandmeier and K. Itten, "A physical-based model to correct atmospheric and illumination effects in optical satellite data of rugged terrain," *IEEE Trans. Geosci. Remote Sens.*, vol. 35, no. 3, pp. 708–717, May 1997.

[48] N. Hoffman and K. Mitchell, *Real-Time Photorealistic Terrain Lighting*. [Online]. Available: www.gamasutra.com/features/gdcarchive/2001/hoffman.doc

[49] [Online]. Available: http://www.SPOTimage.fr/html/_167_224_584_php

[50] [Online]. Available: http://eo1.usgs.gov

[51] A. K. Shackelford and C. H. Davis, "A hierarchical fuzzy classification approach for high-resolution multispectral data over urban areas," *IEEE Trans. Geosci. Remote Sens.*, vol. 41, no. 9, pp. 1920–1932, Sep. 2003.

[52] G. Zhou and M. Kafatos, "Future intelligent earth observing satellites (FIEOS)," in *Proc. ISPRS/FIEOS Conf.*, 2002. [Online]. Available: http://www.isprs.org/commission1/proceedings02/paper/00031.pdf

[53] [Online]. Available: http://directory.eoportal.org/info_3rdInternationalSymposiumonFutureIntelligentEarthObservingSatellitesFIEOS.html

[54] J. D. Colby, "Topographic normalization in rugged terrain," *Photogramm. Eng. Remote Sens.*, vol. 57, no. 5, pp. 531–537, May 1991.

[55] T. Svoray and Y. Carmel, "Empirical method for topographic correction in aerial photographs," *IEEE Geosci. Remote Sens. Lett.*, vol. 2, no. 2, pp. 211–214, Apr. 2005.

[56] *ENVI 4.3 User Manual*, ITT Industries Inc., Boulder, CO, 2006.

[57] Y. Sohn, E. Motan, and F. Gurri, "Deforestation in North-Central Yucatan (1985–1995): Mapping secondary succession of forest and agricultural land use in Sotuta using the Cosine of the angle concept," *Photogramm. Eng. Remote Sens.*, vol. 65, no. 8, pp. 947–958, Aug. 1999.

[58] S. South, J. Qi, and D. P. Lusch, "Optimal classification methods for mapping agricultural tillage practices," *Remote Sens. Environ.*, vol. 91, no. 1, pp. 90–97, May 2004.

[59] L. J. Guo and J. M. Moore, "Cloud-shadow suppression technique for enhancement of airborne Thematic Mapper imagery," *Photogramm. Eng. Remote Sens.*, vol. 59, no. 8, pp. 1287–1291, Aug. 1993.

[60] K. F. Huemmrich, "Effects of shadows on vegetation indices," in *Proc. IGARSS*, 1996, vol. 4, pp. 2372–2374.

[61] A. Baraldi and F. Parmiggiani, "Combined detection of intensity and chromatic contours in color images," *Opt. Eng.*, vol. 35, no. 5, pp. 1413–1439, May 1996.

[62] A. Baraldi and F. Parmiggiani, "A neural network for unsupervised categorization of multivalued input patterns: An application to satellite image clustering," *IEEE Trans. Geosci. Remote Sens.*, vol. 33, no. 2, pp. 305–316, Mar. 1995.

[63] [Online]. Available: http://www.coventry.ac.uk/ec/~nhunt/meths/strati.html

[64] C. M. Bishop, *Neural Networks for Pattern Recognition*. Oxford, U.K.: Clarendon, 1995.

[65] C. Mason and E. R. Kandel, "Central visual pathways," in *Principles of Neural Science*, E. Kandel and J. Schwartz, Eds. Norwalk, CT: Appleton Lange, 1991, pp. 420–439.

[66] P. Gouras, "Color vision," in *Principles of Neural Science*, E. Kandel and J. Schwartz, Eds. Norwalk, CT: Appleton Lange, 1991, pp. 467–479.

[67] T. Matsuyama and V. Shang-Shouq Hwang, *SIGMA—A Knowledge-Based Aerial Image Understanding System*. New York: Plenum, 1990.

[68] K. Shackelford and C. H. Davis, "A combined fuzzy pixel-based and object-based approach for classification of high-resolution multispectral data over urban areas," *IEEE Trans. Geosci. Remote Sens.*, vol. 41, no. 10, pp. 2354–2363, Oct. 2003.

[69] J. Bestimt and B. Freitag, *Real-Time Shadow Casting Using Shadow Volumes*. [Online]. Available: http://www.gamasutra.com/features/19991115/bestimt_freitag_01.htm

[70] M. Woo Davis and M. B. Sheridan, *OpenGL Programming Guide: The Official Guide to Learning OpenGL*. Boston, MA: Addison-Wesley, 2006. ver. 2.0.

[71] V. Perdigao and A. Annoni, "Technical and methodological guide for updating CORINE land cover data base," Eur. Comm. Joint Res. Center, Ispra, Italy, Tech. Rep. EUR 17288, 1997.

[72] V. Cherkassky and F. Mulier, *Learning From Data: Concepts, Theory, and Methods*. New York: Wiley, 1998.

[73] A. Baraldi and P. Blonda, "A survey of fuzzy clustering algorithms for pattern recognition: Part I," *IEEE Trans. Syst., Man, Cybern. B, Cybern.*, vol. 29, no. 6, pp. 778–785, Dec. 1999.

[74] A. Baraldi and P. Blonda, "A survey of fuzzy clustering algorithms for pattern recognition: Part II," *IEEE Trans. Syst., Man, Cybern. B, Cybern.*, vol. 29, no. 6, pp. 786–801, Dec. 1999.

[75] A. Baraldi and E. Alpaydin, "Constructive feedforward ART clustering networks—Part I," *IEEE Trans. Neural Netw.*, vol. 13, no. 3, pp. 645–661, May 2002.

[76] A. Baraldi and E. Alpaydin, "Constructive feedforward ART clustering networks—Part II," *IEEE Trans. Neural Netw.*, vol. 13, no. 3, pp. 662–677, May 2002.

[77] B. Fritzkein "Some competitive learning methods," Ruhr-Universität Bochum, Bochum, Germany, 1997. [Online]. Available: http://www.ki.inf.tu-dresden.de/~fritzke/JavaPaper

[78] E. Backer and A. K. Jain, "A clustering performance measure based on fuzzy set decomposition," *IEEE Trans. Pattern Anal. Mach. Intell.*, vol. PAMI-3, no. 1, pp. 66–75, Jan. 1981.

[79] R. Xu and D. Wunsch, II, "Survey of clustering algorithms," *IEEE Trans. Neural Netw.*, vol. 16, no. 3, pp. 645–678, May 2005.

[80] R. Duda, P. Hart, and D. Stork, *Pattern Classification*. New York: Wiley, 2001.

[81] P. H. Swain and S. M. Davis, *Remote Sensing: The Quantitative Approach*. New York: McGraw-Hill, 1978.

[82] W. Zhou, G. Huang, A. Troy, and M. L. Cadenasso, "Object-based land cover classification of shaded areas in high spatial resolution imagery of urban areas: A comparison study," *Remote Sens. Environ.*, vol. 113, no. 8, pp. 1769–1777, Aug. 2009.

[83] L. Delves, R. Wilkinson, C. Oliver, and R. White, "Comparing the performance of SAR image segmentation algorithms," *Int. J. Remote Sens.*, vol. 13, no. 11, pp. 2121–2149, 1992.

[84] *GMES IMAGE2006 Mosaic*. [Online]. Available: http://www.gmes-gseland.info/com/news/GMES-Land_NewsLetter_I1.00.pdf

[85] R. Lunetta and D. Elvidge, *Remote Sensing Change Detection: Environmental Monitoring Methods and Applications*. London, U.K.: Taylor & Francis, 1999.

[86] X. Dai and S. Khorram, "The effects of image misregistration on the accuracy of remotely sensed change detection," *IEEE Trans. Geosci. Remote Sens.*, vol. 36, no. 5, pp. 1566–1577, Sep. 1998.

[87] A. Baraldi, L. Bruzzone, and P. Blonda, "Quality assessment of classification and cluster maps without ground truth knowledge," *IEEE Trans. Geosci. Remote Sens.*, vol. 43, no. 4, pp. 857–873, Apr. 2005.

[88] R. G. Congalton and K. Green, *Assessing the Accuracy of Remotely Sensed Data*. Boca Raton, FL: Lewis, 1999.

[89] G. M. Foody, "Status of land cover classification accuracy assessment," *Remote Sens. Environ.*, vol. 80, no. 1, pp. 185–201, Apr. 2002.

[90] Z. Wang and A. C. Bovik, "A universal image quality index," *IEEE Signal Process. Lett.*, vol. 9, no. 3, pp. 81–84, Mar. 2002.

[91] P. Lukowicz, E. Heinz, L. Prechelt, and W. Tichy, "Experimental evaluation in computer science: A quantitative study," Univ. Karlsruhe, Karlsruhe, Germany, Tech. Rep. 17/94, 1994.

[92] L. Prechelt, "A quantitative study of experimental evaluations of neural network learning algorithms: Current research practice," *Neural Netw.*, vol. 9, no. 3, pp. 457–462, Apr. 1996.

[93] *Proceedings and Recommendations of the Workshop on European Reference Grids*, European Commission Joint Research Center—Institute for Environment and Sustainability, Ispra, Italy, Oct. 27–29, 2003. EUR 21494 EN.

**Andrea Baraldi** was born in Modena, Italy, in 1963. He received the Laurea (M.S.) degree in electronic engineering from the University of Bologna, Bologna, Italy, in 1989. His M.S. thesis focused on the development of segmentation and classification algorithms for remotely sensed optical imagery.

From 1989 to 1990, he was a Research Associate with the Centro di Studio per l'Interazione Operatore–Calcolatore, National Research Council (CNR), Bologna, and served in the army with the Istituto Geografico Militare, Florence, Italy, working on satellite image classifiers and geographic information systems (GISs). As a Consultant with the European Space Agency European Space Research Institute, Frascati, Italy, he worked on object-oriented applications for GISs from 1991 to 1993. From December 1997 to June 1999, he was assigned with a Postdoctoral Fellowship in Artificial Intelligence with the International Computer Science Institute, Berkeley, CA. From 2000 to 2002, as a Postdoctoral Researcher, he joined the Global Vegetation Monitoring Unit, Institute for Environment and Sustainability (IES), European Commission Joint Research Centre (JRC), Ispra, Italy, in the development and validation of algorithms for forest classification of radar mosaics at continental scale. From 2005 to 2009, with the IES–Spatial Data Infrastructure Unit, JRC, he was involved with satellite optical image calibration, classification, and mosaicking at continental scale. Since his master's thesis, he has continued his collaboration with Istituto di Scienze dell'Atmosfera e del Clima, CNR, Bologna, and Istituto di Studi sui Sistemi Intelligenti per l'Automazione, CNR, Bari, Italy. He is currently with Baraldi Consultancy in Remote Sensing, Bologna. His main research interests center on image understanding, with special emphasis on the development of operational automatic hierarchical multisource multiresolution spaceborne image-understanding systems consistent with biological vision.

Mr. Baraldi was an Associate Editor of the IEEE TRANSACTIONS ON NEURAL NETWORKS from 2001 to 2006.

**Matteo Gironda** was born in Noventa Vicentina, Italy, in 1979. He received the B.S. degree in forestry from Padua University, Padua, Italy, in 2003 and the M.S. degree in geographic information systems and remote sensing from the University Institute of Architecture of Venice, Venezia, Italy, in 2008.

He was with the University Institute of Architecture of Venice. He is currently a Private Officer in the environmental field.

**Dario Simonetti** was born in Varese, Italy, in 1981. He received the Laurea (M.S.) degree in informatics from the Facoltà di Scienze Matematiche, Fisiche e Naturali, Università dell'Insubria, Varese, in 2004. His thesis focused on the development of improved classification algorithms for near-real-time fire detection at global scale from satellite optical imagery.

Since 2004, he has been an Analyst–Programmer Consultant with the Global Environment Monitoring Unit, Institute for Environment and Sustainability, European Commission Joint Research Centre, Ispra, Italy. His main activities are focused on automatic near-real-time analysis of fire occurrences in African protected areas, development and assessment of processing chain for calibration, coregistration, topographic correction, and classification of satellite imagery, and development of user-friendly geographic information system applications for validation of satellite imagery classification across different epochs. He is contributing in delivering products and services derived from the analysis of satellite remote sensing data, with special emphasis on biodiversity and land cover change detection.